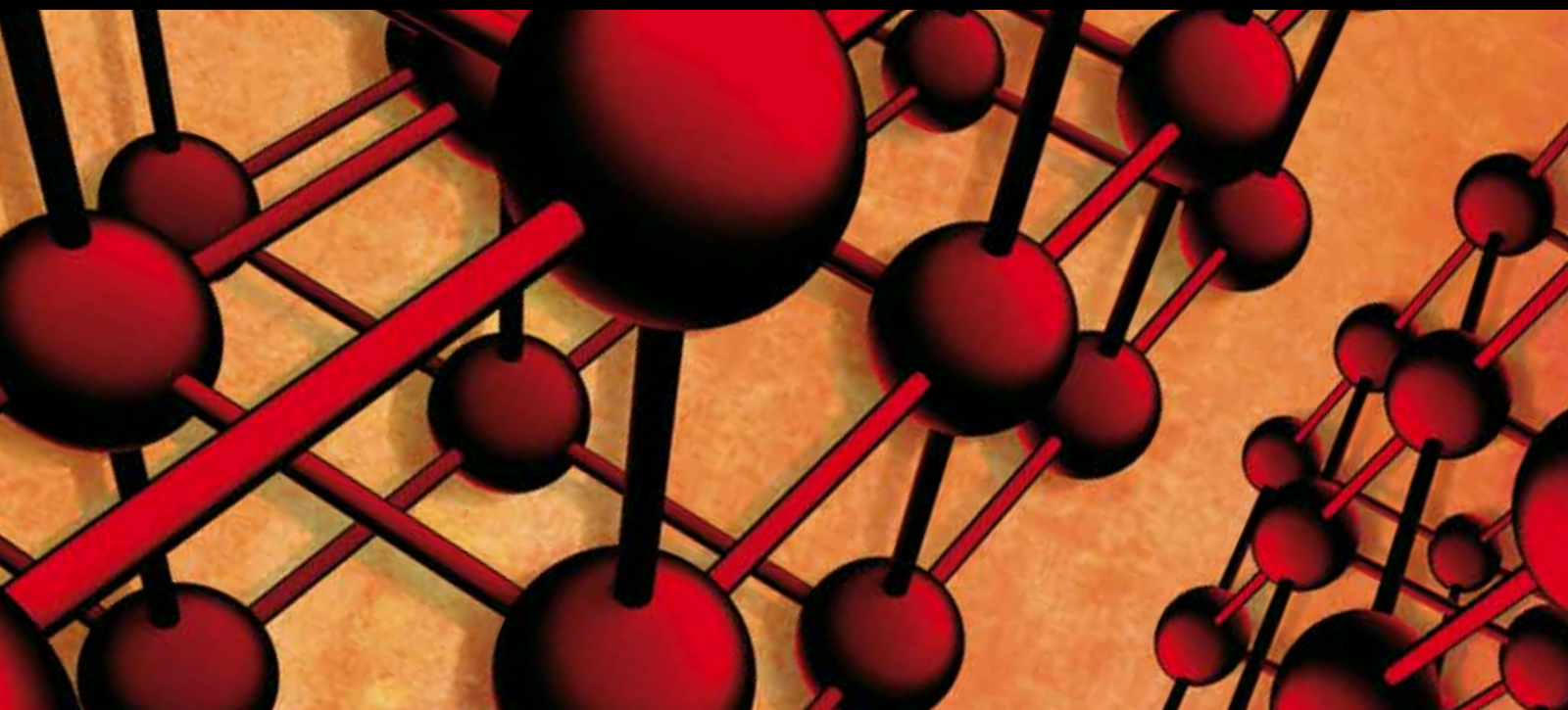# Solar Energy: Materials, Devices, and Applications

Guest Editors: Ru-Yuan Yang, Yu-Pei Huang, Nowshad Amin, and Fengqiang Sun

Solar Energy: Materials, Devices, and Applications

Solar Energy: Materials, Devices, and Applications

Guest Editors: Ru-Yuan Yang, Yu-Pei Huang, Nowshad Amin, and Fengqiang Sun

Editorial Board

Contents

Editorial

Solar Energy: Materials, Devices, and Applications

Ru-Yuan Yang,[1] Yu-Pei Huang,[2] Nowshad Amin,[3] and Fengqiang Sun[4]

[1] *Graduate Institute of Materials Engineering, National Pingtung University of Science and Technology, Pingtung 91201, Taiwan*
[2] *Department of Electronic Engineering, National Quemoy University, Kinmen 89250, Taiwan*
[3] *Department of Electrical, Electronic, and Systems Engineering Mathematics, National University of Malaysia, 43600 Bangi, Selangor, Malaysia*
[4] *Department of Materials Science and Engineering, South China Normal University, Guangzhou, Guangdong 510631, China*

Correspondence should be addressed to Ru-Yuan Yang, ryyang@mail.npust.edu.tw

Received 2 December 2012; Accepted 2 December 2012

As "a low-carbon society and CO_2-free energy" have been the global issues, so have the opportunities and challenges for renewable energy technologies, like photovoltaic solar cells. Solar energy is an alternative of fossil fuels. Dye-sensitized solar cells (DSSCs), organic thin-film solar cells, quantum dot solar cells, Schottky solar cells, inorganic-organic heterojunction solar cells, and many others have been developed with the promise of further improvements to both performance and affordability expected during the last years.

The aim of this special issue has been to present the latest and generalized coverage of the fundamental and constructive ideas, concepts, and important issues in the accepted original research articles stimulating the continuing efforts to solar energy. We received 12 research papers in the research fields. This special issue includes 8 high-quality peer-reviewed papers. We hope that this collection of papers will be a source of ideas and motivation for scientists across different fields in academia and industry to continue further research on solar energy including topics about materials, devices, and applications.

In the fascinating paper by A. M. Abdel-Ghany and I. M. Al-Helal, under solar radiation conditions, the modeling approach has been used to determine equivalent optical constants of plastic shading nets. W.-s. Kuo and C.-l. Wu provide a treatment of color filter wastewater using solar photo-Fenton process enhanced by high-concentrating Fresnel lens. Series resistance analysis is presented by M. Lenio et al. for passivated emitter rear contact cells patterned using inkjet printing. In the nonvacuum processes for solar cell materials, S. Ito and T. Ryo are working successfully on finding segregation of Cu-In-S elements in the spray-pyrolysis-deposited layer of solar cells. In the interesting paper by H. Zhao et al., the experimental study on solar cooling tube has been built using thermal/vacuum emptying method. These wonderful results in the studies of ruthenium complex sensitizer and gold nanoparticles doped flexible organic solar cells are given by L.-C. Chen and C.-C. Chen. Organic compounds effect on microstructure, optical, and electrical properties of ITO thin films prepared by dip coating method has been investigated by Y.-M. Peng et al. Finally, the other published paper has good studies on providing the phenomenon of performance degradation induced by electrolytes for dye-sensitized solar cells by H.-Y. Chen et al.

Acknowledgments

Ru-Yuan Yang
Yu-Pei Huang
Nowshad Amin
Fengqiang Sun

Research Article

Segregation of Cu-In-S Elements in the Spray-Pyrolysis-Deposited Layer of CIS Solar Cells

Seigo Ito and Toshihiro Ryo

Department of Electric Engineering and Computer Sciences and Department of Materials Science and Chemistry,
University of Hyogo, 2167 Shosha, Himeji, Hyogo 671-2280, Japan

Correspondence should be addressed to Seigo Ito, itou@eng.u-hyogo.ac.jp

We report the fabrication of superstrate-structured solar cells by the deposition of Cu-In-S (CIS) films on $\langle glass/FTO/TiO_2/In_2S_3 \rangle$ under air by spray pyrolysis. The cells had an open-circuit voltage of 0.551 V, a photocurrent density of 9.5 mA/cm^2, a fill factor of 0.45, and a conversion efficiency of 2.14%. However, transmission electron microscopy/energy dispersive X-ray (TEM-EDX) analysis revealed significant differences between the atomic ratio of the setting material in the spray-deposition solution and the elements in the layer. Moreover, TEM-EDX measurements suggested strong segregation of the Cu-In-S elements in the spray-pyrolysis-deposited layer. The degree of segregation depended on the substrate ($\langle glass \rangle$, $\langle glass/TiO_2 \rangle$, or $\langle glass/TiO_2/In_2S_3 \rangle$), although $Cu_3In_5S_9$ nanoparticles were segregated in the sulfur layer.

1. Introduction

Compound solar cells with high-conversion efficiencies (20.3%) have been fabricated by vacuum methods [1], which are slow and require costly equipment. Nonvacuum processes for solar cell materials, such as $Cu(In_{1-x}Ga_x)Se_2$, $CuInSe_2$, and $CuInS_2$ (CIS), have been investigated with the aim of developing fast and inexpensive fabrication methods. Printing [2, 3], spray-pyrolysis-deposition (SPD) [4, 5], selenization of printed metal oxides with H_2S or H_2Se [6], and electrochemical deposition [7, 8] have been explored as alternative methods. Less toxic materials are required because nonvacuum methods are carried out in air; therefore $CuInS_2$ absorber materials are more suitable than $CuInSe_2$ or $Cu(In,Ga)Se_2$. This is particularly important for SPD methods because aerosols are formed from the compounds. In this work, the structures of spray-pyrolysis-deposited Cu-In-S layers, which have 2.14% conversion efficiency in superstrate-structured solar cells, were studied by transmission electron microscopy-energy dispersive X-ray (TEM-EDX) analysis. It was confirmed that SPD formed a segregated structure in the Cu-In-S layers and the Cu-In-S structure differed between substrates.

2. Experimental

Cu-In-S films were deposited on substrates at 300°C in air, by SPD. The substrates were glass, $\langle glass/TiO_2 \rangle$, and $\langle glass/TiO_2/In_2S_3 \rangle$. Figure 1 shows the fabrication processes for the Cu-In-S layer and the resulting Cu-In-S structures. The glass substrates were coated with a TiO_2 layer ($t = 100$ nm) by SPD at 400°C. The solution used for depositing the TiO_2 compact layer was a mixture of titanium acetylacetonate (TAA) and ethanol (9 : 1 v/v). TAA was prepared by slowly injecting acetylacetone (99.5%, Kanto Chemical Co. Inc., Tokyo, Japan) into titanium tetraisopropoxide (97%, Kanto Chemical Co. Inc.) at a mole ratio of 2 : 1. The In_2S_3 layers ($t = 100$ nm) were used as the buffer layers and deposited using a precursor solution of $InCl_3$ (10 mM) and thiourea (20 mM) in water (10 mL) at 300°C. The Cu-In-S spray deposition was performed using an aqueous solution of $CuCl_2 \cdot 2H_2O$ (30 mM; 97.5%, Kanto Chemical Co.), $InCl_3$ (30 mM; 98%, Kishida Chemical Co., Ltd, Japan) and thiourea (150 mM; Tokyo Chemical Industry Co., Ltd, Tokyo, Japan) giving a Cu/In/S ratio of 1 : 1 : 5. The Cu-In-S absorber layer was deposited by spraying the Cu-In-S SPD solution (40 mL) on to each substrate at 300°C at a speed of 2 mL min^{-1}. The Cu-In-S layers were scratched
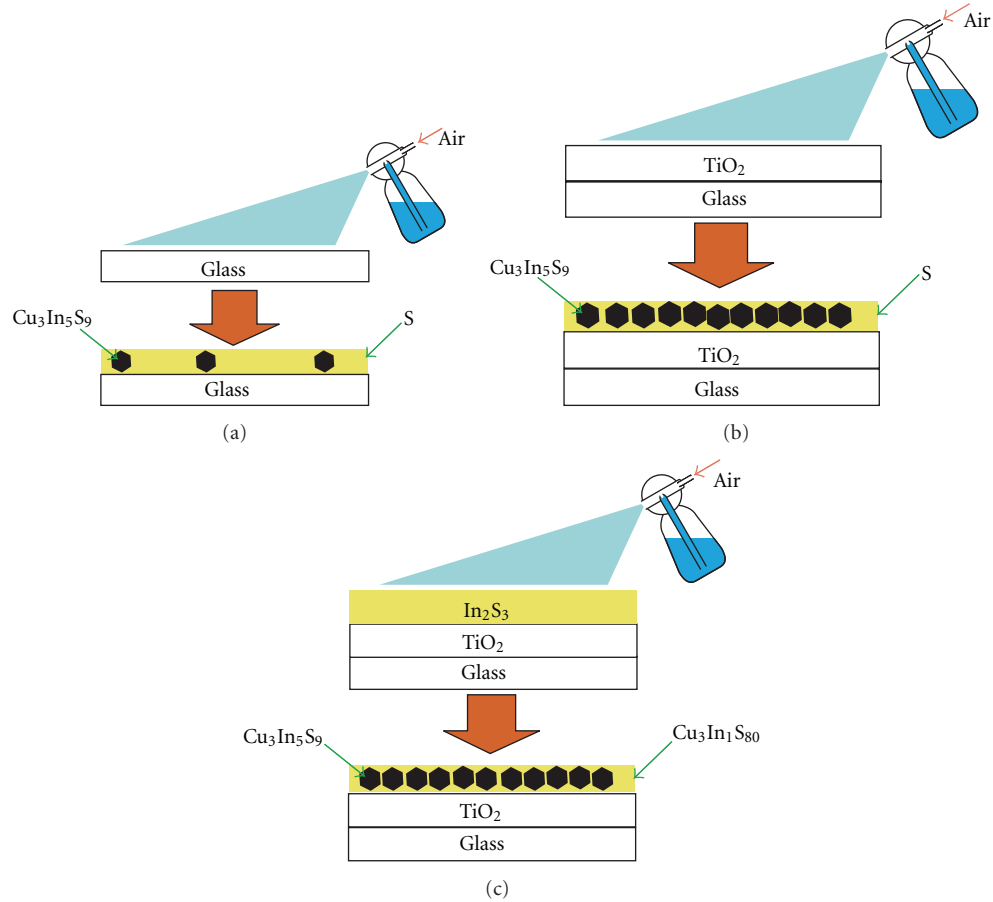
Figure 1: Relations between substrates, (a) glass, (b) glass/TiO_2, and (c) glass/TiO_2/In_2S_3, and the structures of spray-pyrolysis-deposited Cu-In-S.

from the substrates and powdered, dispersed in ethanol, and attached to Mo grids for TEM observation. A TEM-EDX system (JEOL JEM2100) was used to characterize the Cu-In-S materials. XPS analysis conducted previously showed an oxidation state just on the Cu-In-S surface [5]. Thus, the powdered Cu-In-S samples for TEM observation show the inside of the SPD layer.

SEM cross-section images showed that the surface is relatively flat [5] with a roughness factor of only 1. However, there were several pinholes due to dust and aggregates. Moreover, observation by atomic scale view indicated a very rough surface because it is not a single crystal layer, hence the superstrate-type structure of the solar cells has been fabricated.

The back contact electrode formed from an Au layer deposited by vacuum evaporation produced superstrate-structured solar cells ⟨glass/F-doped SnO$_2$ (FTO)/TiO$_2$/ Cu-In-S/Au⟩. The samples used to obtain the photo I-V curve were 5 mm × 5 mm. The photovoltaic measurements employed an AM 1.5 solar simulator equipped with a xenon lamp (YSS-100A, Yamashita Denso, Japan). The power of the simulated light was calibrated to 100 mW cm^{-2} by using a reference Si photodiode (Bunkou Keiki, Japan). The I-V curves were obtained by applying an external bias to the cell

and measuring the generated photocurrent with a DC voltage current source (6240, ADCMT, Japan). It is very important to obtain information regarding the electrical properties of samples on various substrates for the preparation of Cu-In-S solar cells. However, since the resistance of the Cu-In-S layer was very high, the electrical resistance and the Hall effects could not be measured.

3. Results and Discussion

Figure 2 shows the photo and dark I-V curves for the superstrate-structured solar cell ⟨glass/FTO/TiO$_2$/In$_2$S$_3$/ Cu-In-S/Au⟩ fabricated by SPD. The crossing of the curves suggests double-diode effects in the CIS solar cells. The open-circuit photovoltage, the short-circuit photocurrent density, the fill factor, and the conversion efficiency were 0.521 V, 9.68 mA cm^{-2}, 0.423, and 2.14%, respectively, and were improvements compared with our previous report [5], obtained by optimizing the SPD conditions. The conversion efficiency is far removed from the best Cu-based solar cells (20.1%) [1]; however, if the efficiency of SPD-processed solar cells can be enhanced by over 10% in the near future, this would be a very significant improvement due to the high-speed and nonvacuum processing methods used in
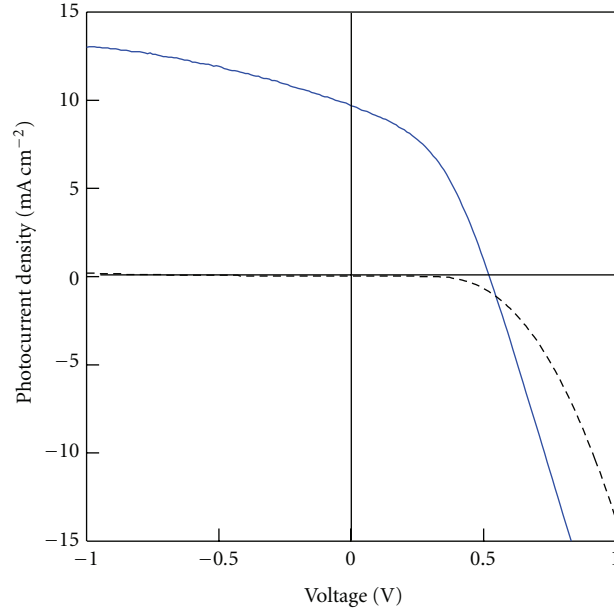
FIGURE 2: Photo (solid) and dark (dashed) *I-V* curves for the ⟨glass/FTO/TiO$_2$/In$_2$S$_3$/Cu-In-S/Au⟩ solar cell. The cell size was 5 mm × 5 mm, and the cell was irradiated with AM 1.5 (100 mW cm^{-2}) light.
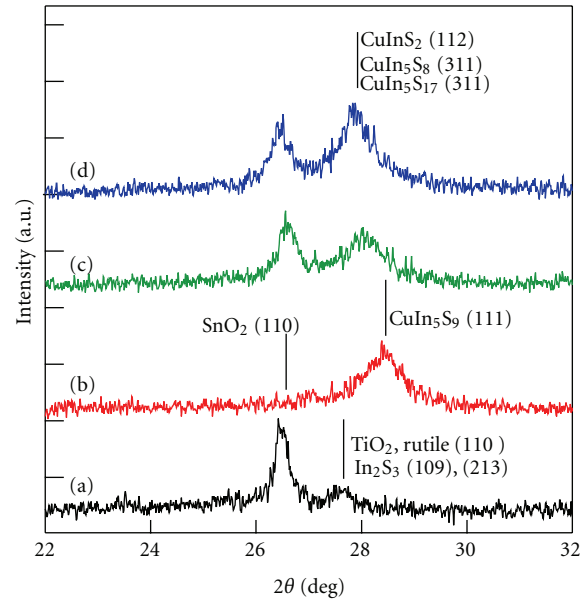
FIGURE 3: XRD patterns of ⟨glass/FTO/TiO$_2$/In$_2$S$_3$⟩ (a), ⟨glass/Cu-In-S⟩ (b), ⟨glass/FTO/TiO$_2$/Cu-In-S⟩ (c), and ⟨glass/FTO/TiO$_2$/In$_2$S$_3$/Cu-In-S⟩ (d). Numbers in round brackets show the crystal plane of materials in reference to JCPDS card data.

the fabrication of cost-effective solar cells. Thus, further investigation is required to improve the conversion efficiency. Here, we report changes in the CIS layer as observed by XRD and TEM-EDX.

Figure 3 shows the XRD patterns for the Cu-In-S layers on the different substrates that produced the ⟨glass/Cu-In-S⟩, ⟨glass/FTO/TiO$_2$/Cu-In-S⟩, and ⟨glass/

FTO/TiO$_2$/In$_2$S$_3$/Cu-In-S⟩ structures. The peak at 26.4° was attributed to SnO$_2$ (26.6° by JCPDS 88–0287) in FTO (Figure 3(a)); therefore, an SnO$_2$ peak was not observed in the XRD pattern of Cu-In-S on the glass substrate (Figure 3(b)). The peak at 27.6° in Figure 3(a) was assigned to In$_2$S$_3$ (27.4° by JCPDS 73–1366) and TiO$_2$ (27.7° by JCPDS 88–1173) and was not observed

(a)

(b)

FIGURE 4: TEM image of spray-pyrolysis-deposited Cu-In-S with the electron diffusion patterns (inset) on a glass substrate: (a) the major part and (b) the minor part.

(a)

(b)

FIGURE 5: TEM image of spray-pyrolysis-deposited Cu-In-S with the electron diffusion patterns (inset) on a glass/TiO_2 substrate: (a) the major part and (b) the minor part.

TABLE 1: The atomic ratios of Cu-In-S analyzed by TEM-EDX. Each location is indicated by the relevant figure number.

Substrate	Major/Minor	Cu	In	S	Figures
⟨glass⟩	Major	0.06	0.00	99.94	Figure 4(a)
	Minor	16.00	28.41	55.58	Figure 4(b)
⟨glass/TiO_2⟩	Major	16.49	30.49	53.02	Figure 5(a)
	Minor	0.19	0.25	99.56	Figure 5(b)
⟨glass/TiO_2/In_2S_3⟩	Major	17.85	29.51	52.65	Figure 6(a)
	Minor	3.78	1.17	95.05	Figure 6(b)

in the ⟨glass/FTO/TiO_2/In_2S_3/Cu-In-S⟩ (Figure 3(c)) and ⟨glass/FTO/TiO_2/In_2S_3/Cu-In-S⟩ (Figure 3(d)) XRD patterns. Hence, the In_2S_3 layer had diffused into the Cu-In-S layer, confirmed by EPMA mapping analysis of the cross-sectional image [5]. The TiO_2 peak was buried below the Cu-In-S layer (Figure 3(c)) because of the very thin TiO_2 layer (t = 200 nm) and made evident by the small XRD signal.

Although the positions of the peaks were very close to the $CuInS_2$ peak (27.9° by JCPDS: 85–1575), the Cu-In-S XRD peaks (27.8–28.4°) varied significantly among substrates (Figures 3(b)–3(d)) and the peak shifts suggested variations in the types of Cu-In-S crystals. Due to the large

ratio of sulfur in the Cu-In-S layer (Cu-poor), which will be addressed in the TEM-EDX discussion to follow, assignment of the peaks from 27.8° to 28.4° in Figures 3(b)–3(d) would be $CuIn_{11}S_{17}$ (27.7° by JCPDS: 34–0797), $CuIn_5S_8$ (27.7° by JCPDS: 72–0956), and $CuIn_5S_9$ (28.4° by JCPDS: 49–1383). Therefore, it was thought that the peak shifts may be due to variations in the Cu-In-S crystals, which are projecting the compositions of the Cu-In-S.

The elemental analysis of Cu-In-S by TEM-EDX is shown in Table 1 and the locations analyzed are shown in Figures 4, 5, and 6. The Cu-In-S samples for TEM-EDX analysis were taken from the layers deposited on the different substrates: glass, glass/TiO_2, and glass/TiO_2/In_2S_3. It was confirmed that the Cu-In-S elements were segregated in the SPD layer. The components of the Cu-In-S materials were $CuInS_2$, $Cu_3In_5S_9$, $Cu_2In_4S_7$, $CuIn_3S_5$, and $CuIn_5S_8$ [9] with atomic ratios calculated as 25.00 : 25.00 : 50.00, 17.65 : 29.41 : 52.94, 15.38 : 30.77 : 53.85, 11.11 : 33.33 : 55.56, and 7.14 : 35.71 : 57.14, respectively. Therefore, the Cu-poor and In-rich portions of the segregated Cu-In-S layer were close to the composition ratio of $Cu_3In_5S_9$.

Figure 4 shows the TEM images of Cu-In-S deposited on a glass substrate. It was confirmed that, although the spray-pyrolysis solution for the Cu-In-S layer contained a

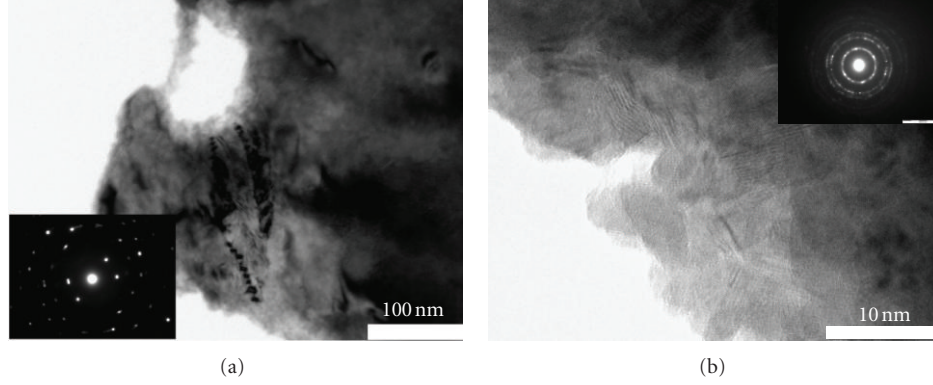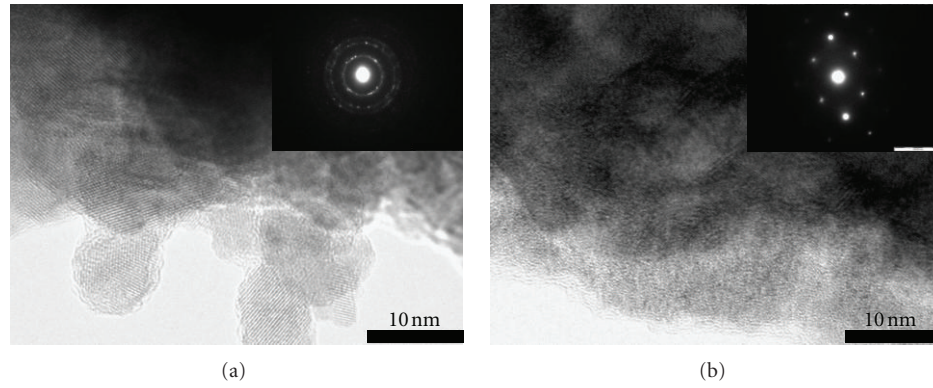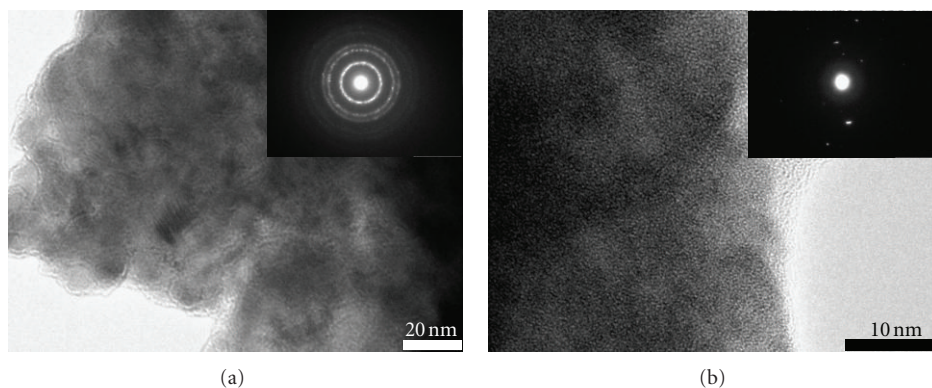(a)   (b)

Figure 6: TEM image of spray-pyrolysis-deposited Cu-In-S with the electron diffusion patterns (inset) on a glass/TiO$_2$/In$_2$S$_3$ substrate: (a) the major part and (b) the minor part.

significant amount of copper and indium, the layer on the glass substrate was mainly pure sulfur (Figure 4(a), Table 1). The sulfur particles were several hundred nanometers in size. The atomic lattice was not visible in the TEM images because sulfur is much lighter than the heavy metal elements. However, the electron scattering patterns showed a single crystal (inset, Figure 4(a)). A small number of nanoparticles around 10 nm in diameter were observed (Figure 4(b)) and revealed the atomic lattice because they contained metallic elements. The electron sputtering pattern (inset, Figure 4(b)) suggested the existence of a polycrystalline structure. EDX analysis indicated that the Cu-In-S elemental ratio was close to Cu$_3$In$_5$S$_9$. Hence, a considerable amount of the copper metal source (CuCl$_2$) did not end up in the Cu-In-S layer and was dispersed somewhere else during SPD. The structure of the Cu-In-S layer (Figure 1(a)) shows the segregated Cu$_3$In$_5$S$_9$ particles in the sulfur layer.

Figure 5 shows the TEM images of Cu-In-S deposited on a glass/TiO$_2$ substrate. In contrast to the glass substrate (Figure 4), most of the Cu-In-S layer consisted of Cu$_3$In$_5$S$_9$ nanocrystals, 10 nm in diameter (Figure 5(a)). The electron diffraction pattern also suggested it had a nanocrystalline structure. Again the heavy metal elements meant that the nanocrystal atomic lattice could be observed. Although the nanocrystals contained copper, the Cu/In ratio was only 0.54 : 1, which was half that of the setting ratio (1 : 1) in the spray-deposition solution. The CuCl$_2$ in the Cu-In-S solution was again dispersed and not deposited in the Cu-In-S layer. In the minor part of Cu-In-S layer, a small amount of copper was observed (Figure 5(b)). However, when the substrate was changed from glass to glass/TiO$_2$, the amount of metal ([Cu + In]/[Cu + In + S]) in the sulfur rich part increased from 0.06% (Figure 4(a)) to 0.44% (Figure 5(b)). The electron scattering suggested a single crystal (inset, Figure 5(b)), although an atomic lattice was not observed, which may be because sulfur is a light element. Therefore, it was concluded that the substrate (⟨glass⟩ or ⟨glass/TiO$_2$⟩) significantly affected the composition and structure of the spray-pyrolysis-deposited CuInSe$_2$ layer. The structure of Cu-In-S layer deposited on the glass/TiO$_2$ substrate by spray pyrolysis is shown in Figure 1(b).

Figure 6 shows the TEM images of Cu-In-Se deposited on a glass/TiO$_2$/In$_2$S$_3$ substrate. The atomic ratio showed that, for Cu-In-Se, the layer mainly consisted of Cu$_3$In$_5$S$_9$ (Figure 6(a)), although a small amount of Cu$_3$In$_1$S$_{80}$ (Figure 6(b)) was present. Pure sulfur (Figures 4(a) and 5(b)) was not observed because of the In$_2$S$_3$ buffer layer and interdiffusion to the upper Cu-In-S layer. Cu$_3$In$_5$S$_9$ was present as nanocrystals, around 10 nm in diameter (Figure 6(a)), and the electron diffraction pattern suggested a polycrystalline structure (inset, Figure 6(a)). The Cu$_3$In$_1$S$_{80}$ particles were around several hundred nanometers in size (Figure 6(b)) and the atomic lattice was not visible because of the light sulfur atoms, although the electron diffraction pattern suggests a single-crystalline structure (inset, Figure 6(b)). Therefore, Cu-In-S was segregated as Cu$_3$In$_5$S$_9$ and Cu$_3$In$_1$S$_{80}$. The structure of the Cu-In-S layer deposited on the glass/TiO$_2$/In$_2$S$_3$ substrate by spray pyrolysis is shown in Figure 1(c).

The ratios of Cu-In-S, such as Cu$_3$In$_5$S$_9$ and Cu$_3$In$_1$S$_{80}$, simply show integral multiplication of the TEM-XRD results of Table 1. From a scientific point of view, the crystal structures should be revealed by XRD analysis. However, the results from normal XRD were obscure and GIXRD may be a more suitable method. Nevertheless, although GIXRD may have provided better results, the Cu-In-S was a mixture of small crystals and amorphous phases of different Cu-In-S compositions, making crystal identification in this work very complicated. It would be desirable to improve the analytical methods in the future.

4. Conclusions

Compound solar cells based on Cu-In-S (CIS) were prepared by SPD under air. Although the Cu-In-S layer had a segregated structure, the solar cells had a 9.68 mA cm^{-2} short-circuit photocurrent density and 2.14% conversion efficiency. The segregated structures differed among substrates. The resulting Cu-In-S layers were copper poor due to the loss of CuCl$_2$ during SPD. Therefore, the next step in improving the conversion efficiency is to control the amount of copper in the Cu-In-S layer. Since the significance of the

contribution of a Cu-poor CuInS$_2$ and CuInSe$_2$ solar cells has been discussed in the publications [10, 11], we believe that a Cu-poor CuInS$_2$ layer, and hence the presence of Cu$_3$In$_5$S$_9$, may contribute to the photovoltaic effects.

Samples prepared for this kind of work may be solid mixtures of CuInS$_2$, CuIn$_3$S$_5$, and so on and should be clearly identified. Each major part of the sample was expressed in the TEM figures in this paper. It is very difficult to obtain the exact components of such segregated materials by other methods, such as XPS, Auger, SIMS, Raman, XRD, and EPMA, because the resolutions in these methods reach the submicron range and give mixed information about major and minor parts of the materials. Advancements in the analytical tools may reveal further details in the future.

Acknowledgment

References

[1] P. Jackson, D. Hariskos, E. Lotter et al., "New world record efficiency for Cu(In, Ga)Se$_2$ thin-film solar cells beyond 20%," *Progress in Photovoltaics: Research and Applications*, vol. 19, no. 7, pp. 894–897, 2011.

[2] B. M. Sager, D. Yu, and M. R. Robinson, "Coated nanoparticles and quantum dots for solution-based fabrication of photovoltaic cells," US Patent, US7, 306, 823 B2, 2007.

[3] T. Wada, Y. Matsuo, S. Nomura et al., "Fabrication of Cu(In,Ga)Se$_2$ thin films by a combination of mechanochemical and screen-printing/sintering processes," *Physica Status Solidi (A)*, vol. 203, no. 11, pp. 2593–2597, 2006.

[4] M. Nanu, J. Schoonman, and A. Goossens, "Nanocomposite three-dimensional solar cells obtained by chemical spray deposition," *Nano Letters*, vol. 5, no. 9, pp. 1716–1719, 2005.

[5] T. Ryo, D. C. Nguyen, M. Nakagiri, N. Toyoda, H. Matsuyoshi, and S. Ito, "Characterization of superstrate type CuInS$_2$ solar cells deposited by spray pyrolysis method," *Thin Solid Films*, 2011.

[6] V. K. Kapur, A. Bansal, P. Le, and O. I. Asensio, "Non-vacuum processing of CuIn$_{1-x}$Ga$_x$Se$_2$ solar cells on rigid and flexible substrates using nanoparticle precursor inks," *Thin Solid Films*, vol. 431-432, pp. 53–57, 2003.

[7] Y. Oda, M. Matsubayashi, T. Minemoto, and H. Takakura, "Crystallization of In-Se/CuInSe$_2$ thin-film stack by sequential electrodeposition and annealing," *Journal of Crystal Growth*, vol. 311, no. 3, pp. 738–741, 2009.

[8] D. Lincot, J. F. Guillemoles, S. Taunier et al., "Chalcopyrite thin film solar cells by electrodeposition," *Solar Energy*, vol. 77, no. 6, pp. 725–737, 2004.

[9] T. Halboom, T. Godecke, F. Ernst et al., "Phase relations and microstructure in bulk materials and thin films of the ternary system Cu-In-Se," in *Proceedings of the 11th International Conference on Ternary and Multinary Compounds*, pp. 249–252, Institute of Physics, Salford, UK, 1997.

[10] T. Watanabe, H. Nakazawa, M. Matsui, H. Ohbo, and T. Nakada, "The influence of sodium on the properties of CuInS$_2$ thin films and solar cells," *Solar Energy Materials and Solar Cells*, vol. 49, no. 1–4, pp. 357–363, 1997.

[11] R. Kaigawa, A. Ohyama, T. Wada, and R. Klenk, "Electric properties of Cu-poor and Cu-rich Cu(In,Ga)S$_2$ films after O$_2$-annealing," *Physica Status Solidi (C)*, vol. 3, no. 8, pp. 2568–2571, 2006.

Research Article

Series Resistance Analysis of Passivated Emitter Rear Contact Cells Patterned Using Inkjet Printing

Martha A. T. Lenio,[1] James Howard,[1] Doris (Pei Hsuan) Lu,[1] Fabian Jentschke,[2] Yael Augarten,[1] Alison Lennon,[1] and Stuart R. Wenham[1]

[1] *Electrical Engineering Department, School of Photovoltaic and Renewable Energy Engineering,*
 University of New South Wales, Sydney, NSW 2052, Australia
[2] *Energy Australia, Sydney, NSW 2001, Australia*

Correspondence should be addressed to Martha A. T. Lenio, m.lenio@student.unsw.edu.au

For higher-efficiency solar cell structures, such as the Passivated Emitter Rear Contact (PERC) cells, to be fabricated in a manufacturing environment, potentially low-cost techniques such as inkjet printing and metal plating are desirable. A common problem that is experienced when fabricating PERC cells is low fill factors due to high series resistance. This paper identifies and attempts to quantify sources of series resistance in inkjet-patterned PERC cells that employ electroless or light-induced nickel-plating techniques followed by copper light-induced plating. Photoluminescence imaging is used to determine locations of series resistance losses in these inkjet-patterned and plated PERC cells.

1. Introduction

As the photovoltaics industry becomes more mature, manufacturers must find new ways of staying competitive. Developing cost-effective ways of fabricating higher-efficiency cell structures that have to date only been realized in a laboratory environment is an option that is being considered by many. An obvious cell structure to attempt to commercialise is the Passivated Emitter Rear Contact (PERC) cell [1, 2].

New patterning methods such as inkjet printing and laser doping [3–5] enable the patterning of dielectric layers for metal contacting and therefore eliminate the need to use techniques such as photolithography which enabled the earlier laboratory implementations of these cells. Metal plating, which has been successfully used for the manufacture of photovoltaic devices in industry [6], is compatible with these patterning methods and consequently presents as a commercially viable metallization method. In addition to enabling the use of less expensive metals like Ni and Cu, metal plating is a self-aligning process thus eliminating the need for the photolithographic lift-off steps which were used

in conjunction with evaporated Ti-Pd-Ag metal contacts. A further advance that is desirable to make PERC cells commercially viable is to reduce the number of high temperature steps [7, 8].

This paper contains an analysis of the series resistance losses of PERC cells that have been fabricated using inkjet printing (IJP) for the patterning steps and self-aligned Ni and Cu plating for the metallization. The fabricated PERC cells were analyzed using photoluminescence (PL) imaging, current-voltage (IV) measurements, and microscopy. Transmission line model (TLM) test structures were fabricated to characterize the metal-silicon interface and estimate the contact resistance associated with both the front and rear metal contacts. The findings of this work show that a decrease in fill factor due to high series resistive losses is a problem with electrolessly plated PERC cells. This is consistent with the findings of other researchers who have seen fill factor losses in their electrolessly plated PERC cells that were formed using laser-fired rear contacts [9]. It was found here that spurious Ni plating on the rear point contacts forms during electroless Ni plating, and this contributes

significantly to the high series resistance and resulting low fill factors of final devices. Poorly adhered front contacts were also an issue with inkjet-printed and electrolessly plated PERC cells. It is shown that use of appropriate plating techniques, such as bias-assisted light induced plating, can help reduce these resistive effects.

2. Experimental Procedure

2.1. Cell and Test Structure Fabrication. Cells and test structures were fabricated on planar, $0.5\,\Omega\cdot$cm, p-type, $200\,\mu$m thick, FZ Si wafers. The processing sequence used for the cells is outlined in Table 1. The emitter sheet resistance after processing was $\sim120\,\Omega/\square$. Nickel contacts were formed using both electroless plating and bias-assisted LIP. In the latter process, a bias voltage of 0.6 V was applied to the rear Al surface of the devices (this setup can be seen in Figure 1(a)). All Cu plating was performed using noncontact LIP without an applied bias (see Figure 1(b)).

The dimensions of the completed cells are detailed in Table 2. The TLM test structures underwent the same thermal processing as the fabricated cells. The only difference in the fabrication sequence was the inkjet patterning. Instead of forming openings for front finger grids and rear point contacts, TLM contact pads were patterned using the indirect inkjet patterning method [5] for the (front) Ni and (rear) Al contact resistance test structures. For the rear measurements, TLM contact pads of Al were evaporated through a mask which was aligned to the inkjet-patterned openings in the rear SiO$_2$ dielectric layer.

2.2. Analysis. The series resistance of the final IJP PERC cells was estimated from comparing the light-IV measurements with the Suns-V_{oc} measurements [10]. Photoluminescence (PL) imaging was used to record a spatially resolved image of the voltage across the cells. Two types of PL imaging were used: open-circuit PL and R_s-PL [11, 12]. The contributing components of the series resistance were identified, and each component was calculated using actual dimensions and resistances measured from test structures. Scanning electron microscope (SEM), focused ion beam (FIB), and optical microscopy were used to inspect the quality of the metal contacts and to help determine the underlying causes of the high series resistance problems experienced by IJP PERC cells.

3. Results and Discussion

3.1. Contact Resistance Results. The TLM measurements for the front Ni contacts depended on the plating technique used, with the average specific contact resistivity being $0.07 \pm 0.04\,\Omega\cdot$cm^2 and $0.09 \pm 0.02\,\Omega\cdot$cm^2 for electroless Ni and bias-assisted LIP Ni contacts, respectively. There were some variations between individual test structures using the same Ni-plating technique, particularly with the electroless Ni-plated cells. Specific contact resistivities as low as $3.5 \times 10^{-5}\,\Omega\cdot$cm^2 have been reported previously for Ni/Cu-plated fingers [19]. The discrepancy between the resistivity values

could be due to the difficulty experienced in achieving good adhesion between the Ni and Si.

The specific contact resistivity for the Al-Si rear contact TLM test structures was measured to be $0.004 \pm 0.003\,\Omega\cdot$cm^2 and $0.028 \pm 0.010\,\Omega\cdot$cm^2, before and after electroless Ni plating, respectively. The value before electroless Ni plating is higher but on the same order of magnitude as previously reported values of $0.0015\,\Omega\cdot$cm^2 for Al on $0.5\,\Omega\cdot$cm p-type Si [18, 20, 21]. The increase in specific contact resistivity after electroless plating was due to spurious Ni plating at the Al-Si rear contacts [18]. Figure 2 shows an FIB image of Ni plated around a rear point contact on an IJP PERC cell that underwent electroless Ni plating. Nickel plates preferentially on the rear surface at regions where the Al is rough or contains a higher Si content than the surrounding Al [18]. In some areas, the Ni displaces the Al through galvanic displacement, coming into direct contact with the Si (see Figure 3). This plated Ni contributes to the metal Si contact and causes increased contact resistance due to the fact that Ni has a higher barrier height on p-type Si than Al [20].

The spurious rear-side Ni plating was only observed with cells and test structures which underwent electroless Ni plating. In bias-assisted LIP, the rear surface was protected from undesired plating by the bias voltage, and so rear-side plating was avoided. The absence of Ni on the rear contacts means that the Al-Si contact resistance measured from the test TLMs can be used as the contact resistance for rear contacts formed using BA-LIP.

3.2. Light IV Results. The cells were tested under standard conditions using an Adventest DC Voltage Current Source/Monitor, a temperature-controlled copper block, and a halogen lamp light source calibrated to one-sun using a calibrated reference cell. Suns-V_{oc} measurements were done using a flash tester, and the series resistance was estimated from comparing the light IV data to the Suns-V_{oc} data. The open-circuit voltage (V_{oc}), fill factor (FF), series resistance (R_s), and shunt resistance (R_{sh}) data for the cells plated using electroless Ni and BA-LIP Ni are listed in Table 3. The series resistance of the electroless Ni-plated cell was higher than that measured in the BA-LIP Ni-plated cell. The FFs of both cells are remarkably low. Shunting was an issue particularly for the BA-LIP sample, and the series resistance was high for both cells. The shunting in the BA-LIP batch of samples was due to inadequate resist coating on the front surface of the cell during the rear contact patterning step. Pinholes formed, creating holes through the dielectric and emitter which were subsequently plated with metal.

3.3. Photoluminescence Results. Photoluminescence imaging gives a spatially resolved image of locations of high and low voltages within a cell or wafer. When the cell is at open circuit, there is no lateral current flow, so areas of low voltage represent areas of high recombination. The PL intensity is directly proportional to the exponential of the voltage according to (1) [22]:

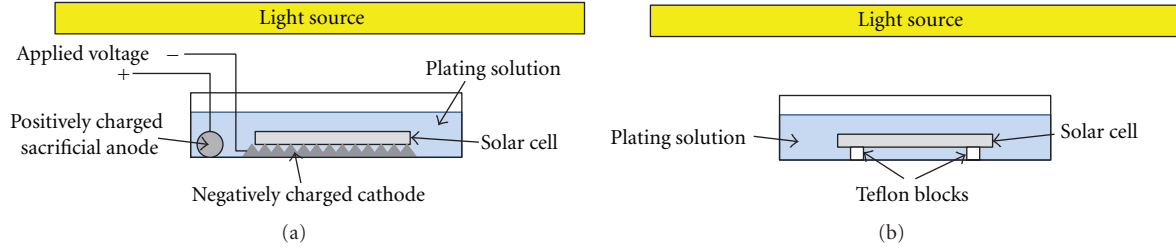$$I_{\mathrm{PL},i} = C_i \exp\left(\frac{eU_i}{kT}\right), \tag{1}$$

FIGURE 1: Experimental setup for (a) bias-assisted LIP; (b) noncontact LIP.

TABLE 1: Processing sequence for IJP PERC cells.

Step	Process	Conditions
(1)	Damage etch/texture	20 min etch in 30% NaOH at 80°C
(2)	Oxidation	Dry oxidation, 1030°C for 4 hr with 1% TCA in O_2
(3)	Strip front oxide	Mask rear; strip SiO_2 with buffered HF
(4)	Emitter diffusion + oxidation	Diffusion: P solid source, 850°C, 15 min Oxidation: 1100°C, 5 hr, 1% TCA in O_2, 15 min anneal in N_2
(5)	IJP the front contacts	Indirect IJP method [5]
(6)	Groove diffusion + drive-in	Diffusion: P solid source, 940°C, 90 min Drive-in: 1000°C, 3 hr, N_2
(7)	IJP the rear contacts	Indirect IJP method [5]
(8)	Evaporate rear Al + sinter	1-2 μm Al, sinter at 400°C, 30 min in forming gas
(9)	Ni plate + anneal	Various plating methods; anneal at 400°C, 10 min in forming gas
(10)	Cu light-induced plate	Cu electroplating solution, 5 min under high-intensity fluorescent light
(11)	Edge isolation	Cut with a 1064 nm Nd : YAG laser from the rear; cut 1/2 way thru wafer then snapped

Ni plating was done in one of two ways: (i) electroless Ni using Transene EN solution [9], 80°C for 3 min; or (ii) BA-LIP Ni, 25–30°C for 30 s under high-intensity fluorescent light. The BA-LIP Ni consisted of Watt's solution in the ratios 10 g Ni_2SO_4, 20 g $NiCl_2$, 4 g boric acid in 100 mL deionized water [13]. The electroplating solution for the Cu plating used 12 g $CuSO_4$, 11 mL H_2SO_4, and 50 mL deionized water.

TABLE 2: Dimensions for cell design and analysis.

Parameter	Value	Variability
Cell area	8 cm^2	±0.15 cm^2
Finger width	90 μm	±10 μm
Finger height	5 μm	±2 μm
Finger length	28 mm	±0.5 mm
Finger spacing	1.2 mm	±10 μm
Rear contact diameter	100 μm	±10 μm
Rear contact spacing	1.5 mm	±10 μm

where $I_{PL,i}$ is the PL intensity at a specific location i, U_i is the voltage at that location, and C_i is a local calibration constant. With an open circuit PL image, the calibration constant can be calculated using the V_{oc} obtained from the light IV measurement along with the average PL signal from the PL image [22]. This then allows the voltage at any particular point in the image to be calculated from the PL signal.

Figure 4(a) shows an open-circuit PL image of an inkjet-patterned PERC cell that had its front metal contacts formed using electroless Ni plating followed by LIP Cu plating. The rear point contacts can be clearly seen in this image. At open circuit, with no current extraction occurring, locations of
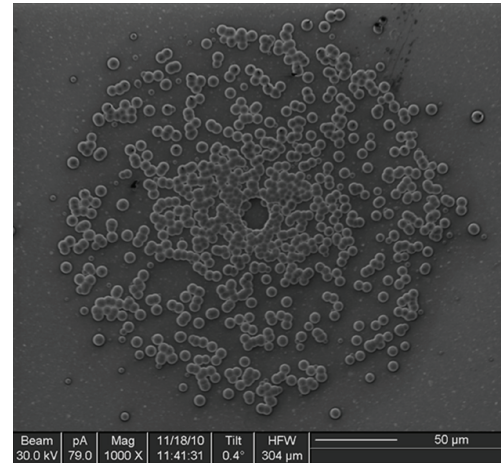

FIGURE 2: Focused ion beam (FIB) image of the rear of a test cell. Unwanted Ni plating can be seen around a rear point contact on an IJP PERC cell plated using electroless Ni [18].

low voltage must be due to either shunts or high recombination (low lifetime). Some shunts are apparent, as larger dark spots in a few locations on the wafer, but the regular

TABLE 3: Cell performance from light IV data.

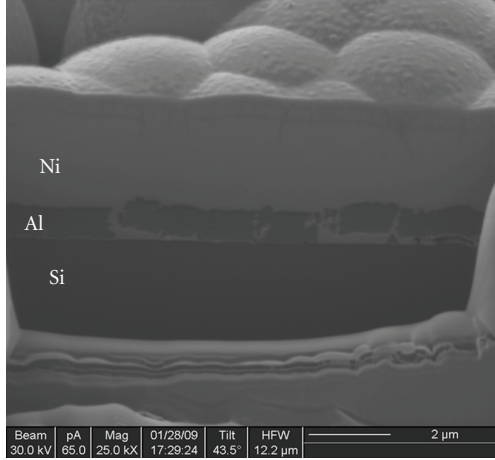| Ni-plating method	V_{oc} (mV)	Fill factor	Series resistance ($\Omega \cdot cm^2$)	Shunt resistance ($k\Omega \cdot cm^2$)
Electroless Ni	646	0.61	4.1	42.7
Bias-assisted LIP Ni	617	0.59	1.5	0.10

FIGURE 3: Focused ion beam (FIB) cross-section image of the rear contact of a test cell. Unwanted electroless Ni plating at the rear point contact has displaced some of the Al, contacting the Si surface and increasing the contact resistance [18].

rear contact design is also seen as a regular, shadowy pattern across the entire wafer. These contact locations are necessarily identified as locations of high recombination as a result.

Figure 4(b) shows the series resistance PL image of an electroless Ni-plated cell. In this image, bright areas indicate regions of high series resistance. Prominent features are the bright areas on the left and right edges of the cell, as well as the two darker regions spreading out from the busbar, again to the left and right sides of the cell. The bright regions on the very edges are regions of high series resistance caused by the edge cleave being too far away from the front contact grid. This can be easily corrected with more careful processing. The dark regions spreading out from the busbar indicate that the series resistance in these areas increases as you move away from the busbar—the resistance is limited by the line resistance of the fingers. In the centre, the whole area is orange (high resistance—about $6 \Omega \cdot cm^2$) which is likely due to poor contact between the Ni and the Si, creating a high resistance everywhere. The average series resistance of this cell measured from the PL image data is $5.25 \Omega \cdot cm^2$.

Figure 5(a) shows the open-circuit PL image for a cell fabricated using BA-LIP Ni and LIP Cu. The rear point contacts are no longer visible, indicating that the recombination at the contacts is less than it was for the electrolessly Ni-plated cells.

Figure 5(b) shows the series resistance PL image of the same BA-LIP Ni-plated cell. Due to both the decreased resistive losses at both the front and rear contacts, it was expected that the total R_s of bias-assisted LIP Ni cells would be less than the electroless Ni-plated cells, and this is in fact

the case. There are fewer bright regions on this sample, with an average series resistance of $2.9 \Omega \cdot cm^2$ being measured using this method (IV measurements indicate $1.48 \Omega \cdot cm^2$— the discrepancy between the measurements may be due to the low shunt resistance affecting the R_s calculation from the IV data). Some high resistance is again seen at the edge of the cell, due to the edge cleave again being too distant from the front contact grid. One finger peeled off the front, and this region of slightly higher series resistance is highlighted by the blue circle, but in general this image shows a much more uniform resistance across the surface of the cell. This means that the contact between the Ni and Si that is formed through BA-LIP Ni plating is more uniformly good across the surface of the wafer.

3.4. Breakdown Analysis of Series Resistance. Figure 6 depicts the sources of series resistance in a PERC cell. The lateral resistance through the emitter (1), line resistance through the fingers (3), resistance through the base (4), and spreading resistance at the rear contacts (5) are all functions of the material properties and geometry, and as such can be estimated from theory. The contact resistances, at (2) and (6), require measurements to be performed, as the actual resistance at contact locations is often very different to the theoretically expected resistance [23].

Table 4 summarizes the total estimated series resistance contribution based on the theoretical and experimental calculations, as well as the associated power loss from each type of series resistance. The percent power loss was calculated using (2). Effective resistances must be calculated in order to use this equation as, for example, not the full current generated flows through the full sheet resistance. Details on how to calculate the individual effective resistances are provided in the appendix:

$$\%P_{loss} = \frac{P_{loss}}{P_{gen}} = \frac{I_{MP}^2 R_{eff}}{I_{MP} V_{MP}} = \frac{I_{MP} R_{eff}}{V_{MP}}. \quad (2)$$

As a percentage of total power loss, the rear point contacts are a major contributor to the overall series resistance on the electroless Ni-plated cells. For the cells Ni plated using BA-LIP, the calculated total resistance was within 1% of that estimated from the R_s-PL measurements. The value used for the rear contact resistance was that measured for an Al-Si contact after Ni plating; however, the FIB images show that there is also spurious Cu present at the rear contacts. As the calculated expected resistance is close to that measured, it is assumed that the spurious Cu did not have a significant impact on the series resistance of the finished devices.

For the cells where the Ni plating was achieved using electroless plating, the calculated total resistance is far greater than the resistance estimated from the IV measurements.
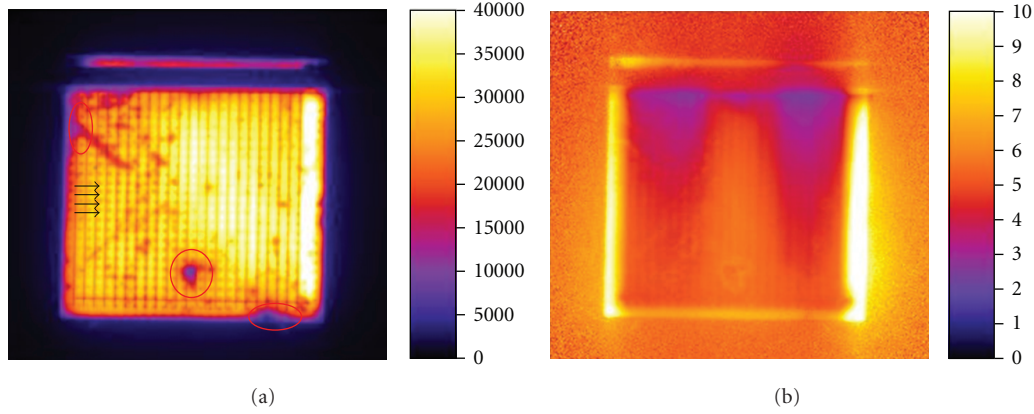
(a)

(b)

FIGURE 4: (a) Open-circuit PL image of a PERC cell made using EN and LIP Cu. The brighter the area, the higher the voltage in that location. The arrows highlight the locations of some of the rear point contacts, red circles are locations of shunts; (b) series resistance PL image of the same cell, bias voltage is −300 mV.

(a)

(b)
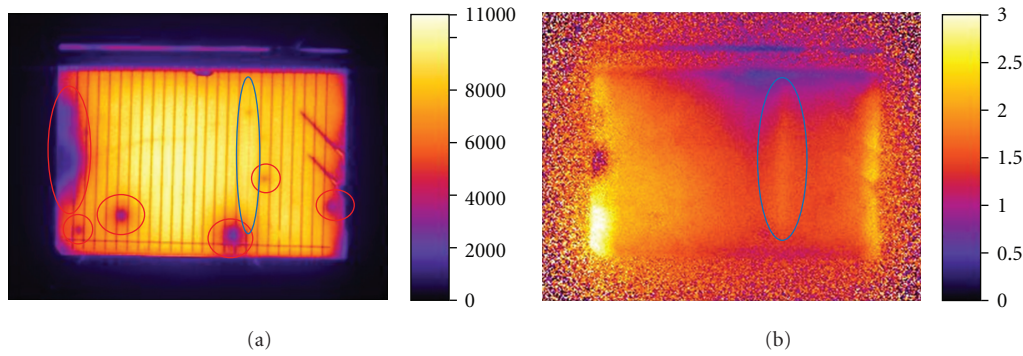
FIGURE 5: (a) Open-circuit PL image of a PERC cell fabricated using BA-LIP Ni and LIP Cu plating. The edges of the cell have been isolated with a laser. Red circles are shunt locations. Blue circle location of a peeled finger; (b) series resistance PL image of the same cell using a bias voltage of −300 mV.
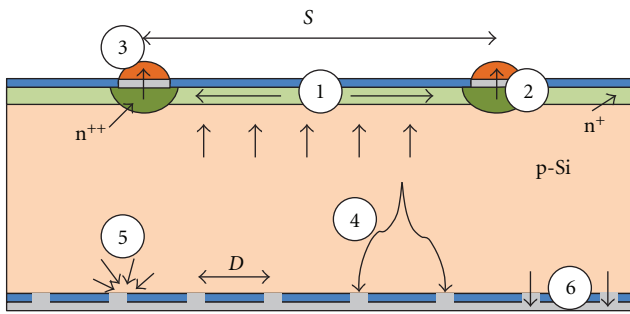
FIGURE 6: Locations of series resistance contributors in a PERC solar cell. S denotes the spacing between the front fingers, and D the spacing between the rear contact points. The length of the fingers is denoted by L (after [23]).

A worst-case scenario was used for the base contact resistance, as the variability in the contact resistance measurements can be great depending on how bad the spurious Ni on the rear is. Despite using the worst-case experimental values for ρ_c, the true value could be as low as 0.049 $\Omega \cdot cm^2$ contribution, resulting in a percent power loss of 2.5%.

The variation across the electroless plated Ni cells is thought to be due to the variation in the severity of the excess Ni plating that occurs from cell to cell.

Focused ion beam (FIB) was used to examine the test cell contacts in order to track down a cause of the high resistance in the cells plated using BA-LIP. The rear contacts exhibited some unwanted plating once again, but this time from the LIP Cu. Figure 7 shows a cross-section of a rear contact from a cell plated using bias-assisted LIP.

Light-induced plating is an equivalent technique to electroplating, with the plating voltage being supplied by the cell itself. As such, it was expected that Cu plating would only occur on the front surface. Cu plated to the rear, though, again in the locations around the rear point contacts. This is thought to be caused by local areas of relatively different voltage. At the rear surface, the Al is oxidizing due to electrons being drained to the front of the cell and driving the reduction of Cu at the front surface. However, the first Al to oxidize will be the Al that is in direct contact with the Si surface. The electrons will be taken from there first, and a voltage potential will form between the Al in contact with the Si and the Al that is floating on the dielectric. The reduction of hydrogen at cathodic sites on the rear surface

TABLE 4: Sources of series resistance.

Resistance source	Electroless Ni		Bias-Assisted LIP Ni	
	R_s ($\Omega \cdot cm^2$)	P_{loss}(%)	R_s ($\Omega \cdot cm^2$)	P_{loss} (%)
Lateral resistance through the emitter	0.152	0.6	0.152	0.6
Line resistance along the fingers*	0.112	0.4	0.112	0.4
Resistance through the base*	0.072	0.3	0.072	0.3
Spreading resistance**	0.560	2.2	0.560	2.2
Front contact resistance	0.090	4.6	0.107	5.5
Rear contact resistance***	0.028	28.7	0.004	4.1
Total	**4.9**	**36.7**	**2.7**	**13.0**
Total measured R from IV	**4.1**		**1.48**	
Total measured R from R_s-PL	**5.3**		**2.9**	

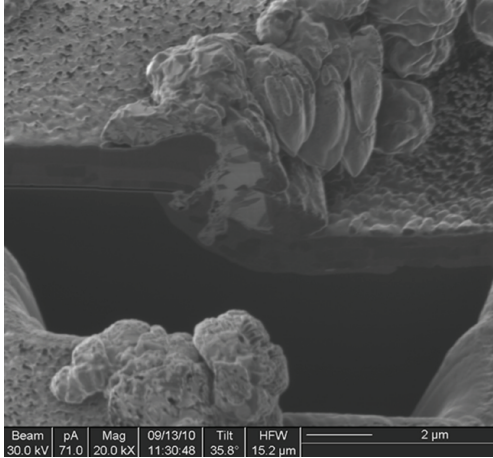* [14, 15].
** [16, 17].
*** From [18].

FIGURE 7: Focused ion beam (FIB) image of the rear of a BA-LIP Ni with LIP Cu test cell. Unwanted Cu plating can be seen at the edges of the rear point contacts.

can result in the formation of bubbles which can cause pitting and variations in surface potential [24]. Bias-assisted LIP of Cu where the rear surface is not in contact with the plating solution should address these issues. A number of commercial tool manufacturers are now developing BA-LIP tools which keep the Al rear surfaces of cells dry [25].

4. Summary and Future Research

In order to achieve higher-efficiency solar cells at lower cost, new fabrication methods such as inkjet patterning and metal plating may need to be considered. This research has identified and quantified the major series resistance losses inherent in the IJP PERC cell. The rear contact resistance of the Al-Si contacts is higher than expected for cells that were Ni plated using both electroless plating and BA-LIP. This results in higher series resistance and lower fill factors being achieved than is desirable. The specific contact resistivity of the these rear contacts in the electroless Ni-plated cells was an order of magnitude greater than for the cell plated using

BA-LIP due to spurious plating of Ni in the regions of the rear contacts.

Future work should focus on methods of achieving low resistance contacts on the rear of the cell. Bias-assisted LIP tools which maintain the rear surface dry will be required to ensure that plated metals do not interfere the electrical properties of the rear contacts. In addition to the rear contact resistance, the rear spreading resistance also needs to be reduced. Ideally this would be achieved by spacing the contacts closer together; however, unless the contact regions are heavily doped to minimize the minority carrier concentration at the surface, the recombination in the device will be increased resulting in a lower device voltage. Future work can also focus on how to form doped rear contact regions, either through laser-fired contacts [2], laser doping [1, 3], or local Al BSFs formed by firing Al through openings in a rear passivation layer.

Appendix

The locations where series resistance occurs in the cell are shown in Figure 5. In this section, the calculations done for determining each portion of the series resistance are shown.

(A) Lateral Resistance through the Emitter. When calculating the series resistance as a result of the current flowing through the emitter, it is important to note that not all the current will see the full resistance; the current generated close to the contact fingers will have less distance to travel through the emitter and experience less resistance than current generated midway between two fingers. A proper summation of the current must be done in order to obtain the effective resistance contribution from the emitter. From [14, 15], the following equation can be used to determine the resistance contribution from the emitter:

$$R_{eff} = \frac{1}{3} \frac{S/2}{L} \frac{\rho}{t}, \qquad (A.1)$$

where S is the finger spacing, L is the length of the fingers, and ρ/t is the sheet resistance of the emitter. With an emitter sheet resistance of ~120 Ω/sq, the effective resistance

contribution of the emitter is calculated to be $0.019\,\Omega$. As the dimensions on all the test cells are the same, this is the expected contribution on all the wafers.

(B) Line Resistance along the Fingers. As with the emitter, not all the current flows through the full length of the fingers; the current generated close to the busbar will have less distance to travel through the metal than the current generated on the far side of the cell. As such, the geometry of the problem is the same, and the same equation that was used to calculate the effective series resistance for the emitter can be used for the fingers. In this case,

$$R_{\text{eff}} = \frac{1}{3}\frac{L}{W}\frac{\rho}{t}, \qquad (A.2)$$

where L is again the length of the fingers, W is the width of the fingers, ρ is the specific resistivity of the Cu, and t is the thickness of the Cu. From the dimensions and the resistivity of Cu being $16.78\,\text{n}\Omega\cdot\text{m}$, the effective resistance from the front fingers works out to be $0.014\,\Omega$.

(C) Resistance through the Base. The resistance contribution from the base can be calculated from:

$$R_b = \rho_b D, \qquad (A.3)$$

where ρ_b is the resistivity of the base and D is the spacing between the rear contacts [16]. From the geometry and a base resistivity of $0.5\,\Omega\cdot\text{cm}$, the resistance through the base material is $0.075\,\Omega\cdot\text{cm}^2$, and a total resistance contribution of $9.4\,\text{m}\Omega$.

(D) Spreading Resistance at the Rear Contacts. The spreading resistance at the base point contacts can be calculated from the geometry and the material properties of Si from:

$$R_{\text{sp}} = D^2\frac{\rho_b}{2d_c}, \qquad (A.4)$$

where ρ_b is the resistivity of the base, D is the spacing of the rear contacts, and d_c is the diameter of the rear contact [15, 16]. From the geometry and a base resistivity of $0.5\,\Omega\cdot\text{cm}$, the spreading resistance at the rear contacts works out to be $0.56\,\Omega\cdot\text{cm}^2$, and a total resistance of $0.07\,\Omega$.

(E) Contact Resistance. Contact resistance between the metal contacts and the Si was determined from TLM test structures, the details of which were given in Sections 3.1 and 3.4.

Acknowledgment

References

[1] Suntech Power Co. Ltd., http://www.suntech-power.com/.

[2] E. Schneiderlochner, R. Preu, R. Ldemann, and S. W. Glunz, "Laser-fired rear contacts for crystalline silicon solar cells," *Progress in Photovoltaics: Research and Applications*, vol. 10, no. 1, pp. 29–34, 2002.

[3] B. S. Tjahjono, L. Mai, Z. Hameiri et al., "High efficiency solar cell structures through the use of laser doping," in *Proceedings of the 22nd European Photovoltaic Solar Energy Conference*, pp. 966–969, Milan, Italy, 2007.

[4] R. Y. Utama, A. J. Lennon, M. A. Lenio et al., "Inkjet printing for high efficiency selective emitter silicon solar cells," in *Proceedings of the 22nd European Photovoltaic Solar Energy Conference*, pp. 1687–1690, Valencia, Spain, 2008.

[5] A. J. Lennon, R. Y. Utama, M. A. T. Lenio, A. W. Y. Ho-Baillie, N. B. Kuepper, and S. R. Wenham, "Forming openings to semiconductor layers of silicon solar cells by inkjet printing," *Solar Energy Materials and Solar Cells*, vol. 92, no. 11, pp. 1410–1415, 2008.

[6] T. Bruton, N. Mason, S. Roberts et al., "Towards 20% efficient silicon solar cells manufactured at 60 MWp per annum," in *Procceddings of the 3rd World Conference on Photovoltaic Energy Conversion*, pp. 899–902, Osaka, Japan, May 2003.

[7] A. Wang, *High efficiency PERC and PERL silicon solar cells [Ph.D. thesis]*, Department of Electrical Engineering, University of New South Wales, Sydney, Australia, 1992.

[8] M. Lenio, J. Howard, F. Jentschke, A. Lennon, and S. Wenham, "Design, fabrication and analysis of high efficiency inkjet printed passivated emitter rear contacted solar cells," in *Proceedings of the 37th IEEE Photovoltaic Specialists Conferenc (PVSC '11)*, Seattle, Wash, USA, 2011.

[9] M. Aleman, N. Bay, M. Fabritius, and S. Glunz, "Characterization of electroless nickel plating on silicon solar cells for the front side metallization," in *Proceedings of the 22nd European Photovoltaic Solar Energy Conference*, pp. 1590–1592, Milan, Italy, 2007.

[10] D. Pysch, A. Mette, and S. W. Glunz, "A review and comparison of different methods to determine the series resistance of solar cells," *Solar Energy Materials and Solar Cells*, vol. 91, no. 18, pp. 1698–1706, 2007.

[11] T. Trupke, E. Pink, R. A. Bardos, and M. D. Abbott, "Spatially resolved series resistance of silicon solar cells obtained from luminescence imaging," *Applied Physics Letters*, vol. 90, no. 9, Article ID 093506, 3 pages, 2007.

[12] H. Kampwerth, T. Trupke, J. W. Weber, and Y. Augarten, "Advanced luminescence based effective series resistance imaging of silicon solar cells," *Applied Physics Letters*, vol. 93, no. 20, Article ID 202102, 3 pages, 2008.

[13] Transene Company Inc., http://www.transene.com/.

[14] N. C. Wyeth, "Sheet resistance component of series resistance in a solar cell as a function of grid geometry," *Solid State Electronics*, vol. 20, no. 7, pp. 629–634, 1977.

[15] L. D. Nielsen, "Distributed series resistance effects in solar cells," *IEEE Transactions on Electron Devices*, vol. 29, no. 5, pp. 821–827, 1982.

[16] J. Zhao, A. Wang, and M. A. Green, "Series resistance caused by the localized rear contact in high efficiency silicon solar cells," *Solar Energy Materials and Solar Cells*, vol. 32, no. 1, pp. 89–94, 1994.

[17] B. Gelmont and M. Shur, "Spreading resistance of a round ohmic contact," *Solid-State Electronics*, vol. 36, no. 2, pp. 143–146, 1993.

[18] M. A. T. Lenio, A. J. Lennon, A. Ho-Baillie, and S. R. Wenham, "Effect of electroless nickel on the series resistance of high-efficiency inkjet printed passivated emitter rear contacted solar cells," *Solar Energy Materials and Solar Cells*, vol. 94, no. 12, pp. 2102–2107, 2010.

[19] E. J. Lee, D. S. Kim, and S. H. Lee, "Ni/Cu metallization for low-cost high-efficiency PERC cells," *Solar Energy Materials and Solar Cells*, vol. 74, no. 1–4, pp. 65–70, 2002.

[20] S. Sze and K. K. Ng, *Physics of Semiconductor Devices*, John Wiley & Sons, New Jersey, NJ, USA, 3rd edition, 2007.

[21] K. K. Ng and R. Liu, "On the calculation of specific contact resistivity on <100> silicon," *IEEE Transactions on Electron Devices*, vol. 37, pp. 1535–1537, 1990.

[22] P. Wurfel, *Physics of Solar Cells*, vol. 1, Wiley-VCH, Weinheim, Germany, 2005.

[23] A. Milne, *The passivated emitter and rear solar cell [Ph.D. thesis]*, Department of Electrical Engineering, University of New South Wales, Sydney, Australia, 1991.

[24] G. A. DiBari, "Nickel plating," *Metal Finishing*, vol. 93, no. 1, pp. 259–279, 1995.

[25] Technic Inc., "SEMCON semiconductor plating tools," http://www.technic.com/.

Research Article

Study of Ruthenium Complex Sensitizer and Gold Nanoparticles Doped Flexible Organic Solar Cells

Cheng-Chiang Chen and Lung-Chien Chen

Department of Electro-Optical Engineering, National Taipei University of Technology, No. 1, Section 3, Chung-Hsiao East Road, Taipei 106, Taiwan

Correspondence should be addressed to Lung-Chien Chen, ocean@ntut.edu.tw

This work presents a flexible organic solar cell with a structure for ITO/PEDOT:PSS/P3HT:PCBM + ruthenium complex sensitizer and Au nanoparticles on a flexible substrate. The process and thickness of the PEDOT:PSS hole transport layer and P3HT:PCBM active layer were optimized. A ruthenium complex sensitizer and Au nanoparticles were then introduced into the P3HT:PCBM active layer to improve the performance of solar cells. For the ITO/PEDOT:PSS/P3HT:PCBM + ruthenium complex sensitizer and Au nanoparticles structure on a flexible polyimide (PI) substrate under 0.1 and 1 sun conditions, the measured short-circuit current density (J_{sc}), open-circuit voltage (V_{oc}), fill factor (FF), and efficiency (η) are 3.89 and 9.67 mA/cm^2, 0.45 and 0.45 V, 0.266 and 0.232, and 4.65 and 1.01%, respectively.

1. Introduction

Flexible organic solar cells (FOSCs) have received considerable attention recently owing to their ability to be fabricated at low temperatures, economic cost, large area production, high flexibility, roll-to-roll manufacturing, and easy fabrication, such as by spin coating, [1–5] printing, [6–9] slot-die coating, [9–12] or evaporation [13, 14]. The organic active layer in FOSCs typically consists of a p-conjugated polymer donor and acceptor. The power conversion efficiency of (PCE) of FOSCs has been improved to 2.5%~3.7% using a bulk heterojunction (BHJ) structure comprising a blended film of poly(3-hexylthiophene) (P3HT) as the donor and [6,6]-phenyl-C$_{61}$-butyric acid methyl ester (PCBM) as the acceptor. Their PCE is significantly lower much than that of organic-based PTB7/PC$_{71}$BM structure solar cells on a glass substrate, that is, 7.4% [1, 11, 15–18]. However, polyimide (PI) substrates have become conventionally used in flexible electronic devices owing to their high transition temperatures, low surface roughness, low coefficients of thermal expansion, and high chemical resistance under typical fabrication conditions [1, 19, 20].

Owing to the inherent symmetry of the BHJ active layer, the nature of the electrodes largely determines the anode and cathode of the device [21]. Therefore, this work attempts to improve the PCE of solar cells by introducing a *cis*-bis(thiocyanato) bis(2,2′-bipyridyl-4,4′-dicarboxylate) ruthenium bis(tetrabutylammonium) (N719) sensitizer (Everlight Chemical Industrial Co., Taiwan) and Au nanoparticles (GNPs) (100 ppm, particle size: 2–5 nm, SD Technology Co., Taiwan) into the active layer of the FOSCs. The N719 and GNPs can achieve electron/hole collection efficiently. The characteristics of the ITO/PEDOT:PSS/P3HT:PCBM+N719+GNPs structure are also studied.

2. Experiment Details

Figure 1(a) shows the structure of flexible solar cells using P3HT as the electron donor and PCBM as the electron acceptor fabricated on semitransparent ITO-coated polyethylene terephthalate (PET) substrate (sheet resistance = 15 Ω/□ and thickness = 178 μm) (CPFilms Inc., Taiwan) and PI substrate (sheet resistance = 15 Ω/□ and thickness = 130 μm) (CPFilms Inc., Taiwan), respectively. The transmittance of both PET

(a)

(b)

P3HT:PCBM(1:0.8)
P3HT:PCBM(1:0.8) + N719

(c)

(d)
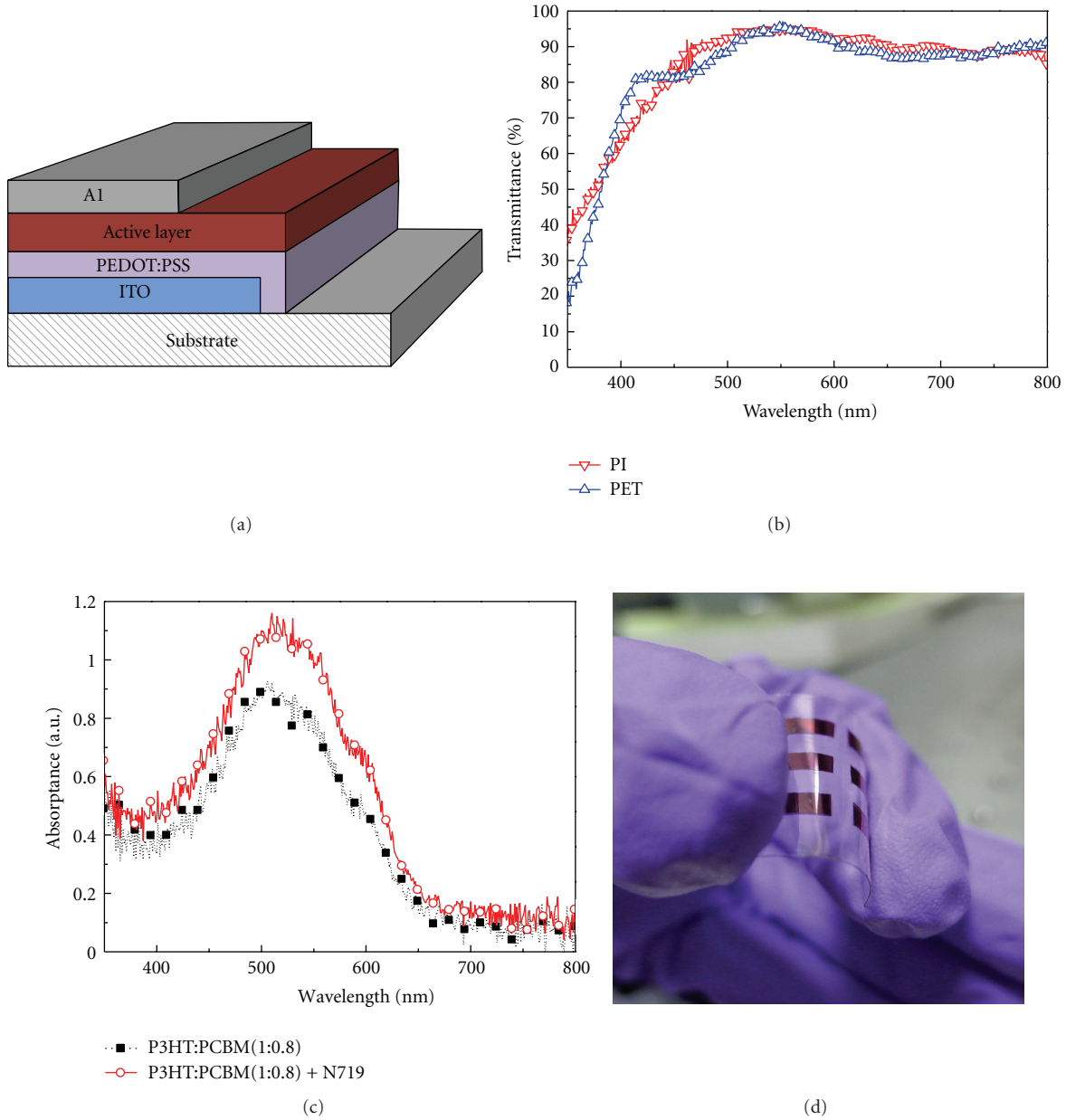
FIGURE 1: (a) Structure of a flexible organic solar cell. (b) Transmittance of PET and PI substrates with ITO layer. (c) Absorbance of P3HT:PCBM and P3HT:PCBM+N719. (d) Optical image of a flexible organic solar cell.

and PI substrates with ITO layer was about 95% at 550 nm, as shown in **Figure 1(b)**. Therefore, PET and PI substrates are suitable for FOSCs. PEDOT:PSS hole transport layer was spun on the substrate with ITO layer and annealed at various temperatures for 10 min in a vacuum. An attempt was made to achieve the required viscosity in the range of 2 to 30 cps and reduce the tension of the PEDOT:PSS layer by adding a surfactant Triton X-100 to the PEDOT:PSS solution [22]. Next, the PEDOT:PSS solution was filtered through 0.45 μm PP syringe filters before spin coating on the substrate. Additionally, P3HT and PCBM were blended with 1,2-dichlorobenzene(DCB) (1 : 0.8 at wt%) as an active layer. The solution was then filtered through 0.45 μm PP

syringe filters before spin coating. P3HT:PCBM blended solution was spin coated on a dried PEDOT:PSS thin film and annealed at 140°C for 10 min in a vacuum. Finally, Al layer was deposited under a base pressure of 1×10^{-6} Torr. Al cathode was deposited through a shadow mask to a thickness of 70 nm, given an active area of 2 mm × 5 mm. Therefore, the cell has an active area of 2 mm × 5 mm. Distance from the crucible to the substrate was fixed at 20 cm, and a substrate holder was rotated continuously to ensure uniform films. Next, film thickness and deposition rate, which was adjusted by SEM, were monitored using quartz crystal microbalance (QCM). **Figure 1(c)** shows the absorbance of P3HT:PCBM and P3HT:PCBM+N719. Therefore, in this study, the N719

FIGURE 2: The J-V characteristics of the solar cells with PEDOT:PSS hole transport layer in (a) various thicknesses and (b) various annealing temperatures.

ruthenium complex sensitizer is employed to improve the absorption of light and the performance of cell. Figure 1(d) shows the flexibility of the as-prepared cell.

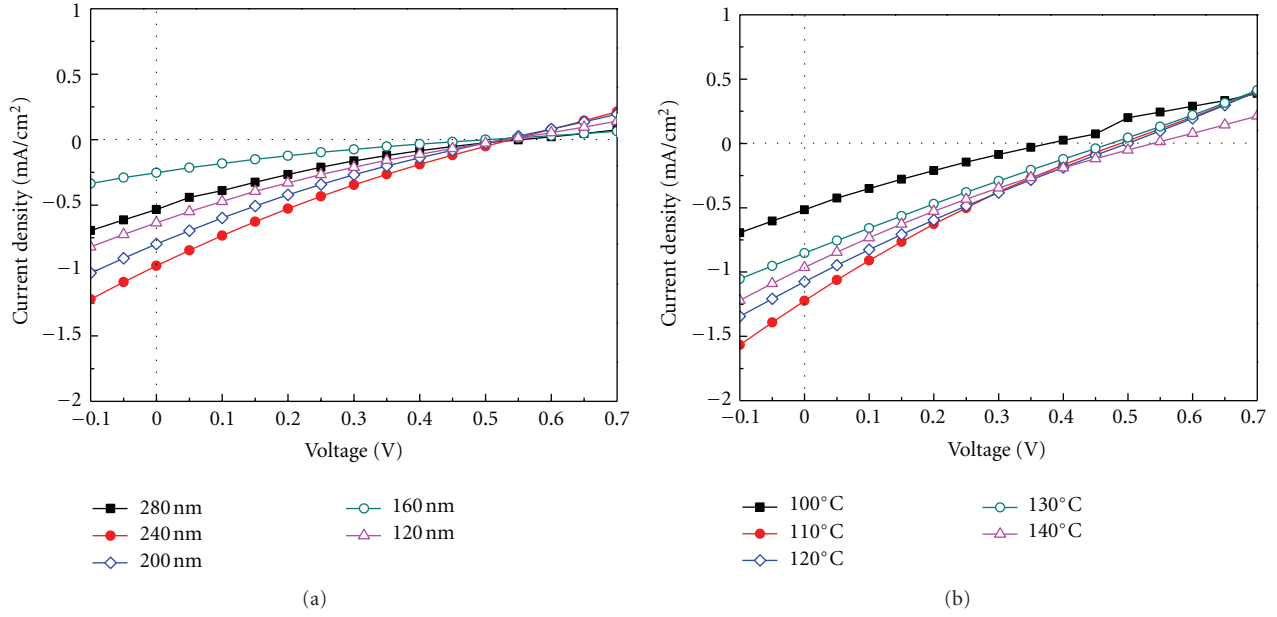The current density-voltage (J-V) characteristics were then measured using a Keithley 2420 programmable sourcemeter under irradiation by a solar simulator with a 250 W xenon lamp. Finally, the irradiation power density in the surface of the sample was calibrated as 100 and 1000 W/m^2 incident power densities.

3. Results and Discussion

This work attempted first to optimize the hole transport layer PEDOT:PSS based on the structure of Figure 1(a) by using a 100 nm-thick P3HT:PCBM active layer annealed at 140°C. Figures 2(a) and 2(b) plot the J-V characteristics of the ITO/PEDOT:PSS/P3HT:PCBM/Al solar cells with various hole transport layer thicknesses and annealing temperatures under illumination, respectively. According to Figure 2(a), increasing the thickness of the PEDOT:PSS layer decreased both the transparency and sheet resistance, subsequently affecting the photocurrent and fill factor of the solar cells. However, decreasing the transparency of the PEDOT:PSS layer reduced the available photons to be absorbed by the active layer ultimately leading to a lower photocurrent density. However, this lowering of the photocurrent was offset by an increase in the fill factor due to the low sheet resistance [23]. The photocurrent of cells increased with an increasing annealing temperature, as shown in Figure 2(b). The photocurrent density increases from 0.516 mA/cm^2 (100°C annealing) to 1.24 mA/cm^2 (110°C annealing) and then decreases to 1.08 mA/cm^2 (120°C annealing), which subsequently increases to 0.97 mA/cm^2 (140°C annealing),

as shown in Figure 2(b). The photocurrent of cells increased with an increasing annealing temperature as the annealing temperature increases from 100 to 110°C. This indicates a variation in the conduction mechanism from the nearest neighbor hopping at the beginning of the heat treatment to the charging-energy limited tunneling between the conductive grains due to the shrinking of the PEDOT conductive grains [24]. The photocurrent of cells decreased with an increasing annealing temperature as the annealing temperature increases from 110 to 130°C. This may attributed to the oxidation or degradation of the PEDOT. Then, the photocurrent of cells increased with an increasing annealing temperature as the annealing temperature increases from 130 to 140°C owing to the PSS segregation effects [25]. The optimum thickness and annealing temperature of the PEDOT:PSS layer is 240 nm and 110°C, respectively.

Figure 3 plots the J-V characteristics of the ITO/PEDOT:PSS/P3HT:PCBM/Al solar cells with the optimized hole transport layer and various thicknesses of the active layer under illumination. Table 1 lists the characteristic parameters of solar cells on various substrates. The parameters of a solar cell with P3HT:PCBM active layer on the PI substrate exhibited J_{sc} = 3.18 mA/cm^2, V_{oc} = 0.4 V, FF = 0.257, and a PCE of 3.27%, respectively. According to this table, the photocurrent of cells increases since the number of photogenerated electron-hole pairs increases with an increasing thickness of the active layer. However, the photocurrent decreases as the thickness of the active layer is higher than 200 nm. The thickness of the active layer increases, subsequently degrading the J-V characteristics and the fill factor. The solar cell can be modeled as an equivalent circuit consisting of a current generator of J_{sc} and two resistances, series resistance (R_s) and shunt resistance (R_{sh}). If the R_{sh} is sufficiently large to be neglected, the effect of the

TABLE 1: The parameters of solar cells with P3HT:PCBM active layer.

Substrate	V_{oc} (V)	J_{sc} (mA/cm^2)	FF	η (%)
Glass	0.45	3.61	0.253	4.1
PI	0.4	3.18	0.257	3.27
PET	0.4	2.14	0.261	2.24
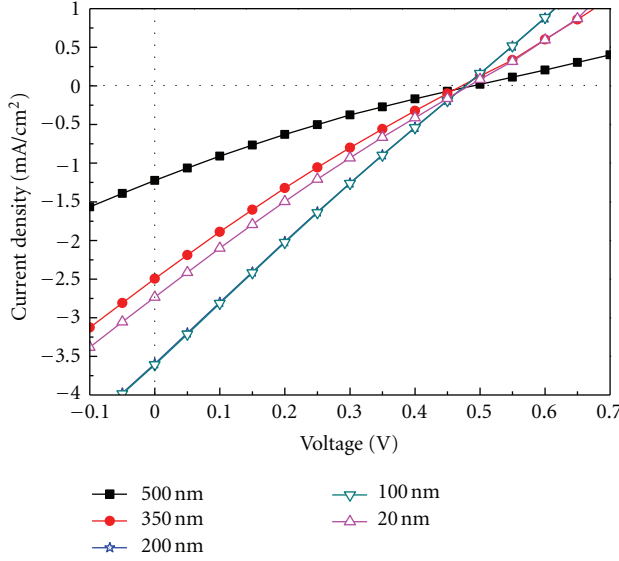
(a)
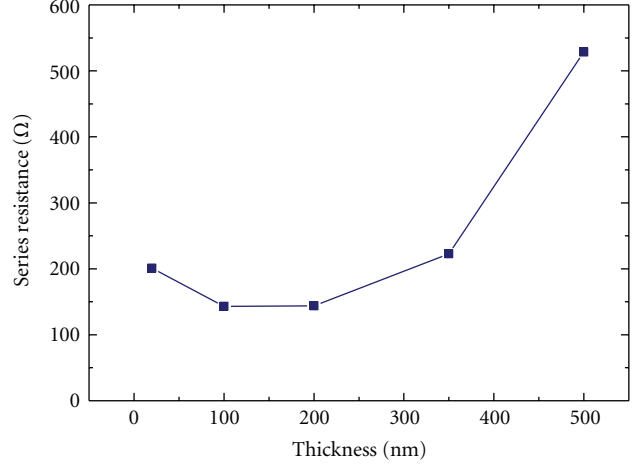
(b)

FIGURE 3: (a) The J-V characteristics of the solar cells with various thicknesses of P3HT:PCBM active layer on the PI substrates. (b) The series resistance of cells with various thickness active layers.

R_s on the I-V characteristics can be taken into account as shown below [26, 27]:

$$I = I_s \left[\exp\left(\frac{q(V - IR_s)}{nkT} \right) - 1 \right] - I_{ph}, \quad (1)$$

where I_{ph} is the photocurrent, I_s is the saturation current, and n, k, and T are the ideality factor, Boltzmann constant, and temperature, respectively. Simple mathematical manipulation of (1) obtains [27]

$$\frac{dV}{dI} = R_s + \frac{nkT}{q} \left(I + I_{ph} \right)^{-1}. \quad (2)$$

As shown in Figure 3(b), the cell with 100 nm-thick active layer have a smaller series resistance ($\sim$140 Ω), and the cell with 500 nm-thick active layer have a larger series resistance ($\sim$528 Ω). A thicker P3HT:PCBM active layer implies a higher series resistance and poorer transparency, subsequently increasing of R_s and lowering of photocurrent, and degrading its performance [23, 28]. Therefore, the effective absorption of P3HT:PCBM active layer can be optimized by varying the active layer thickness.

Previous studies have applied a traditional ruthenium complex sensitizer *cis*-bis(thiocyanato) bis(2,2′-bipyridyl-4,4′-dicarboxylate) ruthenium bis(tetrabutylammonium) (N719) in dye-sensitized solar cells to extend the optical threshold wavelength since the N719 sensitizer should absorb

photons from the visible to near-infrared (NIR) region of the solar spectrum while maintaining sufficient thermodynamic driving force for the electron injection and dye regeneration process [29–32]. This work also attempted to increase the efficiency of flexible solar cells by introducing N719 into the P3HT:PCBM active layer. Figure 4 plots the J-V characteristics of the ITO/PEDOT:PSS/P3HT:PCBM+N719/Al (N719 = 0.3 mg) solar cells under illumination. Table 2 lists the characteristic parameters of solar cells with various structures. The parameters of solar cell with P3HT:PCBM+N719 active layer on the PI substrate exhibited J_{sc} = 3.89 mA/cm^2, V_{oc} = 0.4 V, FF = 0.258, and a PCE of 3.68%, respectively. Notably, the PCE was improved by approximately 12.5% over that of the control sample. This improvement in PCE can be attributed to that the absorption of P3HT:PCBM active with N719 sensitizer have better than that of P3HT:PCBM active layer in visible, especially in the wavelength of 500–600 nm, as shown in Figure 1(c).

Figure 5 plots the J-V characteristics of the ITO/PEDOT:PSS/P3HT:PCBM+N719+GNPs/Al (P3HT:PCBM = 1 : 0.8 (20 mL : 16 mL), N719 = 0.3 mg, GNPs = 0.3 mL) solar cells under illumination. Table 3 lists the characteristic parameters of solar cells with various substrates under 0.1 sun and 1 sun (AM 1.5) conditions, respectively. The parameters of solar cell with P3HT:PCBM+N719+GNP active layer on the PI substrate exhibited J_{sc} = 3.89 mA/cm^2, V_{oc} = 0.45 V, FF = 0.266, and a PCE of 4.65% under 0.1 sun
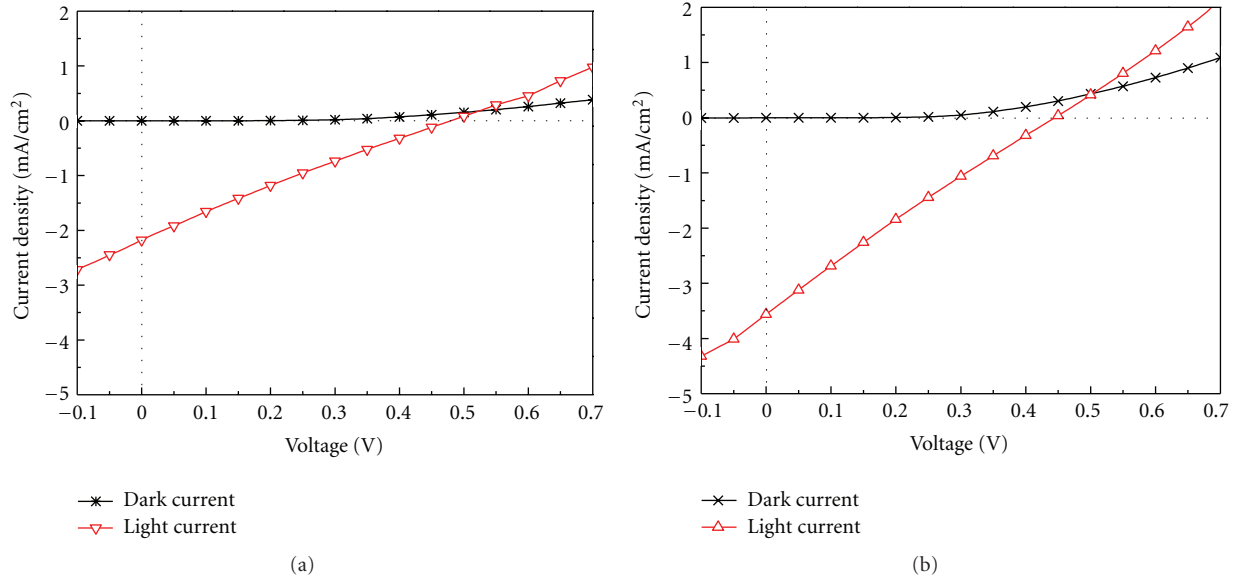
(a)

(b)

FIGURE 4: The J-V characteristics of the solar cells with P3HT:PCBM+N719 active layer on (a) the PET substrate and (b) the PI substrate.

TABLE 2: The parameters of solar cells with P3HT:PCBM+N719 active layer.

Substrate	V_{oc} (V)	J_{sc} (mA/cm^2)	FF	η (%)
Glass	0.45	3.96	0.245	4.36
PI	0.4	3.56	0.258	3.68
PET	0.45	2.18	0.243	2.38

TABLE 3: The parameters of solar cells with P3HT:PCBM+N719+GNP active layer.

Condition	Substrate	V_{oc} (V)	J_{sc} (mA/cm^2)	FF	η (%)
	Glass	0.45	4.06	0.261	4.76
0.1 sun	PI	0.45	3.89	0.266	4.65
	PET	0.45	2.87	0.248	3.21
	Glass	0.50	13.48	0.211	1.42
1 sun	PI	0.45	9.67	0.232	1.01
	PET	0.45	9.31	0.232	0.97

condition, respectively. The PCE was improved by approximately 42.2% over that of the control sample (without N719 and GNPs). Introducing N719 and GNPs may account for this improvement. When photo-generated electrons are injected into GNPs and the Fermi level (E_F) is raised as close to the lowest unoccupied molecular orbital (LUMO) of P3HT as possible, a quick shuttling of electrons occurs from Au to P3HT. Therefore, GNPs promote the generation of charge carriers and increase both the photocurrent and the efficiency of conversion of solar energy in solar cells [33, 34]. Meanwhile, the incorporation of N719 can assist transportation of the photo-generated electrons and holes. The energy level diagram and mechanism of photocurrent generation in the solar cells with P3HT:PCBM+N719+GNPs active layer is summarized in Figure 6. Finally, the efficiency improvement of solar cells with various active layers under condition of 0.1 sun are listed in Table 4 for easy reading and understanding.

4. Conclusions

This work demonstrated the feasibility of fabricating a flexible organic solar cell with a ITO/PEDOT:PSS/P3HT:PCBM + ruthenium complex sensitizer and Au nanoparticles structure on a flexible substrate. The process and thickness of PEDOT:PSS hole transport layer and P3HT:PCBM active layer were optimized. For the ITO/PEDOT:PSS/P3HT:PCBM + ruthenium complex sensitizer and Au nanoparticles structure on a flexible polyimide (PI) substrate under 0.1 and 1 sun conditions, the measured short-circuit current density (J_{sc}), open-circuit voltage (V_{oc}), fill factor (FF), and efficiency (η) are 3.89 and 9.67 mA/cm^2, 0.45 and

TABLE 4: The efficiency improvement of solar cells with various active layers under condition of 0.1 sun.

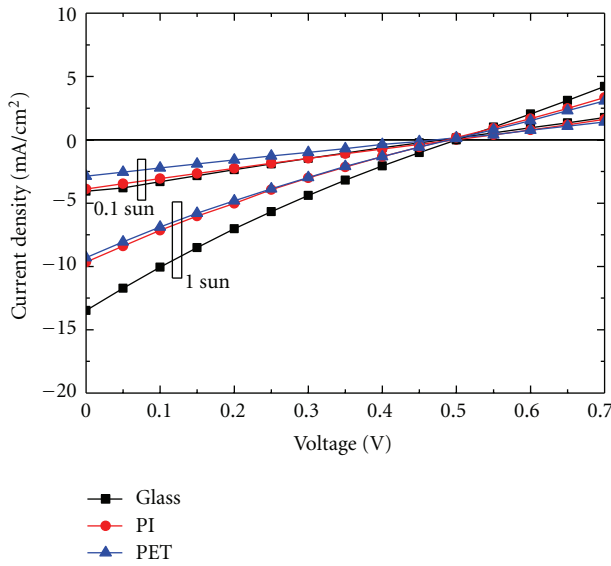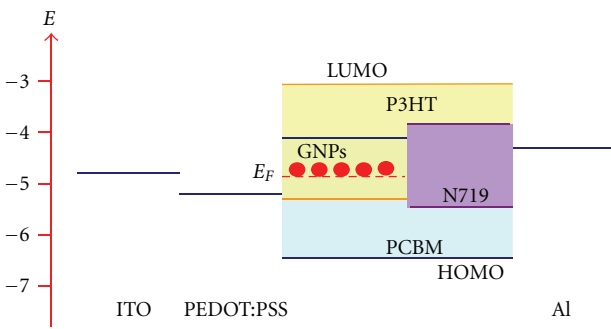| Substrate	P3HT:PCBM	P3HT:PCBM+N719		P3HT:PCBM+N719+GNP	
	η (%)	η (%)	Improvement (%)	η (%)	Improvement (%)
Glass	4.1	4.36	6.34	4.76	16.1
PI	3.27	3.68	12.54	4.65	42.2
PET	2.24	2.38	6.25	3.21	43.3

FIGURE 5: The J-V characteristics of the solar cells with P3HT:PCBM+N719+GNPs active layer on various substrates.

FIGURE 6: Energy level diagram and mechanism of photocurrent generation in the solar cells with P3HT:PCBM+N719+GNPs active layer.

0.45 V, 0.266 and 0.232, and 4.65 and 1.01%, respectively. Comprising the reported articles, the improved PCE of P3HT:PCBM-based FOSCs may be attributed to introduction of a ruthenium complex sensitizer and Au nanoparticles into the P3HT:PCBM active layer, subsequently increasing the photogenerated carrier injection.

Acknowledgment

References

[1] Y. S. Hsiao, C. P. Chen, C. H. Chao, and W. T. Whang, "All-solution-processed inverted polymer solar cells on granular surface-nickelized polyimide," *Organic Electronics*, vol. 10, no. 4, pp. 551–561, 2009.

[2] I. Sasajima, S. Uesaka, T. Kuwabara, T. Yamaguchi, and K. Takahashi, "Flexible inverted polymer solar cells containing an amorphous titanium oxide electron collection electrode," *Organic Electronics*, vol. 12, no. 1, pp. 113–118, 2011.

[3] F. Wang, Z. Chen, L. Xiao, B. Qu, and Q. Gong, "Papery solar cells based on dielectric/metal hybrid transparent cathode," *Solar Energy Materials and Solar Cells*, vol. 94, no. 7, pp. 1270–1274, 2010.

[4] A. Bedeloglu, A. Demir, Y. Bozkurt, and N. S. Sariciftci, "A flexible textile structure based on polymeric photovoltaics using transparent cathode," *Synthetic Metals*, vol. 159, no. 19-20, pp. 2043–2048, 2009.

[5] Y. T. Cheng, J. J. Ho, C. K. Wang et al., "Improvement of organic solar cells by flexible substrate and ITO surface treatments," *Applied Surface Science*, vol. 256, no. 24, pp. 7606–7611, 2010.

[6] P. Kopola, T. Aernouts, R. Sliz et al., "Gravure printed flexible organic photovoltaic modules," *Solar Energy Materials and Solar Cells*, vol. 95, no. 5, pp. 1344–1347, 2011.

[7] M. M. Voigt, R. C. I. MacKenzie, C. P. Yau et al., "Gravure printing for three subsequent solar cell layers of inverted structures on flexible substrates," *Solar Energy Materials and Solar Cells*, vol. 95, no. 2, pp. 731–734, 2011.

[8] M. Manceau, D. Angmo, M. Jørgensen, and F. C. Krebs, "ITO-free flexible polymer solar cells: from small model devices to roll-to-roll processed large modules," *Organic Electronics*, vol. 12, no. 4, pp. 566–574, 2011.

[9] F. C. Krebs, "Polymer solar cell modules prepared using roll-to-roll methods: knife-over-edge coating, slot-die coating and screen printing," *Solar Energy Materials and Solar Cells*, vol. 93, no. 4, pp. 465–475, 2009.

[10] N. Espinosa, R. García-Valverde, A. Urbina, and F. C. Krebs, "A life cycle analysis of polymer solar cell modules prepared using roll-to-roll methods under ambient conditions," *Solar Energy Materials and Solar Cells*, vol. 95, no. 5, pp. 1293–1302, 2011.

[11] B. Zimmermann, H. F. Schleiermacher, M. Niggemann, and U. Würfel, "ITO-free flexible inverted organic solar cell modules with high fill factor prepared by slot die coating," *Solar Energy Materials and Solar Cells*, vol. 95, no. 7, pp. 1587–1589, 2011.

[12] F. C. Krebs, "All solution roll-to-roll processed polymer solar cells free from indium-tin-oxide and vacuum coating steps," *Organic Electronics*, vol. 10, no. 5, pp. 761–768, 2009.

[13] T. T. T. Luong, Z. Chen, and H. Zhu, "Flexible solar cells based on copper phthalocyanine and buckminsterfullerene," *Solar Energy Materials and Solar Cells*, vol. 94, no. 6, pp. 1059–1063, 2010.

[14] C. J. Brabec, N. S. Sariciftci, and J. C. Hummelen, "Plastic solar cells," *Advanced Functional Materials*, vol. 11, no. 1, pp. 15–26, 2001.

[15] M. Al-Ibrahim, H. K. Roth, U. Zhokhavets, G. Gobsch, and S. Sensfuss, "Flexible large area polymer solar cells based on poly(3-hexylthiophene)/ fullerene," *Solar Energy Materials and Solar Cells*, vol. 85, no. 1, pp. 13–20, 2005.

[16] J. P. Liu, K. L. Choy, and X. H. Hou, "Charge transport in flexible solar cells based on conjugated polymer and ZnO nanoparticulate thin films," *Journal of Materials Chemistry*, vol. 21, no. 6, pp. 1966–1969, 2011.

[17] N. Sun, G. Fang, P. Qin et al., "Efficient flexible organic solar cells with room temperature sputtered and highly conductive NiO as hole-transporting layer," *Journal of Physics D*, vol. 43, no. 44, Article ID 445101, 2010.

[18] Y. Liang, Z. Xu, J. Xia et al., "For the bright future—bulk heterojunction polymer solar cells with power conversion efficiency of 7.4%," *Advanced Materials*, vol. 22, no. 20, pp. E135–E138, 2010.

[19] K. Akamatsu, S. Ikeda, and H. Nawafune, "Site-selective direct silver metallization on surface-modified polyimide layers," *Langmuir*, vol. 19, no. 24, pp. 10366–10371, 2003.

[20] H. K. Kim, J. A. Jeong, K. H. Choi, S. W. Jeong, and J. W. Kang, "Characteristics of flexible ito electrodes grown by continuous facing target roll-to-roll sputtering for flexible organic solar cells," *Electrochemical and Solid-State Letters*, vol. 12, no. 5, pp. H169–H172, 2009.

[21] G. Yu, J. Gao, J. C. Hummelen, F. Wudl, and A. J. Heeger, "Polymer photovoltaic cells: enhanced efficiencies via a network of internal donor-acceptor heterojunctions," *Science*, vol. 270, no. 5243, pp. 1789–1791, 1995.

[22] M. A. López, J. C. Sánchez, and M. Estrada, "Characterization of PEDOT:PSS dilutions for inkjet printing applied to OLED fabrication," in *Proceedings of the 7th International Caribbean Conference on Devices, Circuits and Systems (ICCDCS'08)*, pp. 1–4, Cancun, Mexico, April 2008.

[23] S. K. Hau, H. L. Yip, J. Zou, and A. K. Y. Jen, "Indium tin oxide-free semi-transparent inverted polymer solar cells using conducting polymer as both bottom and top electrodes," *Organic Electronics*, vol. 10, no. 7, pp. 1401–1407, 2009.

[24] E. Vitoratos, S. Sakkopoulos, E. Dalas et al., "Thermal degradation mechanisms of PEDOT:PSS," *Organic Electronics*, vol. 10, no. 1, pp. 61–66, 2009.

[25] B. Friedel, P. E. Keivanidis, T. J. K. Brenner et al., "Effects of layer thickness and annealing of PEDOT:PSS layers in organic photodetectors," *Macromolecules*, vol. 42, no. 17, pp. 6741–6747, 2009.

[26] S. M. Sze, *Physics of Semiconductor Devices*, John Wiley & Sons, New York, NY, USA, 2nd edition, 1981.

[27] K. Nishioka, T. Takamoto, T. Agui, M. Kaneiwa, Y. Uraoka, and T. Fuyuki, "Evaluation of InGaP/InGaAs/Ge triple-junction solar cell and optimization of solar cell's structure focusing on series resistance for high-efficiency concentrator photovoltaic systems," *Solar Energy Materials and Solar Cells*, vol. 90, no. 9, pp. 1308–1321, 2006.

[28] W. H. Lee, S. Y. Chuang, H. L. Chen, W. F. Su, and C. H. Lin, "Exploiting optical properties of P3HT:PCBM films for

[29] T. Horiuchi, H. Miura, K. Sumioka, and S. Uchida, "High efficiency of dye-sensitized solar cells based on metal-free indoline dyes," *Journal of the American Chemical Society*, vol. 126, no. 39, pp. 12218–12219, 2004.

[30] S. Q. Fan, C. Kim, B. Fang et al., "Improved efficiency of over 10% in dye-sensitized solar cells with a ruthenium complex and an organic dye heterogeneously positioning on a single TiO$_2$ electrode," *Journal of Physical Chemistry C*, vol. 115, no. 15, pp. 7747–7754, 2011.

[31] M. K. Nazeeruddin, R. Humphry-Baker, P. Liska, and M. Grätzel, "Investigation of sensitizer adsorption and the influence of protons on current and voltage of a dye-sensitized nanocrystalline TiO$_2$ solar cell," *Journal of Physical Chemistry B*, vol. 107, no. 34, pp. 8981–8987, 2003.

[32] S. W. Tong, C. F. Zhang, C. Y. Jiang et al., "Improvement in the hole collection of polymer solar cells by utilizing gold nanoparticle buffer layer," *Chemical Physics Letters*, vol. 453, no. 1–3, pp. 73–76, 2008.

[33] C. Hägglund, M. Zäch, and B. Kasemo, "Enhanced charge carrier generation in dye sensitized solar cells by nanoparticle plasmons," *Applied Physics Letters*, vol. 92, no. 1, Article ID 013113, 3 pages, 2008.

[34] S. Barazzouk and S. Hotchandani, "Enhanced charge separation in chlorophyll a solar cell by gold nanoparticles," *Journal of Applied Physics*, vol. 96, no. 12, pp. 7744–7746, 2004.

organic solar cells with semitransparent anode," *Thin Solid Films*, vol. 518, no. 24, pp. 7450–7454, 2010.

Research Article

Effects of Organic Compounds on Microstructure, Optical, and Electrical Properties of ITO Thin Films Prepared by Dip-Coating Method

Ru-Yuan Yang,[1] Cheng-Jye Chu,[2] Yu-Ming Peng,[1] and Hui-Ju Chueng[2]

[1] *Department of Material Engineering, National Pingtung University of Science and Technology, Pingtung County 912, Taiwan*
[2] *Nanmat Technology CO., Ltd., Kaohsiung 811, Taiwan*

Correspondence should be addressed to Ru-Yuan Yang, ryyang@mail.npust.edu.tw

Tin-doped Indium oxide (ITO) thin films were prepared by sol-gel dip-coating technique using low-cost metal salts and organic solvents. The coated films were treated without annealing or annealed at 400°C and 600°C in 3% H_2/97% N_2 mixtures atmosphere. Microstructure, optical, and electrical properties of the prepared ITO films were investigated in detail. The maximum transmittance in the visible range (380–780 nm) is 85.6%, and the best resistivity is 5×10^{-2} Ω-cm when annealed at 600°C in 3% H_2/97% N_2 mixtures atmosphere. It is found that the optical and electrical properties of the prepared ITO films are strongly related to the microstructure variation. The organic compounds could not be removed completely, and the prepared ITO thin films were not dense when the prepared ITO film was annealed at 600°C in 3% H_2/97% N_2 mixtures atmosphere, causing the poor conductivity.

1. Introduction

Tin-doped Indium oxide (ITO) thin films have been widely applied in touch panel contacts, electrodes for LCD and electrochromic displays, gas sensors, heat-reflecting coatings to increase light bulb efficiency, antistatic window coatings, energy conserving architectural windows and so on [1–4]. A variety of fabricating methods have been employed to prepare the ITO thin films, such as sputtering [5], chemical vapor deposition [6], and sol-gel process [7]. Among the variously available kinds of techniques, the sol-gel technique seemed to attract much attention for its advantages such as simplicity, low cost, doping levels easily controlled and feasible preparation for large area films and without using expensive and complex equipments. Moreover, process conditions affect the densification and crystallization of the ITO films prepared by the sol-gel technique. However, the ITO films prepared by sol-gel technique exhibit a relatively low conductivity resulting from considerable porosity even after films with postannealed at a high temperature and the difficulty to obtain metal alkoxides as raw materials for their unavailability and high price [8–10].

In this paper, the ITO thin films were prepared by sol-gel dip-coating technique using low-cost metal salts and organic solvents. The effects of postannealing temperature in 3% H_2/97% N_2 mixtures atmosphere on morphology, structure, and electrical properties of the ITO thin films are investigated to verify the relationship between the process condition and the properties of the prepared films. It is found that the optical and electrical properties of the prepared ITO films are strongly related to the microstructure variation, especially resulted from the organic compounds of the precursors.

2. Experimental

Figure 1 shows a diagram of the synthesis and deposition process of the prepared ITO films coating on glass substrate in detail. First, anhydrous indium chloride ($InCl_3$) was dissolved in isopropyl alcohol in the mix after adding
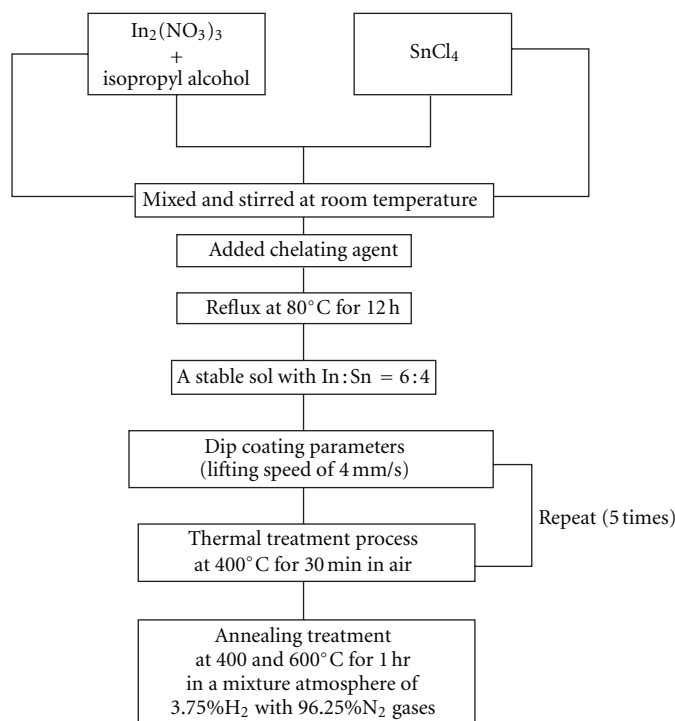
FIGURE 1: A diagram of the synthesis and deposition process of the prepared ITO films coating on glass substrate.

anhydrous tin chemical compound ($SnCl_4$) and stirred at room temperature. Secondary, chelating agent added to the solution and maintained in reflux at 80°C for 12 h. Finally, a stable sol with the molar ratio of the In : Sn = 6 : 4 was obtained. Additionally, the cleaned glass plates (20 mm × 20 mm × 3 mm) were used as the substrates for coating. The sol containing In and Sn sources was prepared on the glass substrate by dip-coating method at a withdrew speed of 4 mm/sec. Then, the film was fired at 400°C for 30 min in air and then cooled down to room temperature. A completely deposition involved 5 orders of the dipping and firing process to form the as-prepared ITO thin films. The total thickness of the as-prepared ITO films was controlled in the range of 250 to 300 nm. Finally, the as-prepared ITO films were annealed in 3% H_2/97% N_2 mixtures atmosphere in a tube furnace at 400 and 600°C for 1 hr.

Thermogravimetric-differential thermal analysis (TG-DTA 2000, MAC Science Co., Ltd., Japan) was used to obtain the weight loss and reaction behavior of the gel and performed under the atmospheric air condition with a heating rate of 5°C/min. X-ray diffraction system (XRD, BRUKER D8 ADVANCE) equipped with CuK_α radiation of average wavelength 1.5406 Å was used to specify the existent phases and the orientation of the ITO thin films. X-ray patterns were taken 2θ between 20° and 80° and scan speed of 4.5°/min. Fourier Transform Infrared Spectroscopy (FTIR, Spectrum 100) and Energy Dispersive Spectrometer (EDS, JSM-6400F. JEOL, Japan) were used to detect the residue of the organic compounds in the ITO thin films, wherein the FTIR spectra were recorded at the range of 4000 cm^{-1} to 400 cm^{-1} [11]. Field emission-scanning

electron microscopy (FE-SEM, JSM-6400F. JEOL, Japan) and Atomic force microscopy (AFM, Veeco CP series) were used to observe the surface microstructure morphologies of the ITO thin films. Moreover, the standard four-point probe method was used to measure the room-temperature conductivity of the ITO thin films.

3. Results and Discussion

Figure 2 shows the TG-DTA curves of the ITO gel. The weight mass of ITO gel displays continuous and significant decrease with the rising of heat treatment temperature before 361°C. There are four endothermic peaks at 65, 94, 213, and 279°C, respectively, and one distinct exothermic peak at 361°C. The endothermic peaks are attributed to heat release from charring and decomposition of organic groups and components, and the exothermic peak is proposed resulting from the transformation of In_2O_3 to polycrystalline cubic bixbyite structure. In addition, the mass of ITO gel does not change at the temperature higher than 350°C. Therefore, the temperature above 400°C was selected as firing temperature to prepare the desired ITO thin films in this work.

Figure 3 shows the XRD patterns of the ITO thin films treated without annealing, and with annealing at 400°C and 600°C in 3% H_2/97% N_2 mixtures atmosphere. The major diffraction peaks angle of the In_2O_3 crystal located at 21.493°, 30.579°, 35.455°, and 51.013° are corresponding to the reflection planes of (222), (400), (440), and (622), respectively, described in JCPDS database (Card No. 44-1087), which indicates that In_2O_3 phase is in a cubic system with the space group, T_h^7 Ia3, and lattice parameter,
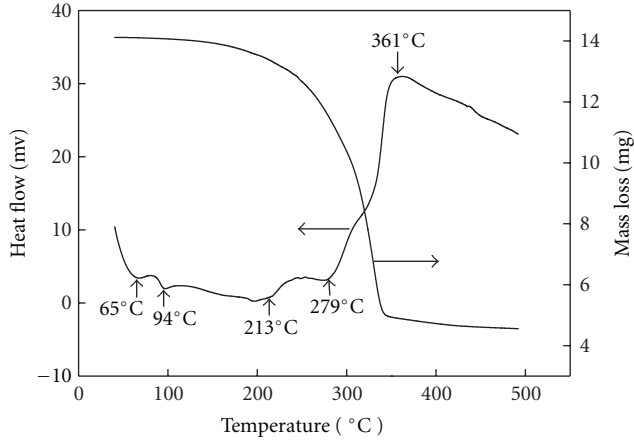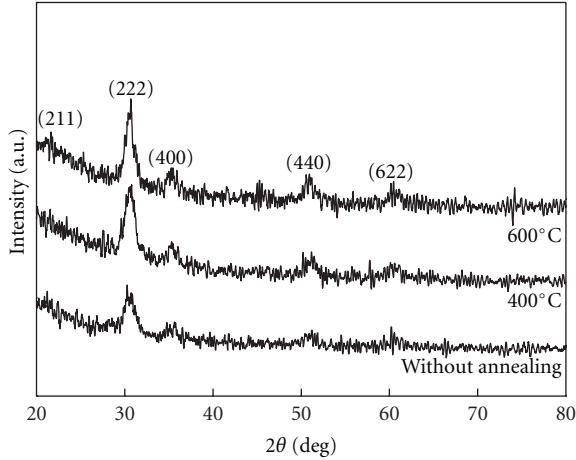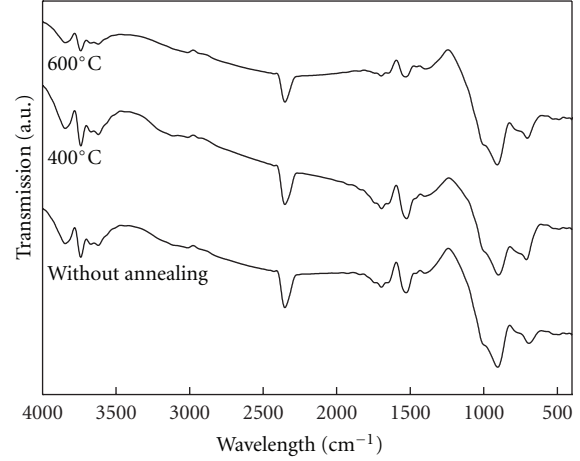
FIGURE 2: TG-DTA curves of the ITO gel.

FIGURE 3: XRD patterns of the ITO thin films treated without annealing and with annealing at 400°C and 600°C in 3% H$_2$/97% N$_2$ mixtures atmosphere.

a = 1.0117 nm at 26°C [12]. The spectrums show that the diffraction peaks of the ITO thin films treated without annealing are not obvious on the planes of the (400), (440), and (622) of the In$_2$O$_3$ crystal. When the ITO films treated with annealing temperature of 400°C, the ITO gel gradually began to lose the intermolecular water and revealed the characteristic diffraction peaks of the In$_2$O$_3$ crystal [9, 10]. All the diffraction peaks were weak even when the annealing temperature further was increased to 600°C. In addition, no second phases corresponded to the other Sn compounds were found indicating that the Sn element was dissolved in the In$_2$O$_3$ to form a good solid solution. In ITO material system, Tin ion is tetravalent and Indium ion is trivalent, each Sn^{4+} replacing In^{3+} substitutionally, thus, contributing a free carrier electron for the conductivity. Therefore, the ITO thin films retain the cubic In$_2$O$_3$ structure up to the solid solubility limit of the Sn in the In$_2$O$_3$ [13]. However, not all the Sn atoms can be substituted to In atom sites. Therefore, small amounts of Sn(IV) may be transformed to Sn(II) [14]. When the annealing temperature was increased,

FIGURE 4: FTIR spectra of the ITO thin films treated without annealing and with annealing at 400°C and 600°C in 3% H$_2$/97% N$_2$ mixtures atmosphere.

the width of the (222) diffraction peaks became more sharp due to the improved crystalline with increasing the postannealing temperature. The crystallinity of the ITO thin films can be improved by increasing the postannealing temperature [15]. Additionally, the crystallinity depends on the annealing temperatures rather than the atmosphere used in the postannealing process [5].

The average crystalline size (D) of the ITO thin films is determined by applying the Scherrer equation to the full width at half maximum (FWHM) of the (222) diffraction peaks, as given by [16]

$$D = \frac{0.9\lambda}{\omega \cos \theta}, \tag{1}$$

where ω is the calibrated FWHM of the selected diffraction line in radians, θ is the Bragg angle, and λ is the X-ray wavelength (0.15406 nm). In Table 1, the FWHM of (222) diffraction peaks were decreased with an increase in annealing temperature. Thus, the crystalline size was increased from about 3.3 to 4.5 nm for that treated without annealing to that treated with annealing temperature of 600°C, indicating the crystalline of the ITO films can be improved with increasing annealing temperature [15].

Figure 4 shows the FTIR spectra of the ITO thin films treated without annealing and with annealing at 400°C and 600°C in 3% H$_2$/97% N$_2$ mixtures atmosphere. The bands appearing at below 900 cm^{-1} are corresponded to the stretching vibrations of In–O and Sn–O, as well as to the contributions of In=O and Sn=O bonds [9]. Moreover, there are a stretching vibration peak of C–C band in the range 1652–1579 cm^{-1}, a stretching vibration peak of C=O band in the range 1727–1720 cm^{-1}, and a stretching vibration peak of C–H band in the range 2800–2200 cm^{-1} since the ITO thin films were treated without annealing. When the ITO thin films were treated without annealing and with annealing temperature at 400°C, the FTIR characteristics almost do not change. However, when the ITO thin films were treated with annealing at 600°C, the C–C band,

TABLE 1: Main characteristics of the prepared ITO thin films.

Annealing conditions	Carbon content[a] (weight%)	FWHM[b] (Degree)	Crystal size[b] (nm)	Conductivity[c] (S/cm)
Without annealing	8.15	2.5	3.3	0.3×10^1
Annealed at 400°C	4.90	2.3	3.9	0.8×10^1
Annealed at 600°C	0.00	1.9	4.5	2×10^1

[a] By EDS.
[b] By XRD.
[c] By 4-point probe.

C=O band and C–H band, became broader. This result is due to the decreased organic compounds as increasing the annealing temperature [10, 11]. Furthermore, under annealing treatment at a certain temperature, thin films are formed after withdrawing and drying to lose their intermolecular water and organic components gradually, and translated into crystalline state [11]. In Table 1, the residues of carbon from the organic compounds detected by EDS were decreased with increased annealing temperature. As annealing temperature was reached to 600°C, carbon contents disappeared completely. Compare to the result from FTIR analysis, the organic compounds did not be decreased completely even as annealing temperature was reached to 600°C. These results may be attributed to the detection limit of the EDS analyzer. Although the burned out temperature of the organic compounds is around 350°C which is obtained from the DTA/TG curve, the organic compounds were not decomposed completely as the ITO films were fired at 400°C. The reason may be the holding time on the firing temperature is not enough to volatilize the organic compounds absolutely.

Figure 5 shows the SEM images of the ITO thin films treated without annealing, and with annealing at 400°C and 600°C in 3% H_2/97% N_2 mixtures atmosphere. The prepared ITO thin films have a structure with full of cracks uniformly distributed such as [11]. All the SEM figures showed the presence of cracks, indicating the ITO thin films were not dense. The considerable porosity ($P \sim 51\%$) of the ITO thin films by using sol-gel method would not be removed even after annealing at a high temperature as the crystalline nanoparticle suspensions consists of an agglomeration of such particles [17]. Figures 5(a) and 5(b) show the average surface grain size of about 30.1 and 32.0 nm for the ITO films without annealing and with annealing at 400°C in 3% H_2/97% N_2 mixtures atmosphere, respectively. However, there are almost no significant changes in the morphology as the annealing temperature was further increased to 600°C, and the average surface grain size is about 32.3 nm.
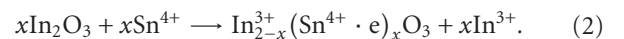
Figure 6 shows the AFM surface views (Scanning range: $10 \times 10\ \mu m^2$) of the ITO thin films treated without annealing, and with annealing at 400°C and 600°C in 3% H_2/97% N_2 mixtures atmosphere. The average surface grain size and root-mean-square (RMS) roughness were high with an increased annealing temperature. This result was associated with the tendency of the grain growth by fusing adjacent grains when sufficient energy for surface rearrangement is provided by annealing. Larger grains are associated with higher RMS roughness [18]. In our work, RMS roughness

and the average surface grain size were increased with the increased annealing temperature in the range from 2.0 to 4.8 nm, and 30.1 to 32.3 nm, for the ITO films without annealing and with annealing at 600°C in 3% H_2/97% N_2 mixtures atmosphere, respectively. The morphology of the prepared ITO thin films depended substantially on annealing temperature [19].

The average grain size from SEM data was significantly larger than the average crystallite size in the film bulk derived from the FWHM of the (222) diffraction peaks and the RMS roughness from the AFM results [20]. The significant difference between the average crystallite and grain size was determined from XRD and AFM measurement; the reason was due to the fact that the AFM measurement was more sensitive to the surface structure and that of the XRD measurement was sensitive to the structure of the film bulk. Thus, the columns grown during the deposition tend to have larger diameter at the surface, resulting in larger surface grains than average grain size in the film bulk [21].

Figure 7 displays the optical transmittance spectra of the ITO thin films treated without annealing and with annealing at 400°C and 600°C in 3% H_2/97% N_2 mixtures atmosphere. The maximum transmittance in the visible range (380–780 nm) is 85.6% when the ITO films annealed at 600°C and approximately 74.6% and 81.4% for the films treated without annealing and annealed at 500°C, respectively. The results agreed with those reported by Alam and Cameron They pointed out that the transmission in the visible range wavelengths was enhanced with increasing the annealing temperature due to crystallization and organic quantity [5].

As shown in Table 1, the conductivity of the prepared ITO films was in the range of 0.3×10^1 to 2×10^1 S/cm for films without annealing, and with annealing at 400°C and 600°C in 3% H_2/97% N_2 mixtures atmosphere. Since the resistivity is inverse to the conductivity, the resistivity of the prepared ITO films was in the range around 3×10^{-1} to 5×10^{-2} Ω-cm. Actually, the conductivity of the ITO thin films is mainly derived from the donor-doping effect generated though replacement of In ion sites by Sn ions in lattice and the oxygen vacancy caused by annealing process. When In_2O_3 is doped by Sn ions, due to approximate radii between In^{3+} and Sn^{4+}, In^{3+} ions site is easily replaced by Sn^{4+} ions site. The doping reaction can be expressed as [22]

$$x In_2O_3 + x Sn^{4+} \longrightarrow In_{2-x}^{3+}(Sn^{4+} \cdot e)_x O_3 + x In^{3+}. \tag{2}$$

The conductivity of the ITO thin films is affected by two major factors. One is the grain boundary scattering, and another is the ionized impurity centers scattering [19].
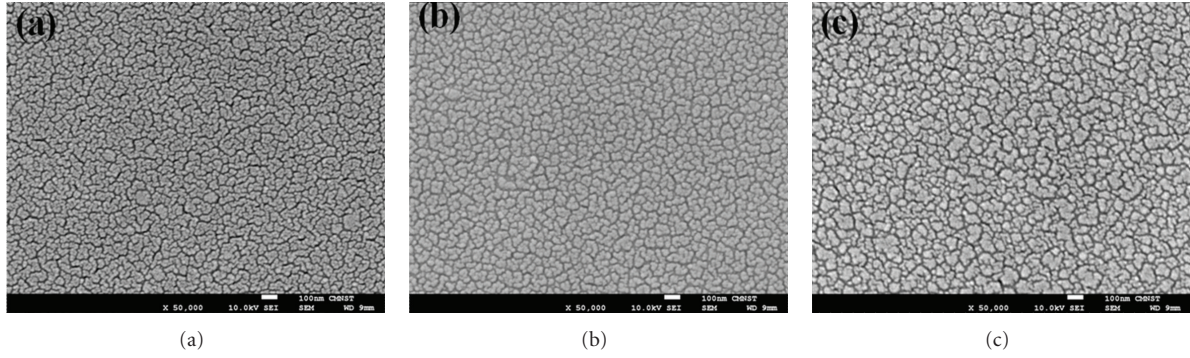
(a)   (b)   (c)

FIGURE 5: AFM surface views of the ITO thin films treated (a) without annealing and with annealing at (b) 400°C and (c) 600°C in 3% H$_2$/97% N$_2$ mixtures atmosphere.
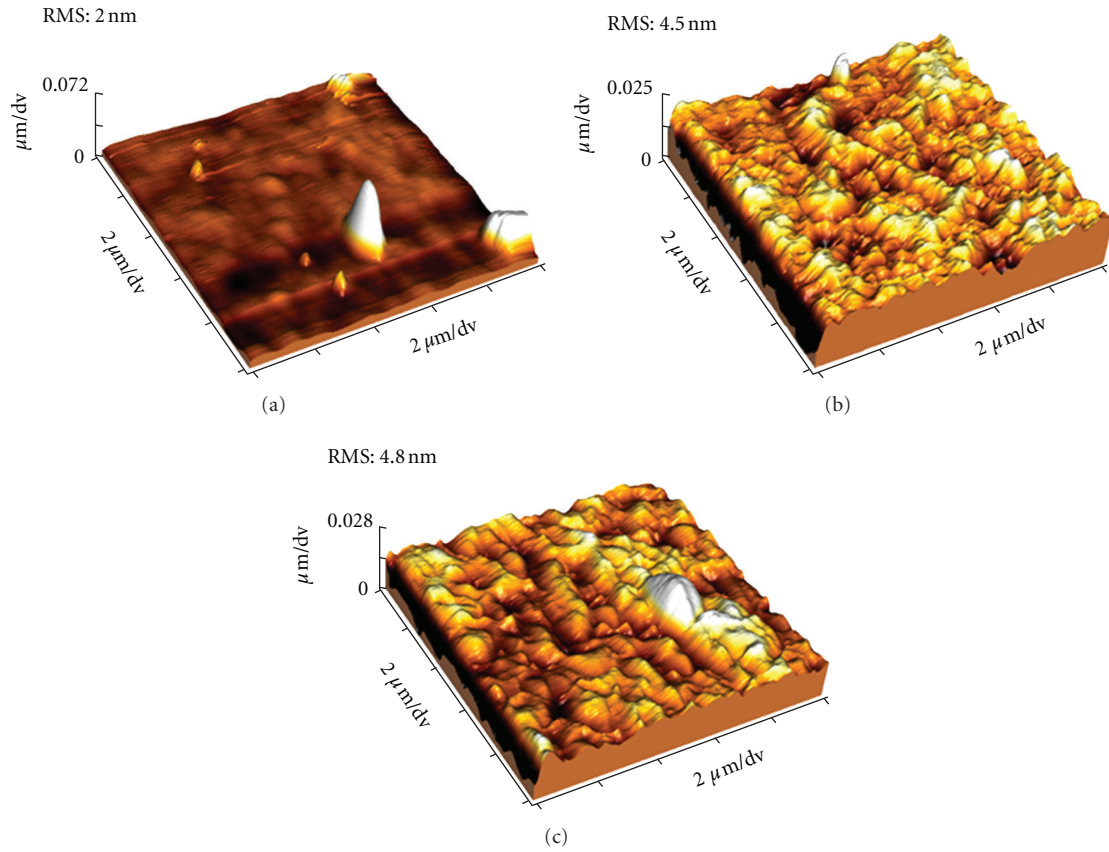

FIGURE 6: SEM images of the ITO thin films treated (a) without annealing and with annealing at (b) 400°C and (c) 600°C in 3% H$_2$/97% N$_2$ mixtures atmosphere.

The grain size gradually increases the proportion of well-ordered crystalline structures. Large grain size reduces the grain boundary scattering and enables the electron carriers to conduct smoothly. However, the ionized impurity centers served as the most important factor of the carrier concentration. The oxygen ion attracted by the doped ionized could be incorporated in lattice and segregated from the grain boundary, resulting in the distortion of the lattice and the generation of a neutral electron scattering center. As discussed in the Figures 4 and 6, the low conductivity of the prepared ITO films may be attributed to the undense film growth and the residual organic compounds, affecting the transportation of the carriers. The best resistivity is 5×10^{-2} Ω-cm obtained for the ITO film with an annealing temperature of 600°C owing to the mechanisms of the considerable porosity [8, 11, 23].
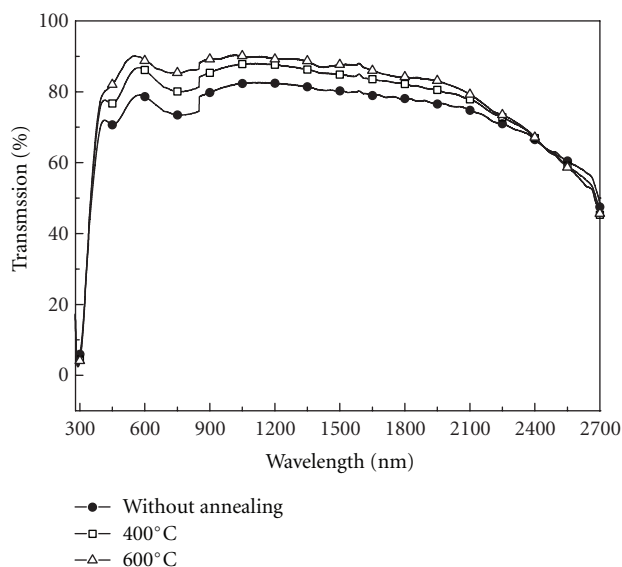
FIGURE 7: Optical transmittance spectra of the ITO thin films treated without annealing and with annealing at 400°C and 600°C in 3% H_2/97% N_2 mixtures atmosphere.

4. Conclusion

In this paper, the ITO thin films were synthesized onto the glass substrates by a sol-gel process using a dip-coating method. A strong dependence of microstructure, crystal quality, electrical, and optical properties under annealing treatment conditions was found. The XRD results showed the prepared ITO thin films were cubic In_2O_3 structure and the calculated crystal sizes were around 3.3 nm to 4.5 nm. The FTIR results showed the organic compounds could not be removed completely even when the postannealing temperature was operated at 600°C. The SEM images indicated the prepared ITO thin films were not dense. The AFM results showed the RMS roughness was increased with the increased annealing temperature due to crystal growth. Moreover, the maximum transmittance in the visible range (380–780 nm) of 85.6% and the best resistivity is 5×10^{-2} Ω-cm (namely, conductivity is 2×10^1 S/cm) were obtained for the ITO film treated with the annealing temperature of 600°C. It is verified that the electrical properties of the prepared ITO films are strongly related to the microstructure variation, especially resulted from the un-dense film growth and un-removed organic compounds of the precursors.

References

[1] P. K. Manoj, B. Joseph, V. K. Vaidyan, and D. S. D. Amma, "Preparation and characterization of indium-doped tin oxide thin films," *Ceramics International*, vol. 33, no. 2, pp. 273–278, 2007.

[2] R. Pan, S. Qiang, K. Liew, Y. Zhao, R. Wang, and J. Zhu, "Effect of stabilizer on synthesis of indium tin oxide nanoparticles," *Powder Technology*, vol. 189, no. 1, pp. 126–129, 2009.

[3] Y. C. Liang, "Surface morphology and conductivity of zirconium-doped nanostructured indium oxide films with various crystallographic features," *Ceramics International*, vol. 36, no. 5, pp. 1743–1747, 2010.

[4] O. Warschkow, D. E. Ellis, G. B. González, and T. O. Mason, "Defect structures of tin-doped indium oxide," *Journal of the American Ceramic Society*, vol. 86, no. 10, pp. 1700–1706, 2003.

[5] M. J. Alam and D. C. Cameron, "Investigation of annealing effects on sol-gel deposited indium tin oxide thin films in different atmospheres," *Thin Solid Films*, vol. 420-421, pp. 76–82, 2002.

[6] M. Quaas, H. Steffen, R. Hippler, and H. Wulff, "Influence of microstructure on oxygen diffusion in plasma-deposited In/Sn films," *Thin Solid Films*, vol. 420-421, pp. 306–311, 2002.

[7] E. S. Raj and K. L. Choy, "Microstructure and properties of indium tin oxide films produced by electrostatic spray assisted vapour deposition process," *Materials Chemistry and Physics*, vol. 82, no. 2, pp. 489–492, 2003.

[8] A. Solieman and M. A. Aegerter, "Modeling of optical and electrical properties of In_2O_3: Sn coatings made by various techniques," *Thin Solid Films*, vol. 502, no. 1-2, pp. 205–211, 2006.

[9] E. Celik, U. Aybarc, M. F. Ebeoglugil, I. Birlik, and O. Culha, "ITO films on glass substrate by sol-gel technique: synthesis, characterization and optical properties," *Journal of Sol-Gel Science and Technology*, vol. 50, no. 3, pp. 337–347, 2009.

[10] Z. H. Li, Y. P. Ke, and D. Y. Ren, "Effects of heat treatment on morphological, optical and electrical properties of ITO films by sol-gel technique," *Transactions of Nonferrous Metals Society of China*, vol. 18, no. 2, pp. 366–371, 2008.

[11] T. S. Renuga Devi and S. Gayathri, "FTIR and FT-Raman spectral analysis of paclitaxel drugs," *International Journal of Pharmaceutical Sciences Review and Research*, vol. 2, no. 2, pp. 106–110, 2010.

[12] I. Hamberg and C. G. Granqvist, "Evaporated Sn-doped In_2O_3 films: basic optical properties and applications to energy-efficient windows," *Journal of Applied Physics*, vol. 60, no. 11, pp. R123–R159, 1986.

[13] S. R. Ramanan, "Dip coated ITO thin-films through sol-gel process using metal salts," *Thin Solid Films*, vol. 389, no. 1-2, pp. 207–212, 2001.

[14] S. S. Kim, S. Y. Choi, C. G. Park, and H. W. Jin, "Transparent conductive ITO thin films through the sol-gel process using metal salts," *Thin Solid Films*, vol. 347, no. 1-2, pp. 155–160, 1999.

[15] L. Yang, X. He, and F. He, "ITO coated quartz fibers for heat radiative applications," *Materials Letters*, vol. 62, no. 30, pp. 4539–4541, 2008.

[16] B. L. Zhu, X. H. Sun, S. Guo et al., "Effect of thickness on the structure and properties of ZnO thin films prepared by pulsed laser deposition," *Japanese Journal of Applied Physics*, vol. 45, no. 10, pp. 7860–7865, 2006.

[17] A. Solieman and M. A. Aegerter, "Modeling of optical and electrical properties of In_2O_3: Sn coatings made by various techniques," *Thin Solid Films*, vol. 502, no. 1-2, pp. 205–211, 2006.

[18] E. Çetinörgü, S. Goldsmith, and R. L. Boxman, "The effect of annealing on filtered vacuum arc deposited ZnO thin films," *Surface and Coatings Technology*, vol. 201, no. 16-17, pp. 7266–7272, 2007.

[19] J. Liu, D. Wu, and S. Zeng, "Influence of temperature and layers on the characterization of ITO films," *Journal of Materials Processing Technology*, vol. 209, no. 8, pp. 3943–3948, 2009.

[20] S. Y. Chu, W. Water, and J. T. Liaw, "Influence of postdeposition annealing on the properties of ZnO films prepared by RF magnetron sputtering," *Journal of the European Ceramic Society*, vol. 23, no. 10, pp. 1593–1598, 2003.

[21] J. A. Thornton, "High rate thick film growth," *Annual Review of Materials Research*, vol. 7, pp. 239–260, 1977.

[22] Z. H. Li and D. Y. Ren, "Fabrication and structure characterization of ITO transparent conducting film by sol-gel technique," *Transactions of Nonferrous Metals Society of China*, vol. 17, no. 3, pp. 665–668, 2007.

[23] L. Yang, X. He, D. Ge, and H. Wei, "Densification study of ITO films during high temperature annealing by GISAXS," *Physica B*, vol. 404, no. 16, pp. 2146–2150, 2009.

Research Article

Performance Degradation of Dye-Sensitized Solar Cells Induced by Electrolytes

Ru-Yuan Yang,[1] Huang-Yu Chen,[2] and Fu-Der Lai[2]

[1] *Graduate Institute of Materials Engineering, National Ping-Tung University of Science and Technology, Pingtung 912, Taiwan*
[2] *Institute of Electro-Optical Engineering, National Kaohsiung First University of Science and Technology, Kaohsiung 811, Taiwan*

Correspondence should be addressed to Ru-Yuan Yang, ryyang@mail.npust.edu.tw

We investigated the change of the electric characteristics in dye-sensitized solar cell (DSSC) when the electrolyte has been injected and measured initially and lately for a period of time. It was found that the short-circuit current density decreased from 9.799 mA/cm^2 to 7.056 mA/cm^2 and the fill factor increased from 0.406 to 0.559 when the cell had stood for an hour, while the open-circuit photovoltage did not change due to fixed difference between the Fermi level of TiO$_2$ and the oxidation-reduction potential of electrolyte. The results can be explained by using the variation of the series resistance in the equivalent circuit of the DSSC.

1. Introduction

Dye-sensitized solar cells (DSSC) have attracted much attention ever since Grätzel et al. demonstrated the possibility to convert solar energy to electricity with a photoelectrochemical dye-sensitized device [1]. The DSSC provides a technically and economically credible alternative concept to present day p-n junction photovoltaic devices. The development of these new types of solar cell is promoted by the increasing public awareness that the earth's oil reserves will run out during this century. Because the energy needs of the planet will at least double within the next 50 years, the stage is set for a major shortage of energy supply unless renewable sources can cover the substantial deficit that fossil fuels can no longer furnish.

This accomplishes the optical absorption and charge separation processes by the association of a sensitizer as a light-absorbing material with a wide-band-gap semiconductor of mesoporous or nanocrystalline morphology [1–3]. It also offers the prospect of very low cost fabrication without expensive and energy-intensive high-temperature and high-vacuum processes, compatibility with flexible substrates, and variety of presentations and appearances to facilitate market entry, both for domestic devices and in architectural or decorative applications. Generally, the semiconductor, which accepts the electron from the sensitizer and transfers it to the electrode, is nanocrystalline anatase TiO$_2$ which is mesoporous because of high surface area. High surface area of TiO$_2$ thin film improves the adsorption of sensitizer and hence increases the light-harvesting capacity of the mesoporous film. However, the electrolyte may penetrate into the mesoporous film and contact the dye-free TiO$_2$ and the electrode surface, resulting in the increase of the reverse saturation current. On the other hand, it also increases the contact area between the electrolyte and the sensitizer so that facilitates the reduction of I_3^- by the combination of the hole. It was found that the short-circuit photocurrent decreased and the fill factor of the dye-sensitized solar cell increased as time goes on.

In this study, the change of the electric characteristics in dye-sensitized solar cell (DSSC) when the electrolyte has been injected and measured initially and lately for a period of time was investigated. The short-circuit photocurrent density (J_{sc}) and the fill factor (F.F.) were varied and the results can be explained by using the variation of the series resistance in the equivalent circuit of the DSSC.

2. Experimental Apparatus and Procedure

2.1. Preparing the Working Electrode. A TiO$_2$ thin-film electrode was designed and fabricated for use in a dye-sensitized solar cell. This TiO$_2$ thin-film was deposited on the top of
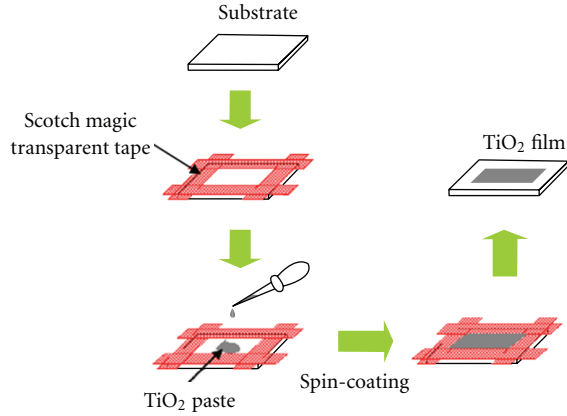
FIGURE 1: The procedure of preparing the working electrode.

FIGURE 2: The photograph of the working electrode.

an FTO-glass (Fluorine doped tin oxide, SnO$_2$:F) substrate, which has a size of $20 \times 20 \times 3$ mm and a sheet resistance of 8 Ω/sq. The TiO$_2$ particles (P-25) are composed of 30% rutile and 70% anatase, with a particle size range (<100 nm).

Figure 1 shows the procedure of preparing the working electrode of DSSC with a layer of TiO$_2$ particles and the steps are described as follows. (1) Diluting 40 μL of acetylacetone in 1 mL of de-ionic (DI) water; (2) mixing 1 g of TiO$_2$ particles with the diluted acetylacetone, and stir well to make the colloid of TiO$_2$ particles; (3) adjusting the glutinosity of the colloid of TiO$_2$ particles by adding 1.5 mL of DI water and 40 μL of surfactant (Triton-100, C$_8$H$_{17}$C$_6$H$_4$(OCH$_2$CH$_2$)nOH), and then homogenize the colloid of TiO$_2$ particles for 30 minute in a mortar; (4) dropping the quantitative colloid of TiO$_2$ particles on the top of the F:SnO$_2$ (FTO) glass substrate, and then spin coat the working electrode with rotational speed of 3000 rpm; (5) drying the working electrode with a layer of TiO$_2$ particles at room temperature for 10 minute, and then sinter this working electrode at 500°C for 30 minutes in a high-temperature furnace; (6) immersing the FTO-glass substrate with a layer of TiO$_2$ particles into the (3×10^{-4} mol/L) solution of N-719 dye (Ruthenium, RuL$_2$(NCS)$_2$) and ethyl alcohol (CH$_3$CH$_2$OH, 95%) for 24 hours at room temperature. A conventional working electrode with a layer of nanocrystalline TiO$_2$ on the FTO-glass substrate was fabricated using above procedures to demonstrate the feasibility and advantages of the working electrode with a layer of TiO$_2$ particles. An α-step (Dekeak 6 M) surface profiler was utilized to obtain the surface profile of the thin film and the average thickness of the thin film on the FTO-glass substrate of the working electrode. The thickness of the TiO$_2$ thin films was about 10 μm. Figure 2 shows the practical working electrode.

2.2. Assembling the DSSC. Figure 3 shows the schematic of the DSSC. The thin film on the FTO-glass substrate of the working electrode was fringed using the Scotch magic transparent tape (3 M). Then, the working electrode and the counter electrode that a thin film of platinum was deposited on the FTO-glass substrate using a ion sputter (Hitachi E-1010) were fitted together, such that the space between the
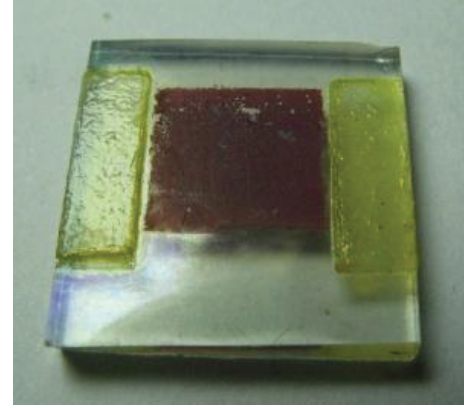
two electrodes was adjusted to approximately 160 μm for embarking the liquid electrolyte. After sealing, the liquid electrolyte, which was composed of 0.5 M lithium iodine (LiI) and 0.05 M iodine (I$_2$) in 3-methoxypropionitrile, was injected into the cell through a hole on the cell that was prepared in advance.

2.3. Testing. A home-made *I-V* measurement system was adopted to measure the open-circuit photovoltage and short-circuit photocurrent of the DSSC. A solar simulator with a 500 W halogen lamp and a light intensity of 100 mW/cm^2, was employed to illuminate the DSSC. In addition, the power conversion efficiency η of the DSSC was determined by

$$\eta(\%) = \frac{V_{oc}J_{sc}\text{FF}}{P_{in}} \times 100. \tag{1}$$

In (1), V_{oc}, J_{sc}, and P_{in} represent the open-circuit voltage, the short-circuit current density, and the incident light power (100 mw/cm^2), respectively. Moreover, the fill factor FF is given by

$$\text{FF} = \frac{V_{max}J_{max}}{V_{oc}J_{sc}}. \tag{2}$$

In (2), V_{max} and I_{max} represent the voltage and the current at the maximum output power point, respectively. The *I-V* characteristics of the prepared DSSC were measured at initial assembling stage and at one hour lately.

3. Results and Discussion

Figure 4 shows *I-V* characteristics of the DSSC when the electrolyte is just injected into the space between the working electrode and the counter electrode. The measured V_{oc}, J_{sc}, and F.F. are 9.799 mA/cm^2, 0.658 V, and 0.406, respectively. Figure 5 shows *I-V* characteristics of the dye-sensitized solar cell after the electrolyte has been injected and stay for one hour. The measured V_{oc}, J_{sc}, and F.F. are 7.056 mA/cm^2, 0.668 V, and 0.559, respectively. as Comparing Figure 4 to Figure 5, it is found that the J_{sc} decreases from 9.799 mA/cm^2 to 7.056 mA/cm^2 and F.F increases from 0.406 to 0.559. The V_{oc} does not change due to the fixed difference between
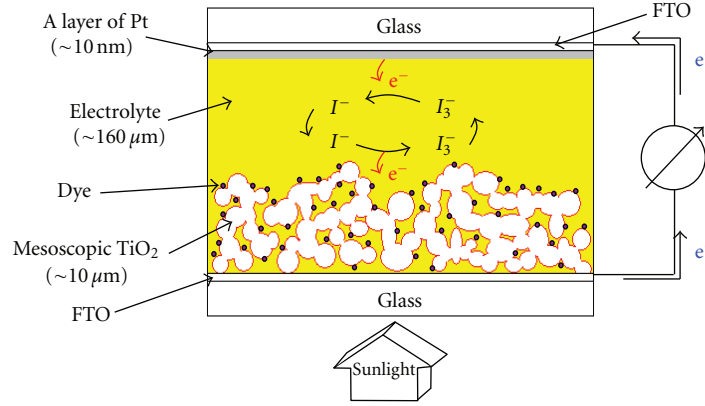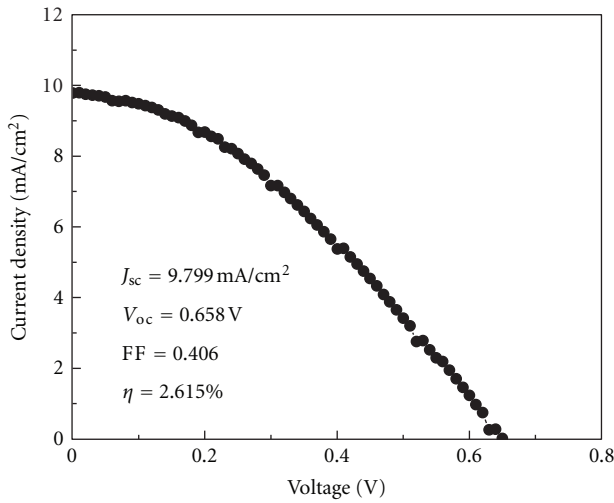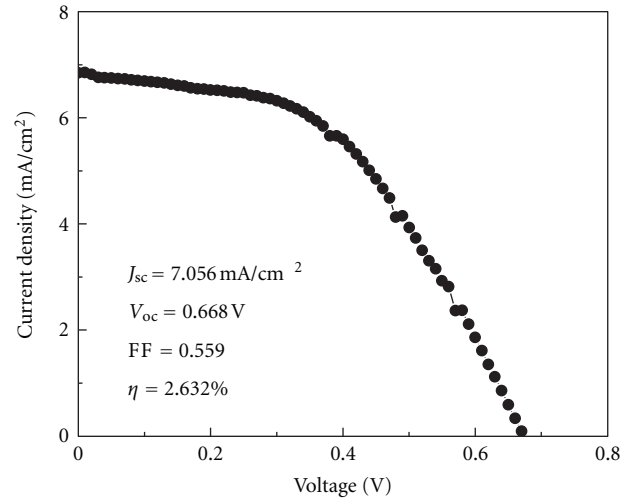
FIGURE 3: Schematic of the dye-sensitized solar cell.

FIGURE 4: I-V curve of DSSC when the electrolyte is just injected.

FIGURE 5: I-V curve of DSSC when the electrolyte has been injected and stay for one hour.

the Fermi level of TiO$_2$ and the oxidation-reduction potential of electrolyte. To understand the difference in their J_{sc} for the measurement at initial assembling stage and at one, two, three and so forth hours lately. We conduct the standard I-V curve of the solar cell and discuss the change of the series resistance and the shunt resistance.

It has been known that the tangent slope of vertical part (near V_{oc}) is proportional to the reciprocal of the series resistance ($1/R_s$) and the tangent slope of transverse part (near J_{sc}) is proportional to the reciprocal of the shunt resistance ($1/R_{sh}$). When R_{sh} increase or/and R_s decrease, F.F. will become better. The tangent slope of V_{oc} part in Figure 5 is larger than that in Figure 4, which means R_s decreases as time goes on. However, the tangent slope of I_{sc} does not change obviously so that R_{sh} is almost the same. We thus discuss the factor that affects the series resistance R_s and ignores the shunt resistance R_{sh}.

The series-internal resistance of DSSCs was investigated by some researchers based on an equivalent circuit of DSSCs [4, 5]. It was found that series-internal resistance correlates with the charge-transfer at Pt counter electrode, TCO substrate resistance, and Nernstian diffusion in the electrolyte. According to these, the equivalent circuit of DSSCs is constructed as shown in Figure 6. The series resistance is the sum of the charge transfer resistance at Pt/electrode interface (R_1), the diffusion resistance of I_3^- ions in electrolyte (R_2), and the sheet resistance of TCO (R_h). Because R_1 and R_h relate to the property of the material, they cannot change as time goes on. We think the major factor that influences R_s must be R_2. The probable explanation is that the electrolyte only contacts the top surface of TiO$_2$ thin film when the electrolyte is just injected. However, the electrolyte may permeate into the mesoporous film after an hour and the contact area with dye-adsorbed TiO$_2$ will increase, so the charge-transfer from the electrolyte to the oxidized dye will be accelerated. The large contact area between the electrolyte and the dye-adsorbed TiO$_2$ film improve the rate of I_3^- reduction and hence decrease R_s.

According to the diode equation that correlates with Figure 6:

$$I = I_{ph} - I_o \left\{ \exp\left[\frac{q(V + IR_s)}{nkT} \right] - 1 \right\} - \frac{V + IR_s}{R_{sh}}, \quad (3)$$
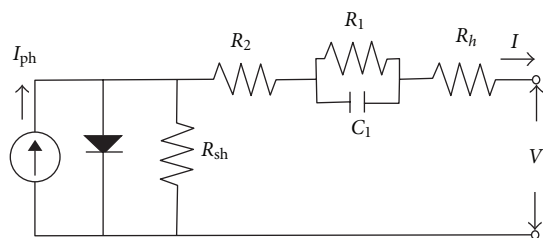
FIGURE 6: Equivalent circuit based on current-voltage characteristics of DSSCs. The sum of R_1, R_2, and R_h corresponds closely to the series resistance of DSSCs. C_1 is capacitance elements.

where I_{ph} is the ideal photocurrent, I_0 is the reverse saturation current, n is the ideality factor whose value is between 1 and 2 for the DSSC, R_s is the series resistance which is the sum of R_1, R_2, and R_h, and R_{sh} is the shunt resistance. The gain in open circuit voltage can be calculated from (3):

$$V_{oc} = \frac{nkT}{q} \ln\left[\frac{I}{I_o} - \frac{V_{oc}}{I_o R_{sh}} + 1 \right]. \tag{4}$$

As R_{sh} increase, V_{oc} will also increase. as comparing Figure 4 to Figure 5, it is found that V_{oc} does not change obviously. Since $1/R_s$ is unchanged, it confirms that the shunt resistance in DSSCs is almost the same as time goes on.

The short circuit current can be obtained from (3) when $V = 0$, and it can be found that I_{sc} will increase as R_s decreases. However, J_{sc} decreases from 9.799 mA/cm^2 in Figure 4 to 7.056 mA/cm^2 in Figure 5. It must be the influences of the dark current which correlates with the recombination of charge carriers by reduction of I_3^- at dye-free TiO$_2$ surface and bare FTO surface exposed to electrolyte through porous electrode [6]. As we discussed before, the electrolyte will permeate into the mesoporous film when DSSC has been staid for an hour. It may apply the electrolyte to contact the dye-free TiO$_2$ surface and even the FTO surface, so that accelerates the recombination of the charge carriers from the conduct band of TiO$_2$ to the electrolyte and produces the reverse saturation current. The increase of the dark current lowers I_{sc} seriously so that it is important to modify the working electrode surface to decrease the reverse charge flow.

Based on the above discussion, it is known how to improve the performance of DSSCs by modifying the interface between the working electrode and the electrolyte, as investigated by some research workers [7–9]. Su et al. fabricated layer-by-layer Au nanoparicles, which were prepared using chemical reduction method, onto the working electrode as a Schottky barrier in a water-based DSSC [10]. It was found that an interfacial blocking layer could suppress the interfacial recombination between TiO$_2$ and excited dye molecules or I^-/I_3^- couple, which led to an improvement on cell performance [7–9]. Moreover, in order to improve the performance of DSSCs, it is also necessary to suppress the dark current. The reverse charge flow, recapture of the electron by the electrolyte, could be impaired by judicious design of the sensitizer. It can also form a tightly packed insulating monolayer blocking the dark current.

Consequently, decreasing the recombination of charges in the dye or electrolyte is one of the important issues to increase the conversion efficiency of DSSC and is worthy of ongoing study.

4. Conclusion

In this study, we discussed the change of the current-voltage characteristics in DSSCs as time goes on and found that fill factor (F.F) got better but short circuit current density J_{sc} decreased. The results were explained by using the variation of the series resistance in the equivalent circuit of the DSSC. The increase of F.F. may result from the decrease of series resistance R_s due to the electrolyte permeating into the mesoporous working electrode and hence increase the contact area with the dye-adsorbed TiO$_2$. However, it also applies the electrolyte to contact the dye-free TiO$_2$ surface and even the FTO surface, so that accelerates the recombination of the charge carriers from the conduct band of TiO$_2$ to the electrolyte and produces the reverse saturation current.

References

[1] B. O'Regan and M. Grätzel, "A low-cost, high-efficiency solar cell based on dye-sensitized colloidal TiO$_2$ films," *Nature*, vol. 353, no. 6346, pp. 737–740, 1991.

[2] M. Grätzel, "Photoelectrochemical cells," *Nature*, vol. 414, no. 6861, pp. 338–344, 2001.

[3] A. Hagfeldt and M. Grätzel, "Molecular photovoltaics," *Accounts of Chemical Research*, vol. 33, no. 5, pp. 269–277, 2000.

[4] L. Han, N. Koide, Y. Chiba, and T. Mitate, "Modeling of an equivalent circuit for dye-sensitized solar cells," *Applied Physics Letters*, vol. 84, no. 13, pp. 2433–2435, 2004.

[5] L. Han, N. Koide, Y. Chiba et al., "Improvement of efficiency of dye-sensitized solar cells by reduction of internal resistance," *Applied Physics Letters*, vol. 86, no. 21, Article ID 213501, 3 pages, 2005.

[6] W. J. Lee, E. Ramasamy, D. Y. Lee, and J. S. Song, "Glass frit overcoated silver grid lines for nano-crystalline dye sensitized solar cells," *Journal of Photochemistry and Photobiology A*, vol. 183, no. 1-2, pp. 133–137, 2006.

[7] A. Kay and M. Grätzel, "Dye-sensitized core-shell nanocrystals: improved efficiency of mesoporous tin oxide electrodes coated with a thin layer of an insulating oxide," *Chemistry of Materials*, vol. 14, no. 7, pp. 2930–2935, 2002.

[8] E. Palomares, J. N. Clifford, S. A. Haque, T. Lutz, and J. R. Durrant, "Slow charge recombination in dye-sensitised solar cells (DSSC) using Al$_2$O$_3$ coated nanoporous TiO$_2$ films," *Chemical Communications*, no. 14, pp. 1464–1465, 2002.

[9] E. Palomares, J. N. Clifford, S. A. Haque, T. Lutz, and J. R. Durrant, "Control of charge recombination dynamics in dye sensitized solar cells by the use of conformally deposited metal oxide blocking layers," *Journal of the American Chemical Society*, vol. 125, no. 2, pp. 475–482, 2003.

[10] Y. H. Su, W. H. Lai, L. G. Teoh, M. H. Hon, and J. L. Huang, "Layer-by-layer Au nanoparticles as a Schottky barrier in a water-based dye-sensitized solar cell," *Applied Physics A*, vol. 88, no. 1, pp. 173–178, 2007.

Research Article

Modeling Approach for Determining Equivalent Optical Constants of Plastic Shading Nets under Solar Radiation Conditions

A. M. Abdel-Ghany[1, 2] and I. M. Al-Helal[1]

[1] *Department of Agricultural Engineering, College of Food and Agriculture Sciences, King Saud University, P.O. Box 2460, Riyadh 11451, Saudi Arabia*

[2] *Mechanical Power Engineering Department, Faculty of Energy Engineering, South Valley University, Aswan 81528, Egypt*

Correspondence should be addressed to A. M. Abdel-Ghany, aghany@ksu.edu.sa

The radiative properties of several plastic shading nets were measured under natural solar radiation conditions. We found that the plastic nets behave as homogeneous translucent materials (e.g., plastic film, plastic sheets, and glass). Based on this behavior, we suggest that it is possible to treat plastic nets as translucent materials and to characterize them with equivalent optical constants (i.e., equivalent refractive indexes, n_{eq}, and equivalent extinction coefficients, σ_{eq}). Here a physical model to determine n_{eq} and σ_{eq} of plastic nets was described in analogy to homogeneous translucent materials. We examined three groups of nets based on their color (black, black-green, and beige). Each group consisted of nets with four or five different porosities. Nets of each group had almost the same texture structure. For each group, we derived an equation for n_{eq} as a function of the net porosity and determined an average value for σ_{eq}. Once values of n_{eq} and σ_{eq} were determined, the solar radiative properties of a net could then be calculated from n_{eq} and σ_{eq} for any incident angle of solar beam radiation without the need of measurements. The present model was validated by comparing the calculated with the measured radiative properties of three nets at different incident angle of solar beam radiation. The calculated radiative properties reasonably agreed with measured values.

1. Introduction

During the last decade, the use of plastic nets for shading agricultural industrial and residential structures in hot and sunny regions has steadily expanded because plastic nets offer many economical and environmental benefits [1–4]. These include (i) reduction or elimination of energy consumption used for heating or cooling structures, (ii) reduction of crop transpiration as well as water consumption for irrigation in agriculture structures in arid regions, and (iii) improvement in environmental and human-health conditions by reducing the need for pesticides. The diffusive nature of the net threads causes the incident beam radiation to be scattered forward (specularly and diffusively) during transmission [5]. This provides a uniform radiation distribution inside structures covered with nets to add more advantages to plastic nets applications. Various types of plastic nets with different colors and different shading powers are popular in the markets and are used for many purposes in many parts of the world. Commercial nets are usually defined by the following (i) the net porosity (ϕ), that is, the surface empty area (uncovered by the plastic threads) divided by the total surface area of the net. The value of ϕ is usually determined by image processing or solar radiation transmission [6]. (ii) The shading factor (SF), defined as the percentage of global solar radiation that the net is able to block. SF strongly depends on the incident angle of the beam radiation (θ), and to estimate the value of SF for a net correctly, the directional solar radiative properties (θ dependence) of the net should be determined. Accordingly, the directional solar radiative properties of nets are essentially needed to characterize different types of plastic nets according to their shading power. However, little information about how to determine these properties is available in the literature.

Some research groups have investigated the radiative properties of different types of plastic net or total net-covered structure models in laboratories under artificial lighting [2–4, 7]. In order to replace expensive measuring techniques in laboratories, we developed a simple method for measuring the radiative properties of nets under natural conditions of global, diffuse, and direct beam solar radiation, and under natural conditions of the photosynthetically active radiation (PAR) [8, 9]. The method was used to test nets with different colors, porosities, and texture structures. Even though, nets are three-dimensional, nonhomogeneous, and porous materials, the behaviors of the plastic nets under solar radiation conditions were found to be similar to those of translucent homogeneous materials (e.g., plastic films, glass and rigid plastic sheets such as polycarbonate and acrylic) [8, 9]. In other words, the changes in the global, diffuse, and direct beam transmittances and reflectances of nets with the incident angle (θ) were similar to those of different translucent materials that were measured under natural conditions of solar radiation [10–14]. This makes it possible to determine optical constants, in analogy to homogeneous transparent materials, to be used for calculating the radiative properties of nets. This is because calculation methods are preferable and easier than the measuring methods which are quite difficult and prohibitively expensive. Accordingly, the goal of the present study was to develop a theoretical model to investigate equivalent optical constants (i.e., equivalent refractive indexes and equivalent extinction coefficients) for plastic nets in analogy to homogeneous translucent materials. Three groups of nets (i.e., a black group, beige group, and black-green group) were selected to develop the model.

2. Materials and Methods

2.1. The Plastic Net Materials.
The nets selected for testing were classified into three groups. Nets in each group have the same color, same texture structure, and different porosities (ϕ). The nets were locally produced by Saudi companies. Samples of the nets (5 cm × 5 cm) were scanned at a resolution of 4800 dpi with a flatbed scanner (HP-5590). Photos of the scanned nets were magnified several times and converted into high-contrast black (thread projection area) and white (empty area) colors using Adobe Photoshop software. The resulting photos showed the net threads as black on a white background. The porosity (the empty area divided by the total surface area of the net, ϕ) of each net was estimated. The three groups were the black group having porosities ϕ of 0.30, 0.36, 0.43, 0.54, and 0.64; the beige group having porosities ϕ of 0.32, 0.34, 0.36, and 0.45; the black-green group having porosities ϕ of 0.45, 0.46, 0.48, 0.50, and 0.51. In the latter group, the texture was interlaced threads made of black and green plastic robs knitted together. Photos of the tested nets (one from each group) are shown in Figure 1.

2.2. The Equivalent Optical Constants Model.
In the case of homogeneous translucent materials (e.g., plastic films, plastic sheets, or glass), the measured radiative properties (reflectance, transmittance, and absorptance) are referred to as effective properties. This is because the incident beam over the material surface suffers an infinite number of multiple internal reflections inside the material itself (Figure 2). With each internal reflection, there are transmitted and reflected portions below and above the material surfaces. The summation of the reflected components above the material surface is the effective reflectance and of those below the material surface is the effective transmittance; both can be measured using radiation sensors. According to [5], transmission of direct beam radiation through a plastic net was characterized as (i) the unscattered beam that is transmitted through the net pores, (ii) the beam that is reflected forward on the thread surfaces specularly, and (iii) the beam that is diffused during transmission. On the other hand, the reflected beam will be a combination of specularly reflected beam, and backward scattered beam. For several types of nets (having different colors, porosities, and texture structures) tested in [5], the forward diffused beam was less than 20% of the incident beam radiation. For the modeling approach, the unscattered beam, the specularly reflected (forward or backward) beam and the diffused beam were assumed to have the same characteristic manner and were considered as direct beams transmitted or reflected from the net. In analogy to homogeneous materials, the effective transmittance and reflectance of a plastic net to the direct beam solar radiation (τ_r and ρ_r) can be expressed as [15] by

$$\tau_r = \frac{\tau^*(1-\rho^*)}{1-(\tau^*\rho^*)^2}, \qquad \rho_r = \rho^*(1+\tau^*\tau_r), \qquad (1)$$

where τ^* is the transmittance of the beam radiation due to absorption only in the net material with a porosity ϕ and a solid matrix of $(1-\phi)$; ρ^* is the interface reflectance between the net surface and air.

By eliminating ρ^* from (1) a second-order algebraic equation with the unknown τ^* can be obtained. By solving the roots of this equation, the value of τ^* is given by [15] as

$$\tau^* = \left\{\frac{\tau_r^2-(1-\rho_r)^2}{2\tau_r}\right\} \pm \left\{\left(\frac{\tau_r^2-(1-\rho_r)^2}{2\tau_r}\right)^2+1\right\}^{1/2}. \qquad (2)$$

Reasonable (i.e., positive) values for τ^* are obtained by considering the plus sign of (2). The input parameters to (1) and (2) are the transmittance and reflectance of the net to direct beam radiation (τ_r and ρ_r) that can be measured using a pyranometer underneath the net and an albedometer above the net. The value of ρ^* is obtained from the direct substitution of τ^* in (1). Once values of τ^* and ρ^* were determined one time (e.g., at normal incidence), the equivalent optical constants (n_{eq} and σ_{eq}) of the plastic net can be determined, in analogy to homogeneous translucent materials, as follows.

The interface reflectance ρ^* at normal incidence between the air ($n = 1$) and the net surface having the equivalent refractive index (n_{eq}) is given by

$$\rho^* = \frac{\left(n_{\text{eq}}-1\right)^2}{\left(n_{\text{eq}}+1\right)^2}. \qquad (3)$$

(mm)
Image of a beige net

(mm)
Image of a black-green net
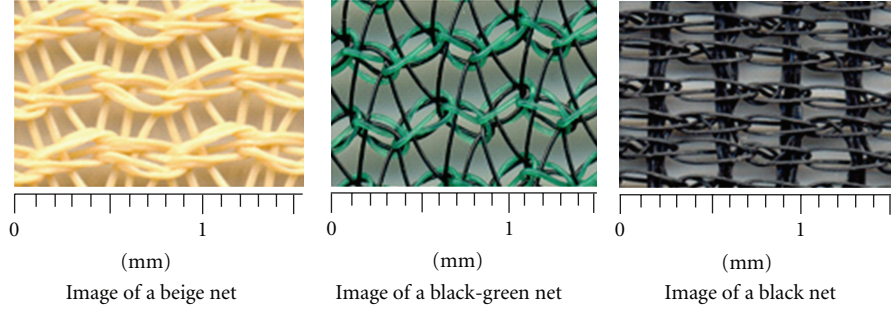
(mm)
Image of a black net

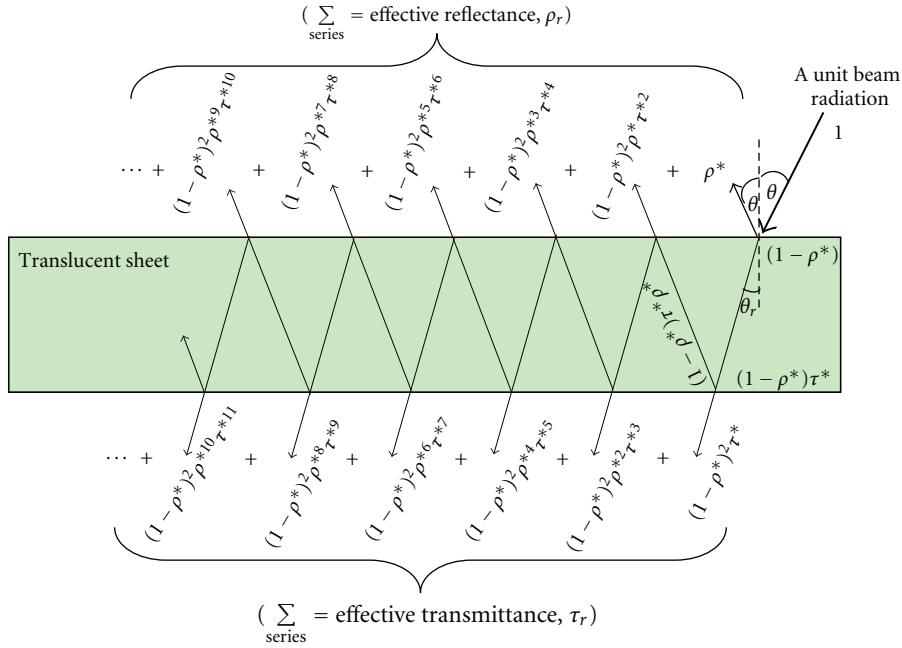FIGURE 1: Scanner images of a net in each group tested in this study.

FIGURE 2: Tracing of a unit beam radiation through a translucent sheet to illustrate the concept of the effective reflectance and effective transmittance of the sheet.

Also at normal incidence, the transmittance due to absorption (τ^*) and the equivalent absorption coefficient (σ_{eq}) of the net material can be expressed in similar manner of the homogeneous translucent films by replacing the film thickness with the net density or net solidity $(1 - \phi)$, ϕ is the net porosity. Thus, the relation between τ^* and σ_{eq} is given by

$$\tau^* = \text{Exp}\left\{-\sigma_{eq}(1 - \phi)\right\}. \tag{4}$$

In (4), σ_{eq} is dimensionless whereas the unit of the absorption coefficient of a homogeneous translucent sheet is mm^{-1} if the sheet thickness is in mm.

Once the values of the equivalent optical constants (σ_{eq} and n_{eq}) are determined for a net, the directional radiative properties of this net can be calculated at any incidence angle (θ) of the beam radiation. In this case, the directional

interface reflectance (ρ_θ^*) between the net surface and air is given by [12, 13] as

$$\rho_\theta^* = \frac{1}{2}\left\{\frac{\sin^2(\theta - \theta_r)}{\sin^2(\theta + \theta_r)} + \frac{\tan^2(\theta - \theta_r)}{\tan^2(\theta + \theta_r)}\right\},$$

$$\theta_r = \sin^{-1}\left(\frac{\sin\theta}{n_{eq}}\right), \tag{5}$$

where θ_r is the equivalent angle of refraction for a beam radiation penetrates through the net. The directional transmittance due to absorption (τ_θ^*) is given by

$$\tau_\theta^* = \text{Exp}\left\{\frac{-\sigma_{eq}(1 - \phi)}{\cos\theta_r}\right\}. \tag{6}$$

The directional radiative properties, with respect to the direct beam radiation, of a plastic net can be obtained by
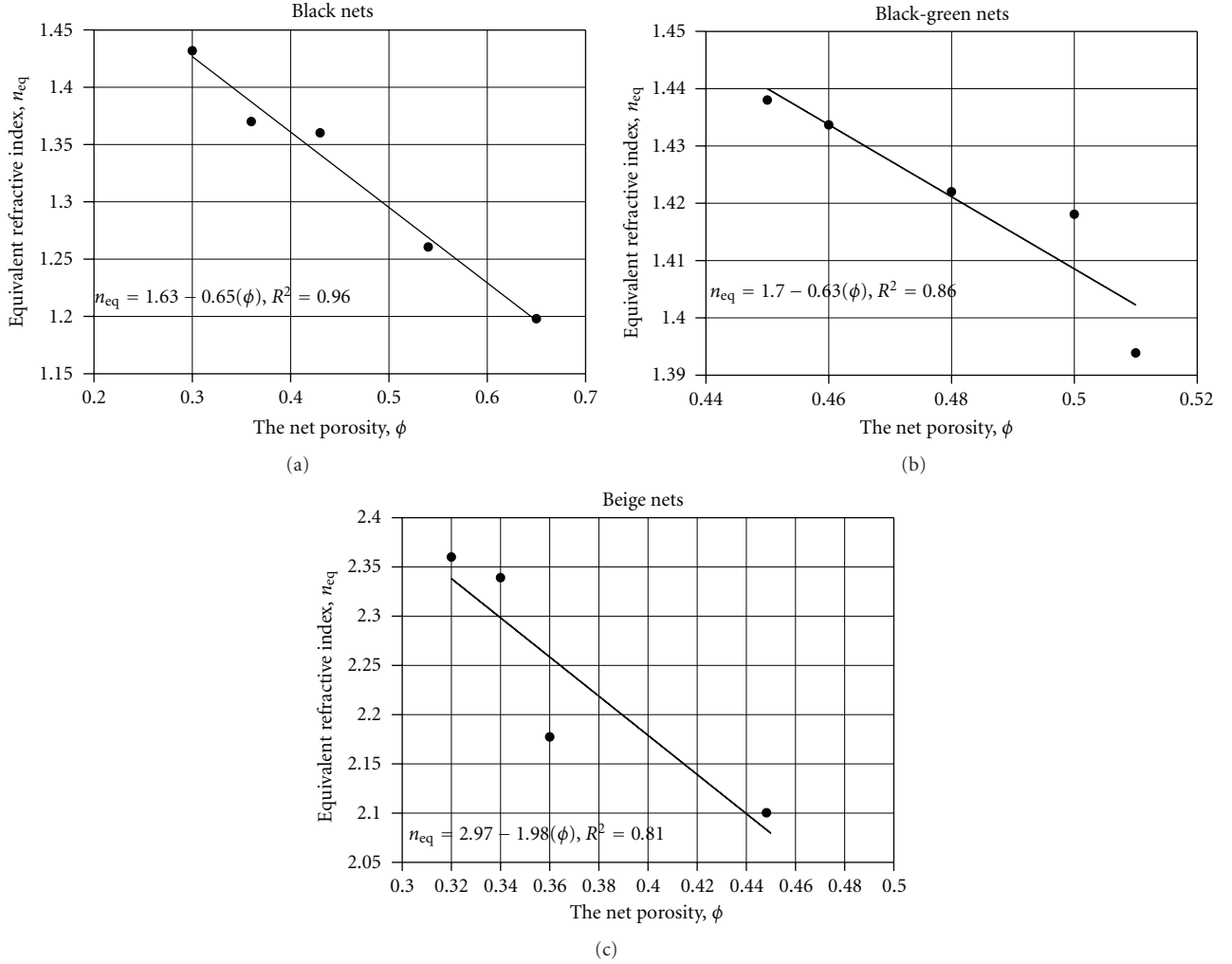
(a)

(b)

(c)

FIGURE 3: The equivalent refractive index (n_{eq}) as affected by the porosity of the tested nets: (a) is for the black group, (b) for the black-green group, and (c) for the beige group.

resubstituting τ_θ^* and ρ_θ^* into (1) to obtain τ_r and ρ_r for the desired direction. The diffuse solar radiation incident over a surface can be treated as a direct beam radiation with an incidence angle (θ) of 60° [12]. Thus the directional transmittance and reflectance of a net with respect to the global solar radiation (τ_g and ρ_g) are defined by

$$\tau_g = \tau_{r,60°}I_D + (1 - I_D)\tau_r,$$
$$\rho_g = \rho_{r,60°}I_D + (1 - I_D)\rho_r, \tag{7}$$

where I_D is the diffuse index estimated as (D_i/S_i) at the desired direction θ.

2.3. Measuring the Required Parameters.

For determining the transmittance and reflectance of the net to direct beam solar radiation (τ_r and ρ_r) to be used as input parameters to (1) and (2), the experiment was conducted on the roof of the building of the Agricultural Research and Experiment Station, Agriculture Engineering Department, King Saud University (Riyadh, Saudi Arabia, 46° 47′ E, longitude and

24° 39′ N, latitude). The measurements were conducted at around solar noon on clear, sunny days from September 10 to September 25, 2011. One pyranometer, CMP3 (Kipp & Zonen B.V. Inc., USA), and one albedometer, CMA-11 (Kipp & Zonen B.V. Inc., USA) were used. Each net sample was tacked onto a black painted wooden frame (50 cm × 60 cm × 30 cm). The frame was oriented toward the sun, so that incidence angle of the solar beam radiation (θ) was nearly zero. The transmitted global solar radiation (S_t) was measured below the net surface using the pyranometer. The incident and reflected global solar radiation (S_i and S_r) were measured above the net sample using the albedometer. This procedure was repeated while shading the frame with an opaque plate to measure the diffuse solar radiation components below (D_t) and above (D_i, D_r) the net sample. The measured parameters were recorded every 10 seconds, averaged over one-minute intervals and saved in a data logger (LI-1400, 9 channels, LI-COR, Inc.). For each parameter, five values were measured at normal incidence, and the average value was obtained. The sensors had been calibrated before
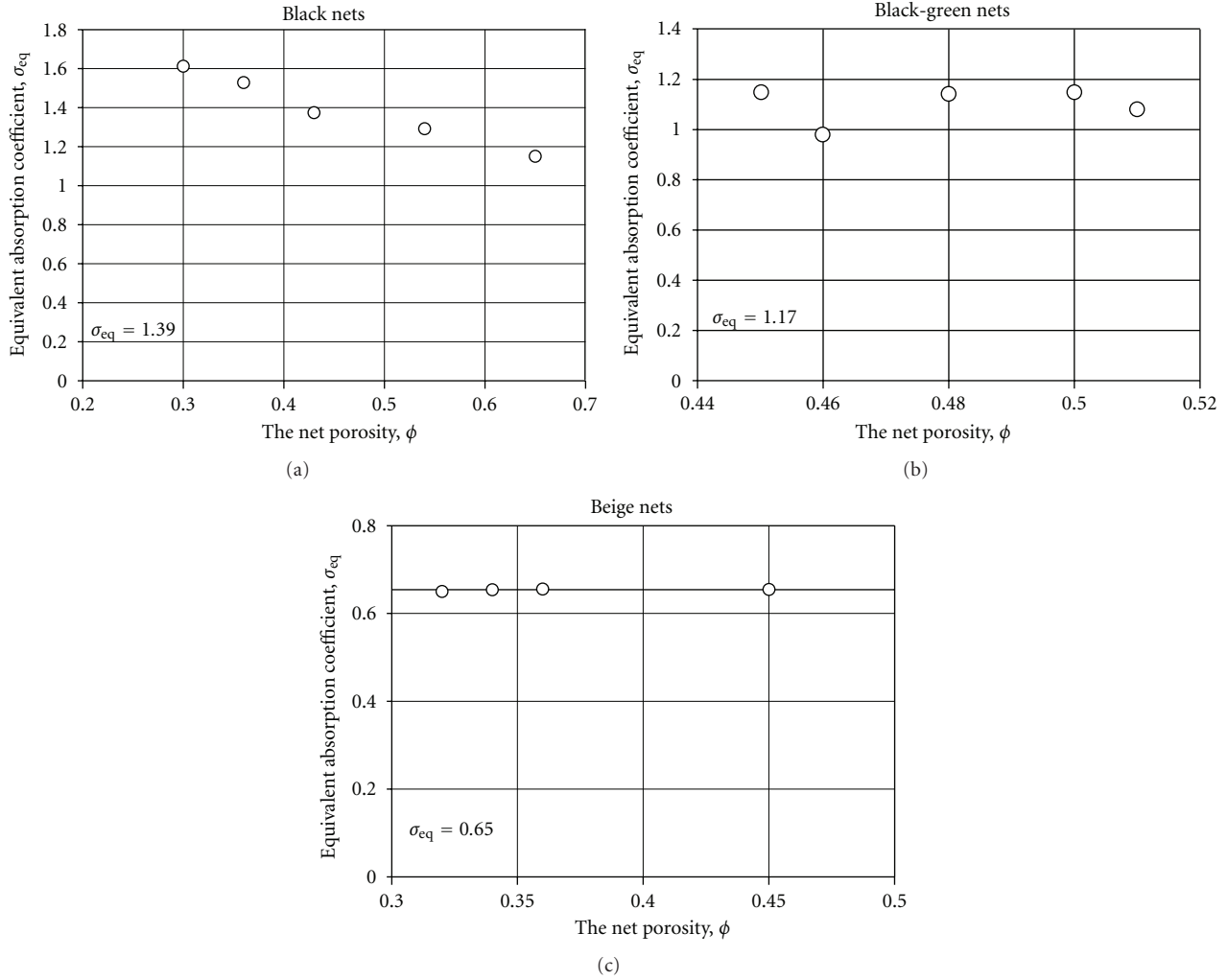
(a)

(b)

(c)

Figure 4: The equivalent absorption coefficient (σ_{eq}) as affected by the porosity of the tested nets: (a) is for the black group, (b) for the black-green group, and (c) for the beige group.

use by the supplier. The components of the direct beam radiation (B_i, B_t, and B_r) were determined as the difference between the global and diffuse radiation components. Thus at normal incidence, the net transmittance to direct beam radiation (τ_r) was estimated as (B_t/B_i) and the net reflectance to direct beam radiation (ρ_r) was estimated as (B_r/B_i).

3. Results and Discussion

For each net sample, the measured values of τ_r and ρ_r at normal incidence were substituted consequently into (2) and (1) to obtain the values of τ^* and ρ^*. Substituting the values of τ^* and ρ^* into (3) and (4) gives the equivalent optical constants (n_{eq} and σ_{eq}) of the selected net. The optical constants of a net did not depend on the direction of the incident beam radiation; therefore they are used to estimate the directional radiative properties of the net. The values of n_{eq} as affected by the net porosities (ϕ) are illustrated in Figures 3(a), 3(b), and 3(c), for the black nets group, the black-green nets group and the beige nets group, respectively.

The data in Figures 3(a), 3(b), and 3(c) show that n_{eq} decreases when ϕ increases and correlations between n_{eq} and ϕ could be obtained with reasonable R^2 values in the following form:

$$n_{eq} = 1.63 - 0.65(\phi), \quad (R^2 = 0.96) \text{ for black nets}, \quad (8)$$

$$n_{eq} = 1.7 - 0.63(\phi), \quad (R^2 = 0.86) \text{ for black-green nets}, \quad (9)$$

$$n_{eq} = 2.97 - 1.98(\phi), \quad (R^2 = 0.81) \text{ for beige nets}. \quad (10)$$

Ideally, if the value of ϕ in (8), (9), and (10) increased to one (no net), then the values of n_{eq} should equal to one (i.e., the refractive index of air). However, there are residuals of +0.02 in (8), −0.07 in (9), and +0.01 in (10) that should be added to n_{eq} estimated form (8)–(10). These equations also show that value of n_{eq} increases with increasing brightness of the net color, which means more reflection is expected. The nets with the brightest color in this study (the beige nets) showed
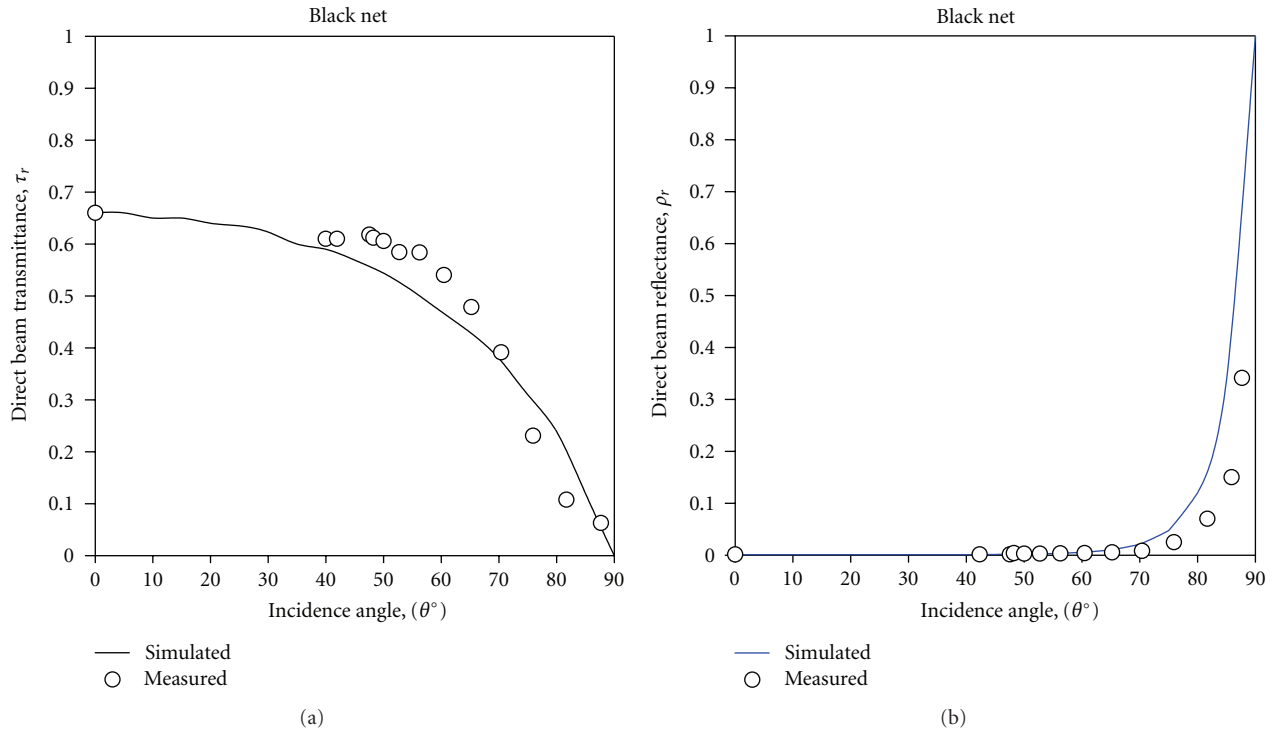
FIGURE 5: Comparison between the measured [8] and simulated values of (a) the direct beam transmittance (τ_r) and (b) the direct beam reflectance (ρ_r) for the black net.

FIGURE 6: Comparison between the measured [8] and simulated values of (a) the direct beam transmittance (τ_r) and (b) the direct beam reflectance (ρ_r) for the beige net.
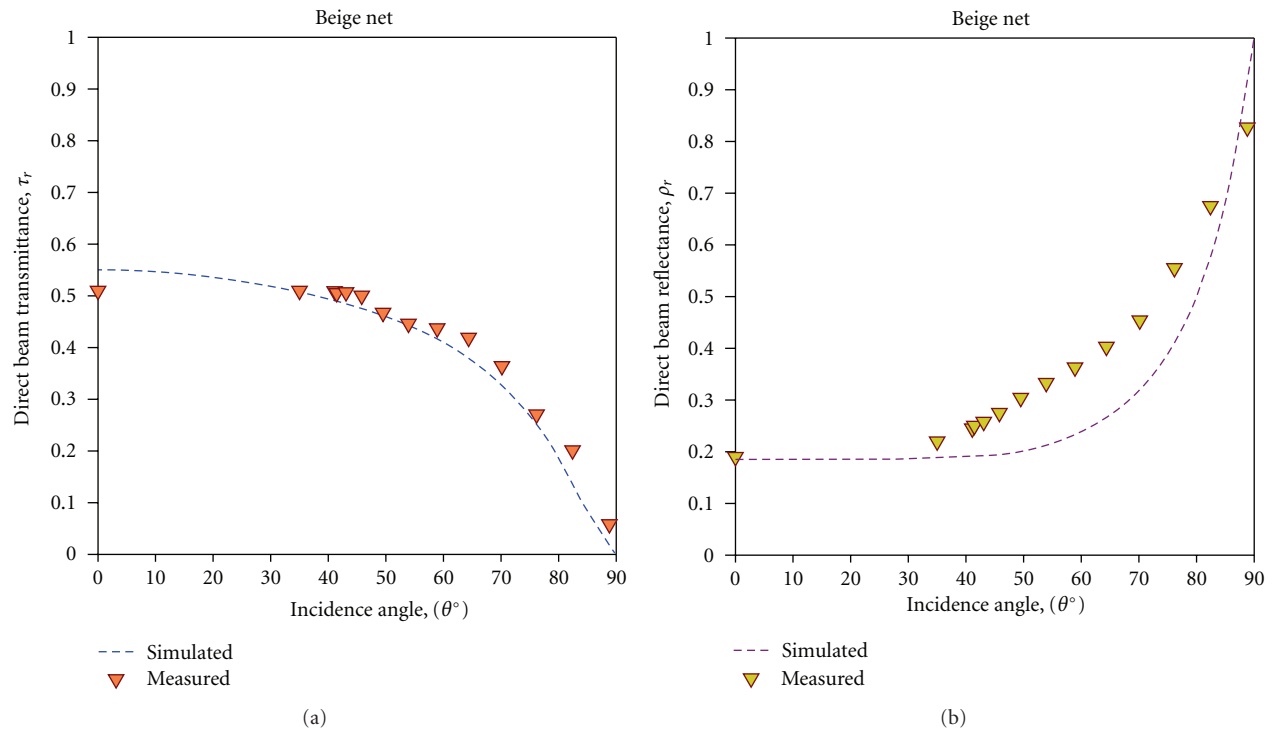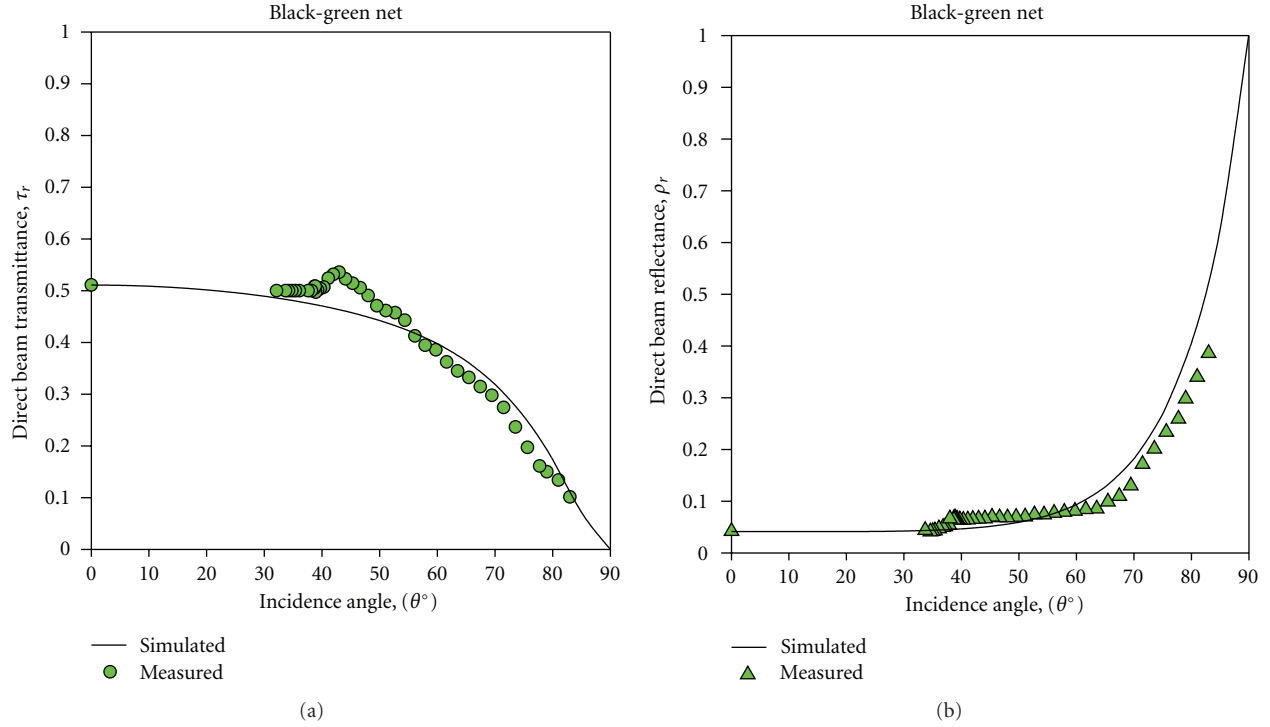
FIGURE 7: Comparison between the measured [8] and simulated values of (a) the direct beam transmittance (τ_r) and (b) direct beam reflectance (ρ_r) for the black-green net.

the highest value of n_{eq} whereas nets with the darkest color (the black nets) showed the lowest n_{eq}.

The effects of the net porosity ϕ on the value of σ_{eq} are illustrated in Figures 4(a), 4(b), and 4(c) for the black group, for the black-green group, and for the beige group, respectively. According to (4) and (6) and in analogy with homogeneous translucent materials, the value of σ_{eq} should be constant for each group of nets. And the value of τ_θ^* in (6) depends on the porosity, ϕ, of the net and on the direction, θ, of the incident beam radiation. The data in Figure 4(c) for the beige nets group satisfy the hypothesis that σ_{eq} is constant for each group of nets. However, the values of σ_{eq} for the black and black-green groups (Figures 4(a) and 4(b)) did not satisfy the hypothesis exactly. This was mainly due to the low number of data points as a result of the low availability of net groups in the local markets. Therefore, an average value for each net group was used.

4. Validation of the Model

The main purpose of the validation is to check the capability of n_{eq} and σ_{eq}, estimated using the present model, to calculate the directional radiative properties of nets under natural solar radiation conditions. In a previous study [8] we measured the direct beam transmittance (τ_r) and reflectance (ρ_r) for a black net ($\phi = 0.65$), for a beige net ($\phi = 0.12$), and for a black-green net ($\phi = 0.47$) at different incident angles (θ) of the direct beam solar radiation. Values of τ_r and ρ_r at normal incidence were measured for the three nets (see Section 2.2). The simulated values of τ_r and ρ_r using the

present model at different θ comparing with the measured values of τ_r and ρ_r are illustrated, respectively, in Figures 5(a) and 5(b) for the black net, in Figures 6(a) and 6(b) for the beige net, and in Figures 7(a) and 7(b) for the black-green net. Reasonable agreement was shown between the simulated and the measured τ_r and ρ_r for the black, beige, and black-green nets.

Figures 5(a), 5(b), 6(a), 6(b), 7(a), and 7(b) do not show measured values of τ_r and ρ_r at low values of incidence angle ($0° < \theta < 33°$) because of the latitude and the time of the year at which the experiments were carried out (the lowest value of θ was estimated to be about 33° at solar noon). In addition, when θ was near or equal to 90°, the beam radiation incident on the thread surfaces reflects downwards. This increased τ_r to a value higher than zero and reduced ρ_r to a value much lower than one.

5. Conclusions

A modeling approach for determining the equivalent optical constants (n_{eq} and σ_{eq}) of plastic nets was described and validated. Three groups of nets (black, beige, and black-green) were tested. For each group, an equation for n_{eq} as a function of the net porosity was derived, and an average value for σ_{eq} was determined. Using values of n_{eq} and σ_{eq}, the directional solar radiative properties of the net can be calculated without the need of measurements which are expensive and time consumed. The resulting properties are equivalent for the whole net as a semitransparent material, not for the net material itself. The present model was

validated by comparing the measured radiative properties of three of the nets, at different incident angle of solar beam radiation, with those calculated using the present model. The calculated radiative properties agreed with the measured values. Further research is needed to investigate n_{eq} and σ_{eq} for other nets communities with different colors (e.g., a blue group, an orange group, a white group, a green group, etc.).

Nomenclature

B_i: Direct beam solar radiation flux incident on the net surface ($W\,m^{-2}$)

B_r: Direct beam solar radiation flux reflected from the net ($W\,m^{-2}$)

B_t: Direct beam solar radiation flux transmitted through the net ($W\,m^{-2}$)

D_i: Diffuse radiation flux incident on the net surface ($W\,m^{-2}$)

D_r: Diffuse radiation flux reflected from the net surface ($W\,m^{-2}$)

D_t: Diffuse radiation flux transmitted through the net ($W\,m^{-2}$)

I_D: The diffuse index (i.e., ratio of diffuse to global solar radiation flux)

n_{eq}: Equivalent refractive index of the net (dimensionless)

S_i: Global solar radiation flux incident on the net surface ($W\,m^{-2}$)

S_r: Global solar radiation flux reflected from the net surface ($W\,m^{-2}$)

S_t: Global solar radiation flux transmitted through the net ($W\,m^{-2}$)

Φ: The net porosity (i.e., the empty area per unit area)

θ: Incident angle of solar beam radiation (degree)

θ_r: Equivalent refracted angle of solar beam radiation (degree)

ρ_g: Reflectance of the net to global solar radiation (dimensionless)

ρ_r: Reflectance of the net to direct beam solar radiation (dimensionless)

ρ^*: Interface reflectance between the net surface and air (dimensionless)

ρ_θ^*: Directional interface reflectance between the net surface and air (dimensionless)

σ_{eq}: Equivalent absorption coefficient of the net (dimensionless)

τ_g: Transmittance of the net to global solar radiation (dimensionless)

τ_r: Transmittance of the net to direct beam solar radiation (dimensionless)

τ^*: Transmittance of the net due to absorption only in the net threads (dimensionless).

Acknowledgments

References

[1] S. Castellano, G. M. Scarascia, G. Russo et al., "Plastic nets in agriculture: a general review of types and applications," *Applied Engineering in Agriculture*, vol. 24, pp. 799–808, 2008.

[2] S. Castellano, G. Russo, and G. Scarascia Mugnozza, "The influence of construction parameters on radiometric performances of agricultural nets," *Acta Horticulturae*, vol. 718, pp. 283–290, 2006.

[3] D. Briassoulis, A. Mistriotis, and D. Eleftherakis, "Mechanical behaviour and properties of agricultural nets—part II: analysis of the performance of the main categories of agricultural nets," *Polymer Testing*, vol. 26, no. 8, pp. 970–984, 2007.

[4] D. Briassoulis, A. Mistriotis, and D. Eleftherakis, "Mechanical behaviour and properties of agricultural nets—part I: testing methods for agricultural nets," *Polymer Testing*, vol. 26, no. 6, pp. 822–832, 2007.

[5] A. M. Abdel-Ghany and I. M. Al-Helal, "Characterization of solar radiation transmission through plastic shading nets," *Solar Energy Materials and Solar Cells*, vol. 94, no. 8, pp. 1371–1378, 2010.

[6] A. M. Abdel-Ghany and I. M. Al-Helal, "Analysis of solar radiation transfer: a method to estimate the porosity of a plastic shading net," *Energy Conversion and Management*, vol. 52, no. 3, pp. 1755–1762, 2011.

[7] S. Hemming, G. L. A. M. Swinkels, S. Castellano, G. Russo, and G. M. Scarascia, "Numerical model to estimate the radiometric performance of net covered structures (AGRONETS)," in *Proceedings of the Agricultural and Biosystems Engineering for a Sustainable World (AgEng '08)*, Crete, Greece, June 2008.

[8] I. M. Al-Helal and A. M. Abdel-Ghany, "Measuring and evaluating solar radiative properties of plastic shading nets," *Solar Energy Materials and Solar Cells*, vol. 95, no. 2, pp. 677–683, 2011.

[9] I. M. Al-Helal and A. M. Abdel-Ghany, "Responses of plastic shading nets to global and diffuse PAR transfer: optical properties and evaluation," *Wageningen Journal of Life Sciences*, vol. 57, no. 2, pp. 125–132, 2010.

[10] A. M. Abdel-Ghany, T. Kozai, and C. Chun, "Evaluation of selected greenhouse covers for use in regions with a hot climate," *Japanese Journal of Tropical Agriculture*, vol. 45, pp. 242–250, 2001.

[11] L. He, T. H. Short, and X. Yang, "Solar radiation transmittance of a double-walled acrylic pellet-insulated greenhouse," *Transactions of the American Society of Agricultural Engineers*, vol. 34, no. 6, pp. 2559–2563, 1991.

[12] J. A. Duffie and W. A. Beckman, *Solar Engineering of Thermal Processes*, John Wiley & Sons, New York, NY, USA, 2nd edition, 1991.

[13] M. M. Elsayed, I. S. Taha, and J. A. Sabbagh, *Design of Solar Thermal Systems*, Scientific Publishing Center, King Abdulaziz University, Jeddah, Saudi Arabia, 1st edition, 1994.

[14] S. S. Soulayman, Z. Nassif, and A. Harfoush, "Transmittance, reflectance and absorptance of multi-plate planar window," *Renewable Energy*, vol. 1, no. 2, pp. 211–217, 1991.

[15] A. M. Abdel-Ghany, T. Kozai, C. Kubota, and I. S. Taha, "Investigation of the spectral optical properties of the liquid radiation filters for using in the greenhouse application," *Japan Journal of Agriculture Meteorology*, vol. 57, pp. 11–19, 2001.

Research Article

Experimental Study on Solar Cooling Tube Using Thermal/Vacuum Emptying Method

Huizhong Zhao,[1, 2] Haibin Liang,[2] Wenzhe Sun,[1] Guoqing Yu,[2] Dan Cao,[1] and Jun Ji[1]

[1] *Merchant Marine College, Shanghai Maritime University, Shanghai 201306, China*
[2] *School of Environment and Architecture, University of Shanghai for Science and Technology, Shanghai 200093, China*

Correspondence should be addressed to Huizhong Zhao, hzzhao@shmtu.edu.cn

A solar cooling tube using thermal/vacuum emptying method was experimentally studied in this paper. The coefficient of performance (COP) of the solar cooling tube was mostly affected by the vacuum degree of the system. In past research, the thermal vacuum method, using an electric oven and iodine-tungsten lamp to heat up the adsorbent bed and H_2O vapor to expel the air from the solar cooling tube, was used to manufacture solar cooling tubes. This paper presents a novel thermal vacuum combined with vacuum pump method allowing an increased vacuum state for producing solar cooling tubes. The following conclusions are reached: the adsorbent bed temperature of solar cooling tube could reaches up to 233°C, and this temperature is sufficient to meet desorption demand; the refrigerator power of a single solar cooling tube varies from 1 W to 12 W; the total supply refrigerating capacity is about 287 kJ; and the COP of this solar cooling tube is about 0.215.

1. Introduction

With the improvement of people's living standard, the demand for air conditioner is increasing. Use of CFCs for refrigeration compression has global warming potential (GWP) and ozone depletion potential (ODP), so their use should be minimized. The energy problem has become a major problem facing human development, and has led to efforts to reduce fossil fuel usage. Solar energy, one of the most abundant resources, has many advantages, most importantly that it is environmentally friendly. This has led to attention from the worldwide research community. Adsorption refrigeration uses nature working pairs as refrigerants and solar energy as a heat resource, so it consumes no fossil fuels during refrigeration process and is environment-friendly.

Ferreira Leite et al. [1] presented the characterization and the pre-dimensioning of an adsorption chiller as part of a 20 kW air conditioning central unit for cooling a set of rooms that comprises an area of 110 m². The adsorption chiller's expected coefficient of performance (COP) was found to be around 0.6. Khattab [2] presented the description and

operation of a simple structure, low cost solar-powered adsorption refrigeration module. Test results showed that a module using bed technique Type 4 and reflector arrangement Type C provided the best performance. Wang et al. [3, 4] used a compound adsorbent of $CaCl_2$ and activated carbon as working pairs and to produce an ice-making test unit for fishing boats. At evaporating temperatures of −35°C and −25°C, the cooling powers are 0.89 and 1.18 kW respectively. Clausse [5] explored the possibility to perform heating and air-conditioning of a state-of-the-art building located near Paris in France. For air-conditioning, thermal comfort was achieved as indoor temperature was kept below 25°C during five consecutive hot days. Anyanwu et al. [6, 7] made a solid adsorption refrigerator, achieving a chilled water temperature around 1°C, suitable for drug, fruits, and vegetables preservation. Khattab [2, 8, 9] set up a solar-powered adsorption module, this module produced ice 6.9 kg/m² and the net solar COP is 0.136. Guilleminot et al. [10–12] presented experimental study on solar adsorptive ice maker and Heat transfer intensification in the adsorbent bed, and the results show the great improvement in the thermal transfer quality using new consolidated materials.
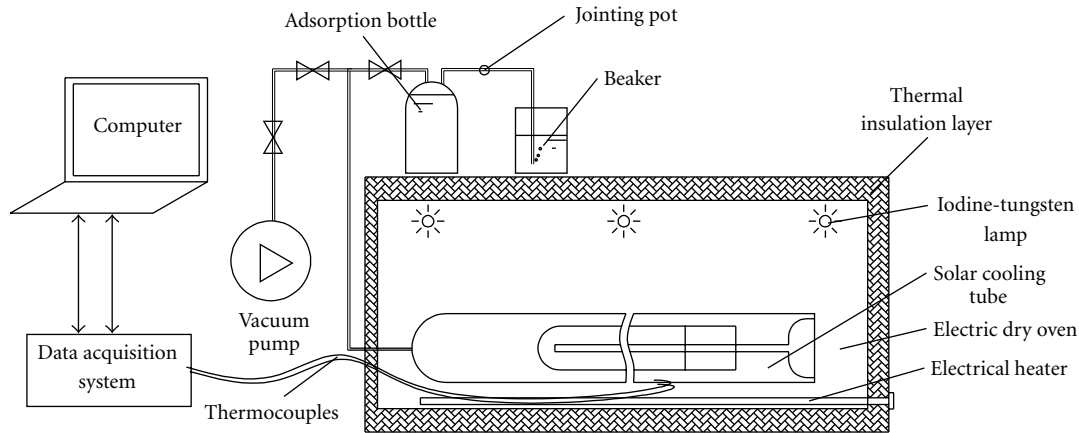
FIGURE 1: Sketch of manufacturing solar cooling tube by means of thermal/vacuum method.

Compared with the above refrigeration system, a solar cooling tube can accomplish the refrigeration cycle in one glass tube. The solar cooling tube [13] and freeze-proof solar cooling tube [14] which uses zeolite/water or active carbon/methanol as working pairs were designed and built. In the past research, the solar cooling tube was manufactured using the thermal vacuum method, which using electric oven and iodine-tungsten lamp to heat up the adsorbent bed, and using H_2O vapor to expel the air of the solar cooling tube and to reduce air partial pressure. This paper presents a novel thermal vacuum combined with vacuum pump method for producing solar cooling tube, resulting in a highly increased vacuum state.

FIGURE 2: Photograph of manufacturing solar cooling tube.

2. Manufacture of the Solar Cooling Tube

The manufacturing process of solar cooling tube is mainly composed of three steps: (1) the preparation filling process; (2) preliminary drying of the solar cooling tube; (3) operating vacuum state by means of thermal/vacuum method. The steps are as follows.

First, the 13X zeolite is activated in the 325°C oven for 8 hours, and then an appropriate amount of highly pure sodium silicate and pure water is added to prepare the adsorption compound. The resulting adsorbent compound has better thermal conductivity and formability than 13X powder [15]. An electric mixer is used to stir the mixture until it becomes liquid state. A funnel is used to fill the confected the compound adsorbent into all-glass tubular solar collector and preliminary dries it by iodine-tungsten lamp.

Second, put the all-glass tubular solar collector filled with the compound adsorbent into a high borosilicate glass and welding pipe using glass welding lathe, then the semifinished solar cooling tube was made.

Third, 200 mL pure water is placed into the semi-finished solar cooling tube. The tube is then placed into an electric dry oven, and welding the solar cooling tube with adsorption bottle, jointing pot beaker and vacuum pump. Figure 1 shows a diagram of the system, and Figure 2 is a photograph of the production equipment. After several hours discharging the air in the solar cooling tube using the thermal emptying method, a vacuum pump is used to evacuate the solar cooling tube. Finally, welding the tail joint completes manufacture of the solar cooling tube.

3. Principle of Solar Cooling Tube

The structure of the solar cooling tube is shown in Figure 3. The solar cooling tube contains these major components: solar collector, adsorbent bed, condenser, inner tube, and evaporator. The solar collector, condenser, inner tube, and evaporator are made of hard borosilicate glass. Using 13X zeolite, the temperature difference between daytime and nighttime corresponds to the adsorption capability difference of refrigerant water; hence, the solar cooling tube achieves refrigeration cycle. The process goes as follows.

During the daytime, the adsorbent bed receives sunlight, and the adsorbent bed temperature rises up to the desorption temperature. When the water vapor flows from adsorbent and raises the water vapor pressure up to the condensing pressure, the desorbed water vapor, which desorbed from adsorbent bed, is condensed in the condenser and flows into the evaporator because of gravity. The water vapor is condensed in the inner wall of the whole outer tube and extracts heat from the environment. In the daytime, the inner

Inner tube

Filtration net

Outer evacuated tube

Inner evacuated tube

Condensor

Adsorbent bed
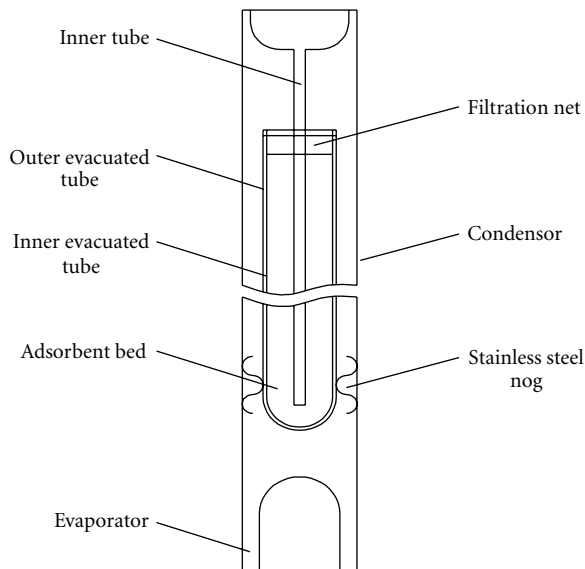
Stainless steel nog

Evaporator

FIGURE 3: Sketch of the solar cooling tube.

tube is full of air and can reduce the thermal loss of adsorbent bed, so the adsorbent bed has higher temperature for desorption. In the whole day, the solar cooling tube receives solar radiation while the water steam continues desorbing from the adsorbent bed and is stored the evaporator. During the nighttime, the adsorbent bed temperature drops after sunset and the inner tube is full with water. This enhances heat transfer for cooling down the adsorbent bed and obtaining heating water. When the adsorbent bed temperature drops to adsorption temperature, the adsorption bed begins to adsorb water vapour and induces a decrease in water vapour pressure, causing the liquid water in the evaporator to vaporize. When the evaporating temperature has lowered enough, the system can provide cooling to the outside. In the adsorption process, the refrigerant water continues to vaporize to supply cooling capacity to the outside; the adsorption refrigeration will continue for the whole night until the next morning.

4. Experiment Setup

The sketch and photograph of the experiment in solar cooling tube was shown in Figures 4 and 5. The main apparatus used for this experiment are as followes: 2700 Multimeter/Data Acquisition system of Keithley Co., was used for collecting the data of temperature measurement, T-type thermocouples and K-type thermocouples are the temperature sensors for lower temperature and higher temperature testing, respectively, the model TRM-123 temperature and radiation instrument produced by Jinzhou was used for testing the solar radiation density, and the model RYQ-1 automatic surface meteorological station was used for measuring the environmental temperature and air relatives humidity.

Temperature and solar radiation were measured at five-minute intervals and could be accessed instantaneously on the computer.

5. Results and Discussion

5.1. The Variation of Solar Radiation and Ambient Temperature. During the experimental period, the weather was sunny and little cloudy. The solar radiation and ambient temperature variation was shown in Figure 6. The solar radiation value is about $20.1 \, \text{MJ} \cdot \text{m}^{-2}$. The maximum solar radiation density is about $800 \, \text{W} \cdot \text{m}^{-2}$ at time 11:45 AM. The ambient temperatures were measured by T-type thermocouples in this experiment. The maximum and the minimum ambient temperature were about $33.8°C$ and $19.4°C$ respectively. The average ambient temperature was $25.9°C$.

5.2. The Adsorbent Bed Temperature Variation. The adsorbent bed temperature variation of solar cooling tube was shown in Figure 7. In the daytime, the adsorbent bed received solar energy and the adsorbent temperature rose up rapidly to $233°C$. This temperature met with desorption demand and the refrigerant water was desorbed from the 13X zeolite adsorbent bed. The steam released the latent heat during condensation and became liquid, before being stored in the evaporator due to gravity. Throughout the day, the solar cooling tube received solar radiation while the refrigerant water steam continued desorbing from the adsorbent bed until the solar radiation was too weak for desorption. At night, the adsorbent temperature dropped and began to adsorb the water steam. In the adsorption process, the adsorbent bed temperature cooled down to a minimum temperature of about $33°C$. The temperature difference between adsorbent bed and ambient temperature was about $14°C$.

5.3. Condensation Temperature Variation. The condensation temperatures of the solar cooling tube were tested at this experiment. Two temperature test points were set on the outside of the condenser. In the desorption process during daylight, the refrigerant water vapor, which desorbed from the adsorbent bed at high temperature, was condensed in the condenser. The variation of the condensation temperature of the solar cooling tube can be seen in Figure 8. The temperature of condenser varied from $31.6°C$ to about $40.5°C$. The maximum and average temperature difference between condenser and ambient temperature was about $13.8°C$ and $9.7°C$, respectively.

5.4. Evaporation Temperature Variation. Two temperature test points were set on the outside of the evaporator. In the adsorption process at nighttime, the adsorbent bed adsorbs the refrigerant gas and keeps the evaporator liquid water evaporating and supply cooling mass to the outside. The variation of the evaporator temperature of the solar cooling tube can be seen in Figure 9. The temperature of evaporator mainly varied from $15°C$ to about $10°C$ and the minimum evaporator temperature is about $9.2°C$.
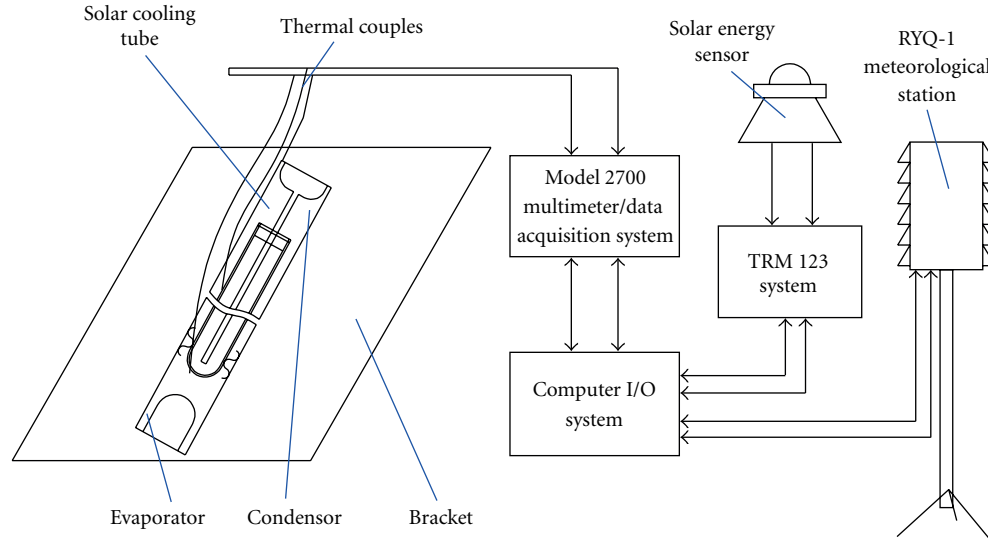
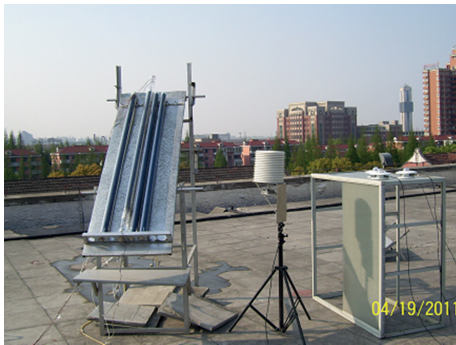FIGURE 4: The experiment of solar cooling tube performance.

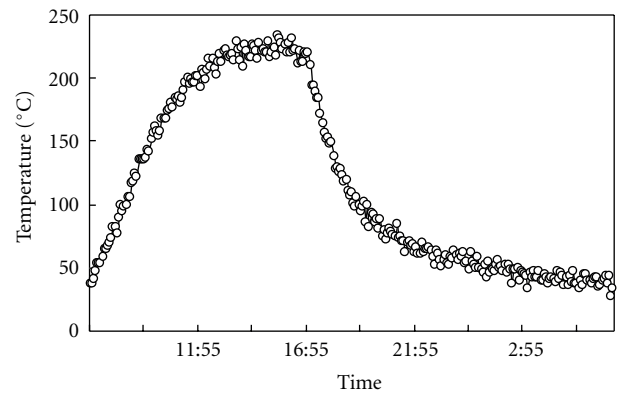FIGURE 5: The photograph of the experiment.

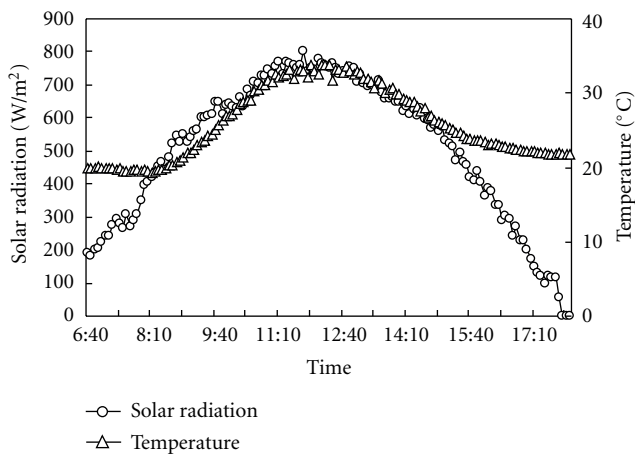FIGURE 7: The adsorbent bed temperature variation of the solar cooling tube.

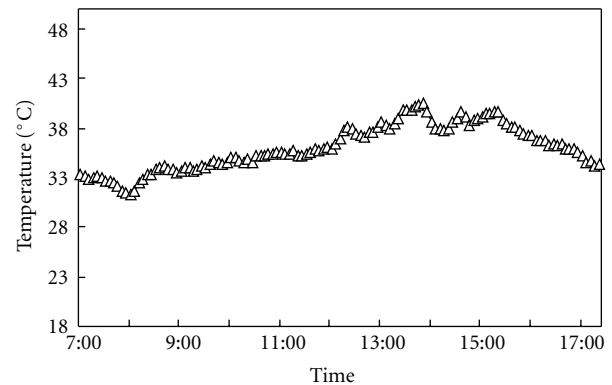FIGURE 6: Solar radiation and ambient temperature variation.

FIGURE 8: The condensation temperature variation.

5.5. Desorption Capacity Variation. The desorption capacity variation of the solar cooling tube can be seen in **Figure 10**. During the daytime, the adsorbent bed temperature rose as solar energy was received. The refrigerant water gas was desorbed from the adsorbent bed and stored in the evaporator. Desorption capacity was measured by the quantity of the refrigerant water. From 9 : 00 to 12 : 00, the speed of
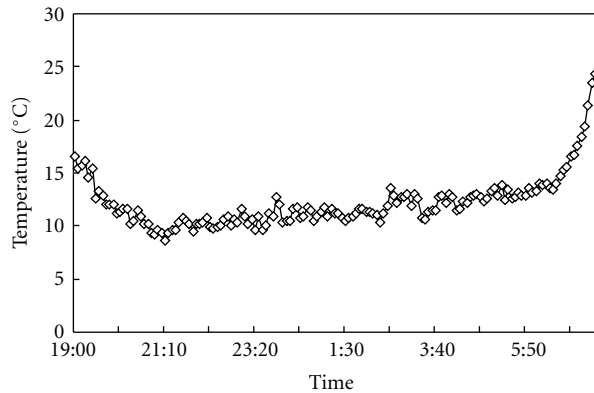
FIGURE 9: The evaporation temperature variation.

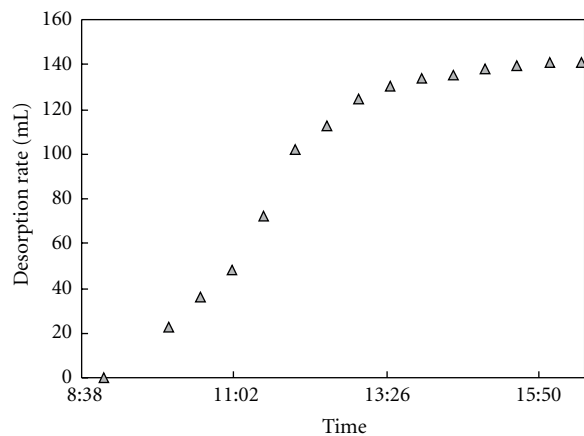FIGURE 11: The refrigerator power of a single solar cooling tube.

FIGURE 10: The desorption capacity variation of the solar cooling tube.

desorption was higher and was slow down after 13:00. The total desorption capacity was about 140 g.

5.6. Evaporative Refrigeration Capacity of a Single Solar Cooling Tube. The refrigerator power variation of a single solar cooling tube can be seen in Figure 11. In the adsorption process at nighttime, the adsorbent bed adsorbed the refrigerant gas and keeps the evaporator liquid water evaporating supply cooling mass to the outside. The refrigerator power of a single solar cooling tube varied from 12 W at about 20:00°C and weakened to less than 1 W by the following morning. The total supply refrigerating capacity was about 287 kJ and the COP of this solar cooling tube was about 0.215.

6. Conclusions

This paper focused on an experimental study of a solar cooling tube using a thermal/vacuum emptying method. The solar cooling tube uses solar energy as a heating resource to complete the adsorption cycle, reducing damage to the environment compared to common alternatives. The performance of solar cooling tube was experimentally studied in this research and the following conclusions can be drawn:
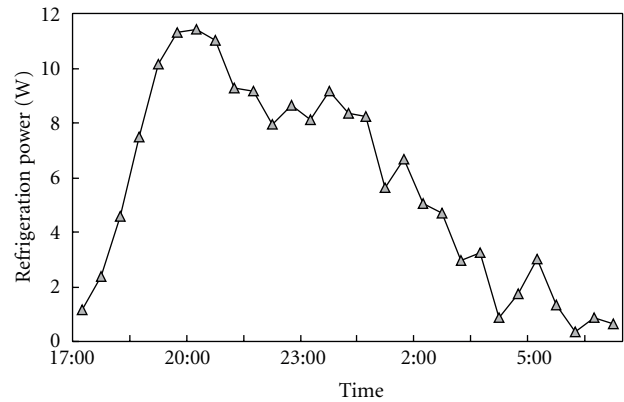
(1) When ambient temperature is about 19.4°C–33.8°C, and the solar radiation is about $20.1 \, MJ \cdot d^{-1} \, m^{-2}$, the adsorbent bed temperature of solar cooling tube reaches up to 233°C. This temperature canmeet desorption demand.

(2) At the nighttime, the adsorbent bed temperature of the solar cooling tube cooled down to the minimum temperature about 33°C and this temperature can meet adsorption demand. The temperature difference between adsorbent bed and ambient temperature is about 14°C.

(3) The refrigerator power of a single solar cooling tube varied from 12 W to 1 W. The total supply refrigerating capacity is about 287 kJ and the COP of this solar cooling tube is about 0.215.

Acknowledgments

References

[1] A. P. Ferreira Leite, F. A. Belo, M. M. Martins, and D. B. Riffel, "Central air conditioning based on adsorption and solar energy," *Applied Thermal Engineering*, vol. 31, no. 1, pp. 50–58, 2011.

[2] N. M. Khattab, "A novel solar-powered adsorption refrigeration module," *Applied Thermal Engineering*, vol. 24, no. 17-18, pp. 2747–2760, 2004.

[3] L. W. Wang, R. Z. Wang, Z. S. Lu, Y. X. Xu, and J. Y. Wu, "Split heat pipe type compound adsorption ice making test unit for fishing boats," *International Journal of Refrigeration*, vol. 29, no. 3, pp. 456–468, 2006.

[4] L. W. Wang, R. Z. Wang, Z. S. Lu, and C. J. Chen, "Studies on split heat pipe type adsorption ice-making test unit for fishing boats: choice of heat pipe medium and experiments under unsteady heating sources," *Energy Conversion and Management*, vol. 47, no. 15-16, pp. 2081–2091, 2006.

 [5] M. Clausse, K. C. A. Alam, and F. Meunier, "Residential air conditioning and heating by means of enhanced solar collectors coupled to an adsorption system," *Solar Energy*, vol. 82, no. 10, pp. 885–892, 2008.

 [6] E. E. Anyanwu and N. V. Ogueke, "Thermodynamic design procedure for solid adsorption solar refrigerator," *Renewable Energy*, vol. 30, no. 1, pp. 81–96, 2005.

 [7] E. E. Anyanwu, U. U. Oteh, and N. V. Ogueke, "Simulation of a solid adsorption solar refrigerator using activated carbon/methanol adsorbent/refrigerant pair," *Energy Conversion and Management*, vol. 42, no. 7, pp. 899–915, 2001.

 [8] N. M. Khattab, H. Sharawy, and M. Helmy, "Development of novel solar adsorption cooling tube," *Energy Procedia*, vol. 18, pp. 709–714, 2012.

 [9] N. M. Khattab, "Simulation and optimization of a novel solar-powered adsorption refrigeration module," *Solar Energy*, vol. 80, no. 7, pp. 823–833, 2006.

[10] J. J. Guilleminot, A. Choisier, J. B. Chalfen, S. Nicolas, and J. L. Reymoney, "Heat transfer intensification in fixed bed adsorbers," *Heat Recovery Systems and CHP*, vol. 13, no. 4, pp. 297–300, 1993.

[11] A. Boubakri, J. J. Guilleminot, and F. Meunier, "Adsorptive solar powered ice maker: experiments and model," *Solar Energy*, vol. 69, no. 3, pp. 249–263, 2000.

[12] F. Bentayeb, F. Lemmini, and J. J. Guilleminot, "Adaptation of an adsorptive solar refrigerator to Moroccan climates," *Renewable Energy*, vol. 6, no. 7, pp. 867–882, 1995.

[13] Z. Liu, Y. Lu, and J. Zhao, "Zeolite-active carbon compound adsorbent and its use in adsorption solar cooling tube," *Solar Energy Materials and Solar Cells*, vol. 52, no. 1-2, pp. 45–53, 1998.

[14] H. Zhao, M. Zhang, L. Zhenyan, L. Yanling, and M. Xiaodong, "Mechanical and experimental study on freeze proof solar powered adsorption cooling tube using active carbon/methanol working pair," *Energy Conversion and Management*, vol. 49, no. 8, pp. 2434–2438, 2008.

[15] H. Zhao, M. Zhang, J. Lv, G. Yu, and Z. Zou, "Thermal conductivities study of new types of compound adsorbents used in solar adsorption refrigeration," *Energy Conversion and Management*, vol. 50, no. 5, pp. 1244–1248, 2009.

Research Article

Treatment of Color Filter Wastewater by Fresnel Lens Enhanced Solar Photo-Fenton Process

Wen-shiuh Kuo and Chia-ling Wu

Department of Safety, Health, and Environmental Engineering, National United University, Miao-Li 36063, Taiwan

Correspondence should be addressed to Wen-shiuh Kuo, wsk@nuu.edu.tw

Treatment of color filter wastewater using solar photo-Fenton process enhanced by high-concentrating Fresnel lens was investigated in this paper. Optimal reaction conditions based on response surface methodology (RSM) were established as under an initial pH of 5, a $[H_2O_2]_0/COD_0$ ratio of 1~1.35 and a $[H_2O_2]_0/[Fe^{2+}]_0$ ratio of 15 for a reaction time of 60 min, which could reach a readily biodegradable level, that is, the biodegradability (BOD_5/COD) of wastewater was more than 0.3. With the assistance of Fresnel lens, the solar photo-Fenton process increased the COD degradation rate and mineralization rate by a factor of 4.5 and 6.5, respectively. In addition, the microtoxicity (TU_{50}) of wastewater was almost diminished after a 60 min of treatment, whereas the microtoxicity of treated wastewater without the assistance of Fresnel lens remained a TU_{50} value of 1.166. This could be mainly due to the concentrating effect of Fresnel lens for solar energy, resulting in an increase of 2~3 times of solar light intensity and a raising heat irradiation in terms of 15~30 °C of wastewater temperature. These results revealed that solar energy could be concentrated effectively by using Fresnel lens and showed a significant promoting effect on the photo-Fenton reaction for treating color filter wastewater.

1. Introduction

Organic wastewater from color filter industry generally contains so many residuals such as TMAH ($C_4H_{13}NO$), PGMEA ($C_6H_{12}O_3$), acrylic resin, and pigments, and it is variable in composition and strength at different stages of process. The effluent is usually characterized by its high chemical oxygen demand (COD), low biodegradability (BOD_5/COD), and with microtoxicity, implying the presence of refractory organic matter. Therefore, biological treatment processes are susceptible for treatment of color filter wastewater. Instead, activated carbon adsorption or coagulation is commonly used. However, new environmental laws may consider the spent adsorbents or sludge as hazardous waste and require further treatment. Consequently, intensive research for novel technologies with higher efficiency and less amount of waste generated has been stimulated. For that reason, advanced oxidation processes (AOPs) have been previously described as a promising option to remove persistent pollutants from contaminated water [1] when conventional water treatment

processes are not efficient enough. AOPs are able to produce a highly reactive, nonspecific oxidant, mainly hydroxyl radicals ($^{\bullet}OH$). The hydroxyl radical possesses inherent properties that enable it to attack refractory organic pollutants in water to achieve a complete mineralization. However, the production of photons with artificial light sources requires significant electrical energy demand and UV lamp consumption, leading in a high operation cost in AOPs [2].

Alternatively, solar energy is essentially unlimited and its utilization is ecologically benign. In the wastewater treatment sector, solar technology has been extensively used as alternative to UV lamps to reduce the operation cost in AOPs [3]. In particular, photo-Fenton process using solar irradiation has been used as an economically viable process and has attracted great interest in recent years [4]. However, solar photo-Fenton process was usually carried out by using solar irradiation directly, resulting in a lower absorption and utilization of solar energy [5]. To improve the efficiency of solar photo-Fenton process, it is necessary to maximize the absorption of solar energy.

TABLE 1: Characteristics of color filter wastewater.

Item	Range
pH	10.4~10.7
UV_{254}	2.000~2.046
COD, mg/L	1674~1766
BOD_5, mg/L	152~230
BOD_5/COD	0.08~0.13
TOC, mg/L	405~430
SS, mg/L	2.4~3.0
TS, mg/L	1145~1440
Color (ADMI value)	1100~1400

TABLE 2: Experimental range and levels of the process independent variables in this study.

Independent variable	Factor	Range and level		
		−1	0	+1
Initial pH	X_1	3	4	5
g H_2O_2/g COD	X_2	1.0	1.5	2.0
$[H_2O_2]_0/[Fe^{+2}]_0$	X_3	5	10	15

In this study, the degradation and mineralization of color filter wastewater using solar photo-Fenton process enhanced by high-concentrating Fresnel lens was investigated. This lens is made of PMMA plastic materials. Response surface methodology (RSM) was employed to obtain the optimal reaction conditions of critical process parameters (initial pH of wastewater, $[H_2O_2]_0/COD_0$ and $[H_2O_2]_0/[Fe^{2+}]_0$) to reach a readily biodegradable degree of color filter wastewater. Moreover, the effect of Fresnel lens on treatment performance in terms of COD degradation efficiency, mineralization efficiency, biodegradability, and microtoxicity of color filter wastewater was examined.

2. Materials and Methods

2.1. Materials. The color filter wastewater used in this study was obtained from an electrooptical industry plant located in Hsin-Chu, Taiwan. The characteristics of color filter waster are shown in Table 1. Basically, the color filter wastewater has the properties of high COD, low biodegradability, and with microtoxicity. Hydrogen peroxide (H_2O_2) with a concentration of 35% was supplied by Panreac Co., EU. $FeSO_4 \cdot 7H_2O$ (Panreac Co., EU) with a purity of 99% was used as a source of ferrous ion. All other chemicals used in this study were analytical grade and used as received.

2.2. Procedures. All experiments were carried out in a batch mode. A 1-L glass beaker containing 200 mL of color filter wastewater was used and maintained at a preset temperature in a water bath during the experiments. A 3-factor *3-level RSM experimental design with three replicates at center point as shown in Table 2 was applied. The color filter wastewater was placed into the photoreactor and irradiated by artificial solar light with an intensity of 500 W/m² by using an ATLAS Suntest CPS+ solar simulator (ATLAS Co., USA). During the experiments, the pH of the solution was monitored using a pH meter (SP-701LI 120, Suntex Co., Taiwan) equipped with a glass electrode. Samples were withdrawn from the reactor at a reaction time of 60 min, tested for H_2O_2 consumption according to the method reported by Seller [6] and iron as Fe^{2+} ion determined by Fe(II)/1,10-phenanthroline complex at 510 nm [7] using a Hitachi (Japan) U-2001 spectrophotometer instantly, and then quenched with sodium hydrogen sulfite to avoid further

reactions. The remaining samples were then stored at 4°C for the following ADMI, COD, TOC, BOD_5, and microtoxicity analysis.

As the optimal values of the process parameters were developed on the basis of RSM application and related equations, a Fresnel lens that was made of PMMA (thickness: 2 mm, pitch: 0.5 mm, facet depth: 0.2 mm, Fresnel circles: 395) was added into solar photo-Fenton system with a distance of 16 cm above the level of wastewater. To investigate the effect of Fresnel lens, a similar reactor without Fresnel lens was also performed under the same actual solar irradiation. A schematic diagram of the photoreactor using Fresnel lens is shown in Figure 1.

2.3. Analytical Methods

2.3.1. Color Measurement of Color Filter Wastewater. A DR 4000 spectrophotometer (HACH Co., USA) was used for color measurement in terms of ADMI (American Dye Manufacturers Institute) values. The decolorization efficiency was calculated on the basis of ADMI reduction in color filter wastewater.

2.3.2. COD and TOC Measurement. COD (Chemical Oxygen Demand) of wastewater was carried out via a DR 4000 photometer (HACH Co., USA) by using a $K_2Cr_2O_7$ reagent. TOC (Total Organic Carbon) of wastewater was measured by a Shimadzu VCPH analyzer (Shimadzu Co., Japan).

2.3.3. BOD_5 Measurement. BOD_5 test was measured according to the procedures described in Standard methods [7] Section 5210D. The bacteria (2000~4000 mgMLSS/L) used in this test were obtained from local activation sludge system, operating at industrial wastewater treatment plant. The data showed that the BOD_5 value of untreated color filter wastewater in this study was 0.08~0.13, indicating that the color filter wastewater was not readily biodegradable.

2.3.4. Microtoxicity Measurement. The microtoxicity of each sample was measured using an SDI M500 (SDI Co., USA) analyzer. Microtoxicity is expressed as EC_{50} (5 min, 15°C), which was defined as the effective concentration of solution for a 50% reduction of the luminescence of the bacterium *Photobacterium phosphoreum*. A lower EC_{50} value indicates a higher amount of toxic constituent presented in the pollutant solution. The EC_{50} values are expressed as percentage (% v/v) of the sample [8, 9]. In addition, EC_{50} values could be transformed to toxicity units (TU_{50}), which was equal to
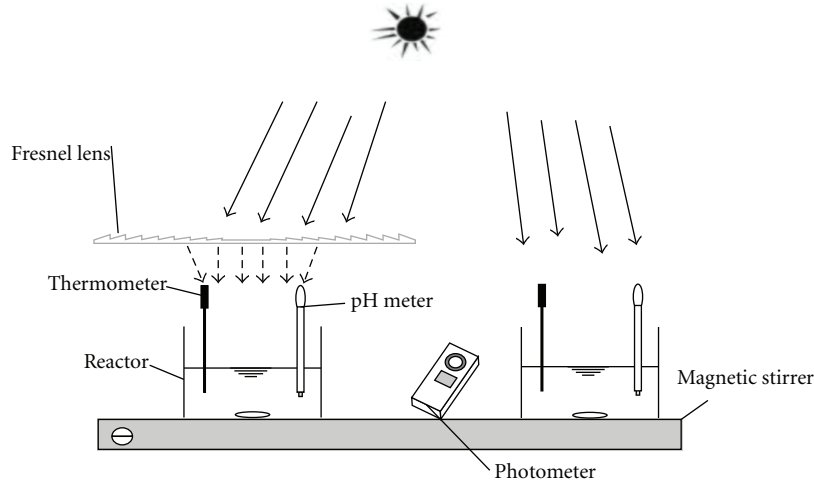
FIGURE 1: Schematic diagram of the solar photoreactor with and without Fresnel lens.

$1/EC_{50}$. The EC_{50} of color filter wastewater was measured, and it was 76~78%. Toxicity Unit (TU_{50}) was, therefore, in the range of 1.25~1.30 for color filter wastewater. In this study, the TU_{50} value was used to trace the change in toxicity of color filter wastewater due to solar photo-Fenton treatment.

3. Results and Discussion

3.1. Optimization of Solar Photo-Fenton Treatment of Color Filter Wastewater. On the basis of RSM application, the empirical relationship between the biodegradability of color filter wastewater (Y) and independent variables studied are shown as follows:

$$Y_{BOD_5/COD}$$
$$= 0.4770 + 0.0066X_1 + 0.0968X_2 - 0.1251X_3$$
$$- 0.0374X_1^2 - 0.0291X_2^2 - 0.0084X_3^2 - 0.0795X_1X_2$$
$$- 0.0628X_2X_3 - 0.0565X_2X_3,$$
$$r^2 = 0.904.$$
$$(1)$$

The regression model (1) had a high value of coefficient of determination ($r^2 > 0.90$). This implies that the process efficiency could be predicted properly by the polynomial regression equations under the conditions studied. Based on the model equation, the optimal values of the process parameters were established as under a pH of 5, a $[H_2O_2]_0/COD_0$ ratio of 1~1.35, and a $[H_2O_2]_0/[Fe^{2+}]_0$ ratio of 15 for a reaction time of 60 min, which could reach a readily biodegradable level, that is, the biodegradability (BOD_5/COD) of wastewater was more than 0.3. In order to confirm the optimum conditions, five replicates and t-test analysis were performed. The results showed that the average of BOD_5/COD was 0.306 and the 95% of confidence intervals for BOD_5/COD was 0.290~0.322. Consequently, the credibility of the optimum conditions obtained in this study was acceptable.

3.2. Effect of Fresnel Lens on the Degradation Efficiency of Wastewater. Basically, it was found that the concentrating effect of Fresnel lens for solar energy could result in an increase 2~3 times of solar light irradiation and a raising heat irradiation in terms of 15~30°C of wastewater temperature in this study. Figure 1 showed the effect of Fresnel lens on COD and TOC degradation efficiency of color filter wastewater. As shown in Figure 2, an 85% of COD and a 70% of TOC degradation of color filter wastewater were achieved with the assistance of Fresnel lens, in contrast to a 48% of COD and a 32% of TOC degradation in solar photo-Fenton process with a solar irradiation of 1,000 W/m² was observed within 60 min. The decolorization efficiency of color filter wastewater also increased 17% as using Fresnel lens. Moreover, it was found that the degradation efficiency of color filter wastewater with the use of Fresnel lens at a reaction time of 30 min was higher than that without the assistance of Fresnel lens at a reaction time of 60 min. This could be due to a higher light irradiation and because water temperature increased the reaction rate between hydrogen peroxide and any form of ferrous/ferric ion, thus increased the rate of generation of oxidizing species such as $^{\bullet}OH$ radical [10]. A similar phenomenon was also found in the study of Will et al. [11]. Its result indicated that the TOC degradation efficiency of phenol wastewater was 45% and 55% for a solar irradiation of 450 W/m² and 750 W/m², respectively. In addition, the study's results of Rodriguez et al. [12] showed that the degradation efficiency of textile wastewater increased while the temperature of water was improved obviously from 30°C to 60°C in photo-Fenton process.

To quantitatively analyze the effect of Fresnel lens on degradation of color filter wastewater, a pseudo-first-order model was applied to obtain the rate constants. It was found that both the COD and TOC degradation efficiencies of color filter wastewater with or without Fresnel lens followed the pseudo-first-order reaction kinetics as indicated by high correlation coefficient ($r^2 > 0.90$) (Table 3). It was obvious that a significant enhancement for the degradation rate of color filter wastewater was achieved by using Fresnel lens. As
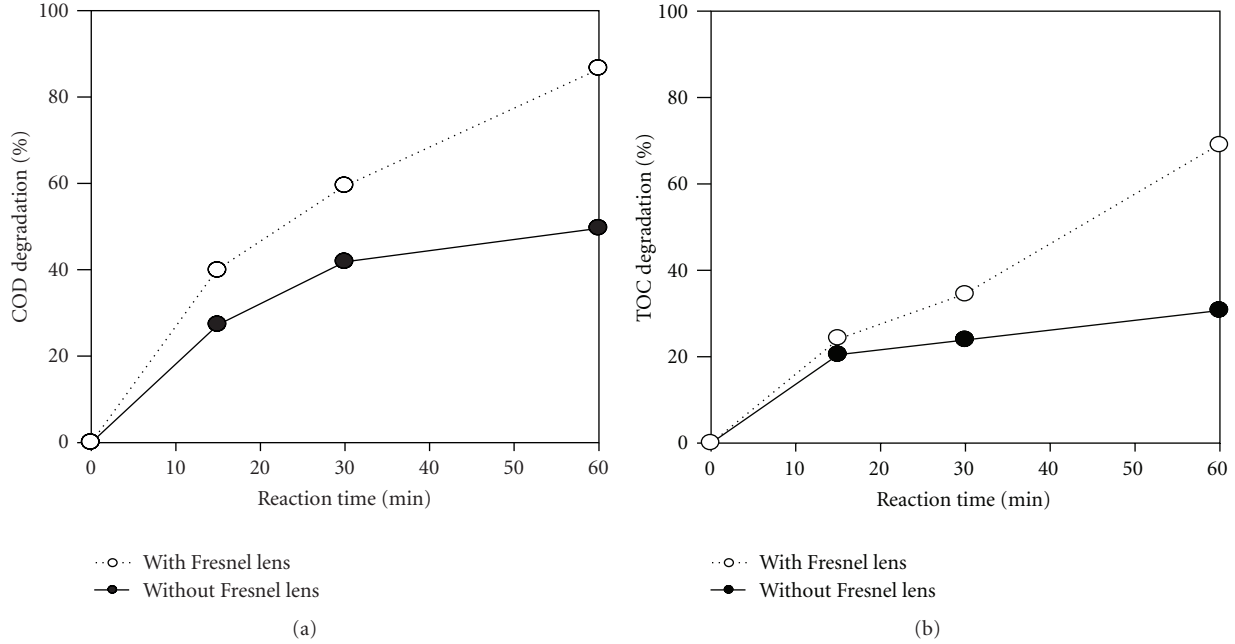
(a)

(b)

Figure 2: Effect of Fresnel lens on the degradation efficiency of (a) COD and (b) TOC of color filter wastewater in solar photo-Fenton process (initial pH: 5.0; H_2O_2/COD = 1.25 g/g; $[H_2O_2]_0/[Fe^{2+}]_0$ = 15).

Table 3: Effect of Fresnel lens on the degradation rate constant of color filter wastewater.

Solar Photo-Fenton Process	[a]k_{COD}, min^{-1}	[b]k_{TOC}, min^{-1}	[c]UV_{a+b}, W/m^2
Without Fresnel lens	0.0076 ± 0.00079	0.0032 ± 0.00050	54.82
With Fresnel lens	0.0342 ± 0.00232	0.0208 ± 0.00170	138.09

[*] Operation condition: pH_0: 5.0, 1.25 g H_2O_2/g COD, $[H_2O_2]_0/[Fe^{2+}]_0$ = 15.
[a]k_{COD}: pseudo-first-order rate constant based on the degradation of COD in solution for 95% confidence coefficient.
[b]k_{TOC}: pseudo-first-order rate constant based on the degradation of TOC in solution for 95% confidence coefficient.
[c]UV_{a+b}: UV light (280–400 nm) intensity.

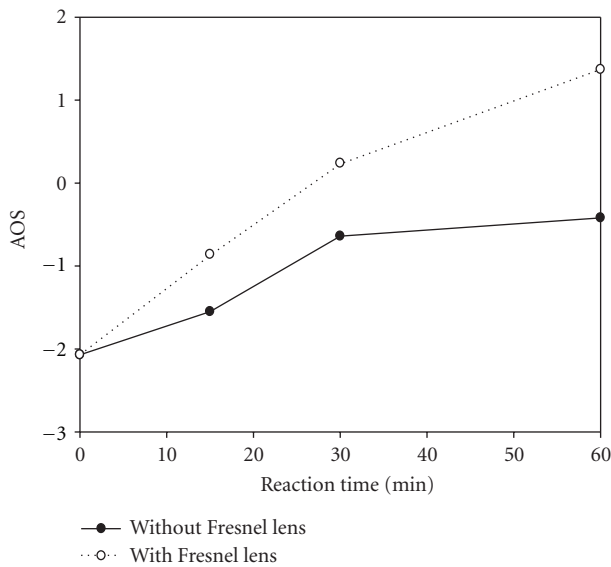Figure 3: Effect of Fresnel lens on AOS of color filter wastewater in solar photo-Fenton process (initial pH: 5.0; H_2O_2/COD = 1.25 g/g; $[H_2O_2]_0/[Fe^{2+}]_0$ = 15).

the rate constant shown in Table 3, the COD degradation rate and mineralization rate of color filter wastewater increased a factor of 4.5 and 6.5, respectively, mainly due to the UV_{a+b} light intensity increasing 2.5 times with assistance of Fresnel lens.

3.3. Effect of Fresnel Lens on the Biodegradability of Wastewater. The degree of oxidation and produced intermediates of color filter wastewater during solar photo-Fenton treatment could affect significantly the biodegradability of solution [13]. Average oxidation state (AOS) could be used to monitor the change in the degree of oxidation [14]. The average oxidation state of the organic carbon was calculated by

$$AOS = 4 - 1.5 \times \frac{COD}{TOC}, \qquad (2)$$

in which the unit of COD and TOC is mol O_2/L and mol C/L, respectively. The AOS value indicates how chemical substances in the effluent become more oxidized. A higher AOS value implies a higher degree of oxidation. Theoretically, the AOS has a value of +4 for CO_2, the most oxidized state of C, and −4 for CH_4, the most reduced state of carbon. As shown in Figure 3, the untreated color
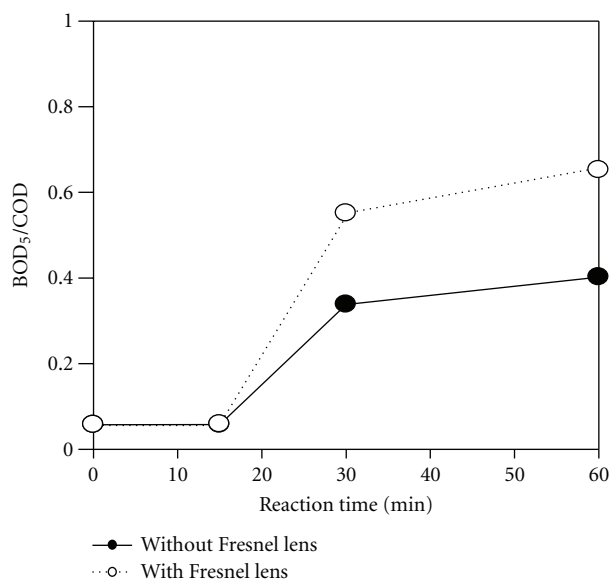
FIGURE 4: Effect of Fresnel lens on the biodegradability of color filter wastewater in solar photo-Fenton process (initial pH: 5.0; $H_2O_2/COD = 1.25$ g/g; $[H_2O_2]_0/[Fe^{2+}]_0 = 15$).

filter wastewater has an AOS value of -2.07 and the AOS values increased to 1.37 and -0.42 at a reaction time of 60 min with and without using Fresnel lens, respectively. This result implied that a higher degree of oxidation happened in Fresnel-lens-assisted system. Figure 4 showed the effect of Fresnel lens on BOD_5/COD of color filter wastewater. It was found that the Fresnel-lens-assisted solar photo-Fenton process could improve furthermore in the biodegradability of color filter wastewater. The required reaction time to reach the criteria of a ready biodegradability of wastewater, in which a BOD_5/COD value of 0.3 was usually selected, was less as a result for the Fresnel-lens-assisted system.

3.4. Effect of Fresnel Lens on the Microtoxicity of Wastewater. The effect of Fresnel lens on the microtoxicity of color filter wastewater in solar photo-Fenton process was shown in Figure 5. It was found that the microtoxicity of color filter wastewater increased obviously at a reaction time of 15 min, which may be due to more toxic intermediates generated at initial reaction stage. A similar result was also found in the study of González et al. [8]. However, the TU_{50} value decreased almost to 0 in the Fresnel-lens-assisted system as reaction was proceeding to 60 min, while the solar photo-Fenton process without Fresnel lens remained a TU_{50} value of 1.116.

4. Conclusion

With the assistance of Fresnel lens, the efficacy of solar photo-Fenton process enhanced considerably in terms of the COD degradation rate, mineralization rate, and biodegradability of color filter wastewater. In addition, the TU_{50} value of wastewater was almost diminished after a 60 min of treatment, whereas the microtoxicity of treated wastewater
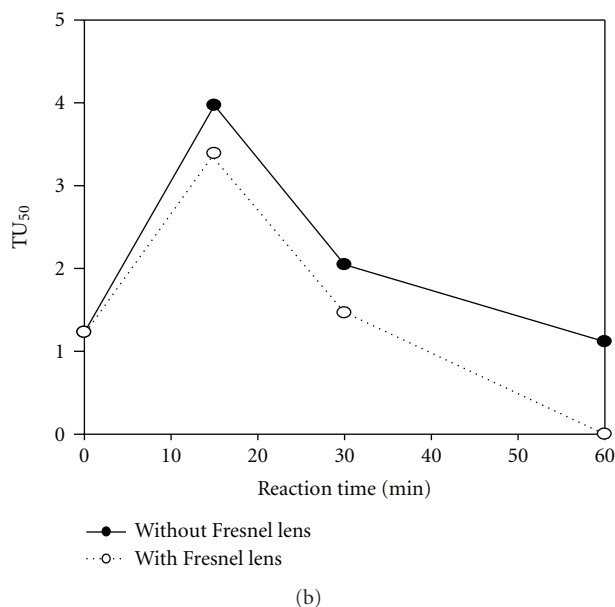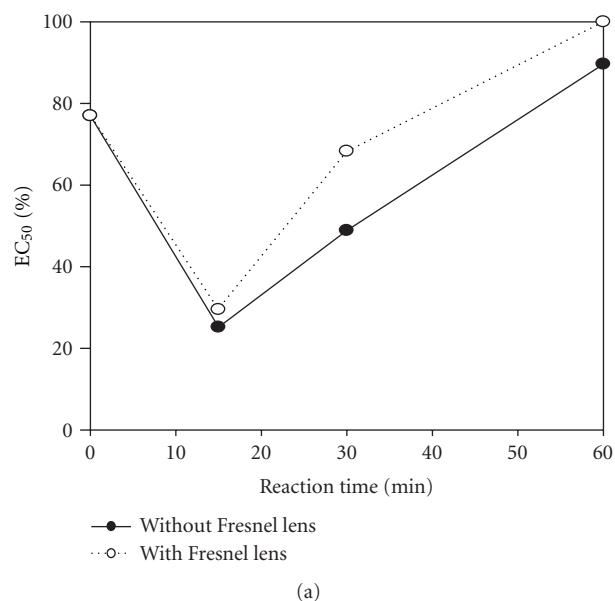

(a)

(b)

FIGURE 5: Effect of Fresnel lens on the microtoxicity of color filter wastewater in solar photo-Fenton process (initial pH: 5.0; $H_2O_2/COD = 1.25$ g/g; $[H_2O_2]_0/[Fe^{2+}]_0 = 15$).

without the assistance of Fresnel lens remained a TU_{50} value of 1.166. This could be mainly due to the concentrated effect of Fresnel lens for solar energy, resulting in an increase of 2~3 times of solar light intensity and a raising heat irradiation in terms of 15~30°C of wastewater temperature. Accordingly, solar energy could be concentrated effectively by using Fresnel lens and showed a significant promoting effect on the performance of solar photo-Fenton process for treating color filter wastewater.

Acknowledgment

References

[1] F. Al Momani, O. Gonzalez, C. Sans, and S. Esplugas, "Combining photo-Fenton process with biological sequencing batch reactor for 2,4-dichlorophenol degradation," *Water Science and Technology*, vol. 49, no. 4, pp. 293–298, 2004.

[2] L. A. Perez-Estrada, S. Malato, A. Aguera, and A. R. Fernandez-Alba, "Degradation of dipyrone and its main intermediates by solar AOPs: identification of intermediate products and toxicity assessment," *Catalysis Today*, vol. 129, pp. 207–214, 2007.

[3] M. I. Maldonado, P. C. Passarinho, I. Oller et al., "Photocatalytic degradation of EU priority substances: a comparison between TiO_2 and Fenton plus photo-Fenton in a solar pilot plant," *Journal of Photochemistry and Photobiology A*, vol. 185, pp. 354–363, 2007.

[4] S. Malato, P. Fernandez-Ibanez, M. I. Maldonado, J. Blanco, and W. Gernjak, "Decontamination and distinfection of water by solar photocatalysis: recent overview and trends," *Catalysis Today*, vol. 147, pp. 1–59, 2009.

[5] J. M. Monteagudo and A. Durán, "Fresnel lens to concentrate solar energy for the photocatalytic decoloration and mineralization of orange II in aqueous solution," *Chemosphere*, vol. 65, no. 7, pp. 1242–1248, 2006.

[6] R. M. Sellers, "Spectrophotometric determination of hydrogen peroxide using potassium titanium(IV) oxalate," *The Analyst*, vol. 105, no. 1255, pp. 950–954, 1980.

[7] APHA/AWWA/WEF, *Standard Methods for the Examination of Water and Wastewater*, Washington, DC, USA, 20th edition, 2000.

[8] O. González, C. Sans, and S. Esplugas, "Sulfamethoxazole abatement by photo-Fenton. Toxicity, inhibition and biodegradability assessment of intermediates," *Journal of Hazardous Materials*, vol. 146, no. 3, pp. 459–464, 2007.

[9] A. S. Koparal, Y. Yavuz, C. Gürel, and Ü. B. Öğütveren, "Electrochemical degradation and toxicity reduction of C.I. Basic Red 29 solution and textile wastewater by using diamond anode," *Journal of Hazardous Materials*, vol. 145, no. 1-2, pp. 100–108, 2007.

[10] J. H. Sun, S. P. Sun, G. L. Wang, and L. P. Qiao, "Degradation of azo dye Amido black 10B in aqueous solution by Fenton oxidation process," *Dyes and Pigments*, vol. 74, no. 3, pp. 647–652, 2007.

[11] I. B. S. Will, J. E. F. Moraes, A. C. S. C. Teixeira, R. Guardani, and C. A. O. Nascimento, "Photo-Fenton degradation of wastewater containing organic compounds in solar reactors," *Separation and Purification Technology*, vol. 34, no. 1–3, pp. 51–57, 2004.

[12] M. Rodriguez, V. Sarria, S. Esplugas, and C. Pulgarin, "Photofenton treatment of a biorecalcitrant wastewater generated in textile activities: biodegradability of the photo-treated solution," *Journal of Photochemistry and Photobiology A*, vol. 151, no. 1–3, pp. 129–135, 2002.

[13] W. S. Kuo and Y. Y. Ho, "Treatment of pesticide rinsate towards reuse by photosensitized Fenton-like process," *Water Science and Technology*, vol. 62, no. 6, pp. 1424–1431, 2010.

[14] F. Al Momani, "Impact of photo-oxidation technology on the aqueous solutions of nitrobenzene: degradation efficiency and biodegradability enhancement," *Journal of Photochemistry and Photobiology A*, vol. 179, no. 1-2, pp. 184–192, 2006.